On performance limitations of large-scale networks with distributed feedback control

EMMA TEGLING

Licentiate Thesis
Stockholm, Sweden 2016

Abstract

Networked control systems arise in a wide range of applications. These systems typically have a *global* control objective, as to drive the states at all network sites to a common setpoint, while the control is distributed and relies only on *local* feedback from a neighborhood around each site. In this thesis, we address the question of performance of large-scale networks with such distributed feedback control.

We consider networked dynamical systems with single and double integrator dynamics, subject to distributed disturbances. We focus on two types of problems. First, we consider problems modeled over regular lattice structures. Here, we consider consensus and vehicular formation control problems and evaluate performance in terms of measures of "global order", which capture the notion of network *coherence*. Second, we consider electric power networks, which we treat as dynamical systems modeled over general graphs. Here, we propose a measure of performance in terms of the resistive power losses that are incurred in maintaining network synchrony. These losses are associated with transient power flows that are a consequence of "local disorder" caused by lack of synchrony. In both cases, we characterize *fundamental limitations* to performance as networks become large.

It has been shown in previous studies that such limitations hold for coherence in networks with regular lattice structures. These studies show that connections in 3 spatial dimensions are necessary to achieve full coherence, when the controller uses static feedback from relative measurements in a local neighborhood. We show that these limitations remain valid also with *dynamic feedback*, where the controller at each network site has an internal memory state. However, if the controller can access certain absolute state information, dynamic feedback can improve performance compared to static feedback, allowing also 1-dimensional formations to be fully coherent.

For electric power networks, we show that the transient power losses grow unboundedly with network size. However, in contrast to previous results, performance does not improve with increased network connectivity. We also show that a certain type of distributed dynamic feedback controller can improve performance by reducing losses, but that the losses' scaling with network size seems to remain an important limitation. We discuss possible implications of these results in terms of design of future power grids, where an increasingly distributed generation paradigm leads to larger networks with the potential for greater performance issues.

Acknowledgements

I have had the privilege to work with some of the best.

First of all my main advisor Henrik Sandberg, whose insightful, supportive and friendly advice has been invaluable. Thank you for keeping your door open, for your attention both to detail and to the big picture and, of course, for convincing me to come back to KTH! I am so happy we are only half-way, and I already look forward to the work ahead of us!

I am most grateful to Bassam Bamieh, for welcoming me to UCSB, and for sharing so much of his knowledge, insight, and time with me. Working with you has been truly inspiring! My warmest thanks also to Dennice Gayme, whose encouragement and friendship over the last few years have meant so much. Thank you for introducing me to research and for sharing your passion with me!

I wish to thank my co-advisor Karl Henrik Johansson, whose visionary and intelligent ideas are always an inspiration. I am also lucky to have great collaborators in Martin Andreasson, Bart Besselink, John W. Simpson-Porco and Partha Mitra. Thank you for all the interesting and fruitful discussions so far!

All my colleagues and friends at the Automatic Control department, thank you for making my day, every day! I cannot mention all of you, but would like to extend a special thanks to Kaveh and Sebastian, for always being there for a fun conversation, and to Jana, for being both a great friend and role model! Thanks also to Silvia, Anneli, Hanna, Gerd, Karin and Margreth for the excellent administration at the department, and for all the friendly chats!

Finally, there are those who had nothing to do with the work that led up to this thesis, but who deserve my deepest gratitude all the same. You know who you are.

Contents

Chapter 1

Introduction

Networked systems are studied across all of science: from atomic networks through neurobiology and the animal kingdom to social networks and the internet. Some of the greatest engineering achievements of the 20th century, the electric power system and telecommunications, are also large and complex networks. Today, further networked systems arise in many engineering applications through the interconnection of smaller subsystems. For example, by connecting domestic solar panels into microgrids, through formations of unmanned aerial vehicles (UAVs), or in vehicle platoons. Some of these applications are illustrated in Figure 1.1.

In most of these applications, there is a desire to control the network to fulfill certain *global* control objectives. Such an objective may be synchrony or power balance in a power network, or a common cruising speed in a vehicle formation. It is often, however, neither possible nor practical to control the networks centrally. The control must therefore be distributed across the individual subsystems, and rely on feedback from a *local* neighborhood. Given that the control relies on such local feedback, an important question becomes whether there are limitations to the overall *performance* of the network. In particular, can performance be maintained as networks grow large?

In this thesis, we will address the question of performance in large-scale networks and explore limitations to performance in systems with distributed feedback control. Later in this chapter, we give a detailed problem formulation, but we first provide some context to the key problems considered in this thesis.
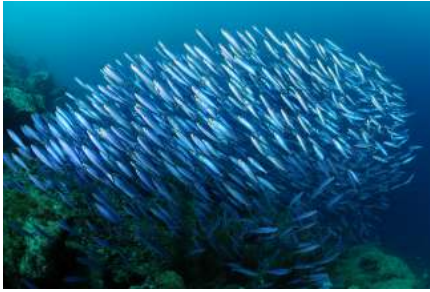
(a)
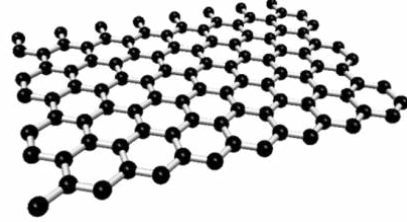
(b)

(c)

(d)

(e)
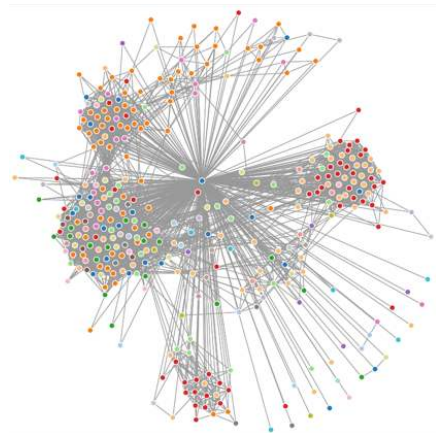
(f)

Figure 1.1: Examples of networked systems. (a) Fish school (b) Atomic network in graphene (c) Formation of UAVs (d) Vehicle platoon (e) Transmission network in the Nordic power grid (f) Visualization of personal network on LinkedIn (see List of Figures for image sources)

1.1 Control problems in large-scale networks

Due to their wide range of applications in engineering, networked control systems have received much attention from researchers over the last decades. In this section, we highlight key research problems related to the applications treated in this thesis.

Example 1.1 (Vehicle platoons and smart highway systems) The so-called platooning problem (control of strings of vehicles) has received much attention since some pioneering work in the sixties [46, 51]. The control objective in a vehicle platoon is typically to maintain a desired cruising velocity with a defined constant spacing between the vehicles. By keeping this spacing small, aerodynamic drag can be reduced, and thereby fuel costs and emissions, which motivates ongoing efforts for platooning in road freight transportation [1, 11]. By implementing platooning with long strings of vehicles, such as is the vision for automated highway systems [41, 78, 82], there is also a large potential to increase road capacity and throughput.
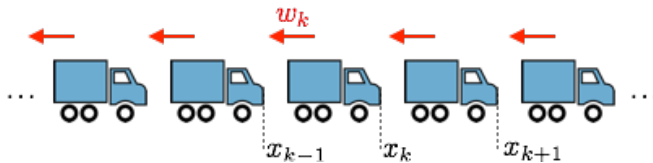
Figure 1.2: A vehicle platoon

The principle of a vehicle platoon is illustrated in Figure 1.2. An example of a simple linear control law for the kth vehicle of the platoon is the combined look-ahead and look-behind control (see e.g. [40]):

$$\ddot{x}_k = \dot{v}_k = f_+(x_{k+1} - x_k - \Delta_{(k+1,k)}) + f_-(x_{k-1} - x_k - \Delta_{(k-1,k)}) + \\ + g_+(v_{k+1} - v_k) + g_-(v_{k-1} - v_k) + w_k. \quad (1.1)$$

where f_+, f_-, g_+, g_- are constant gains, $\Delta_{j,k}$ denotes the desired spacing between vehicles j and k, and w_k is an external disturbance (due to, for example, wind gusts, varying road conditions, and measurement errors).

Apart from a multitude of practical challenges of which [82] gives an early overview, there are a number of control theoretical issues related to platooning that have been addressed over the last decades. Some examples are:

- How can it be ensured that disturbances are not amplified along the string of vehicles, in particular as the string grows large? This is an issue of so-called *string stability* [77].

- What control architecture is more robust: a leader-follower architechture, or a bidirectional architecture as in (1.1) [40]?

- What are optimal controller gains [47]?

- What types of measurements are needed to achieve reasonable performance? Do relative measurements with respect to neighbors (using for example radar) suffice, or is absolute position and velocity information (based on for example speedometers or GPS) for each vehicle required [39, 7]?

In this thesis, we address the question of whether feedback of the type (1.1) is sufficient to maintain *coherence* in a string of vehicles as it grows large. Coherence is a notion of "global order" and describes how well the formation resembles a rigid body. This important issue, which affects the throughput of a platoon, is a different concept from string stability mentioned above, as well as from the notion of robustness in [40].

Example 1.2 (Dynamic load balancing in distributed computing) Distributed computing means that a computational task is shared among a group of networked computers, in order to increase total processing capabilities and thereby efficiency. An important issue in distributed computing is *load balancing*, which means that each processor takes on a "fair share" of the total work load. If the computational problem is complex, it may be difficult to distribute sub-tasks a priori, and it is therefore desirable to balance the work load during the execution. Such a strategy is referred to as *dynamic* load balancing [16].

A very simple algorithm for dynamic load balancing can be written as follows (see, for example, [16, 60, 85]):

$$x_i(t+1) = x_i(t) + \sum_{j \in \mathcal{N}_i} a_{ij}(x_j(t) - x_i(t)) + w_i(t+1), \quad i = 1, \dots, N \qquad (1.2)$$

where the state $x_i(t)$ is the amount of work assigned to computer i at time instance t, $\mathcal{N}_i$ is the set of neighbors that computer i can share tasks with, and a_{ij} are nonnegative constants. The parameter $w_i(t+1)$ accounts for the new work that is generated at time t, less the amount of work that can be executed in one time step. If the computer is precisely able to keep up with the expected amount of new work, then w_i can be seen as a zero-mean random variable, and can be thought of as a distributed disturbance in the process (1.2).

The objective of this algorithm is to converge to an equilibrium where all work loads are equal, that is $x_i = x_j$ for all $i, j \in \{1, \dots, N\}$. Such a state of *consensus* can only hold approximately when the system is subject to distributed disturbances w. Still, it is desirable to keep deviations from a state of consensus small and the system's performance can therefore be quantified through

$$\mathbb{E}\left\{ \left(x_i(t) - \frac{1}{N} \sum_{j=1}^{N} x_j(t) \right)^2 \right\}, \qquad (1.3)$$

that is, the variance of the state x_i's deviation from the network average. This is done, for example, by Xiao *et al.* in [85], who study optimal design of the weights a_{ij} in (1.2) and by Patterson *et al.* in [60], who evaluate systems with stochastic communication failures. A further interesting problem is whether measures such as (1.3) can be kept small when distributed computation networks grow very large, as in a scenario where the internet is used to distribute computations. In other words, how well can approximate consensus be maintained in large-scale networks? In this thesis, we address such questions for continuous time equivalents of the system (1.2).

Example 1.3 (Frequency synchronization in power networks) The electric power system, which is one of the largest and most complex systems ever engineered, is currently undergoing rapid changes. The future power grid is expected to have higher levels of uncertainty from renewable energy sources [81], changing load patterns [65] and increasingly distributed electricity generation [91]. Many of these changes can affect the *synchronous stability* of the power network, which is the network's ability to recover synchrony after a disturbance [56]. This has therefore become an important research topic over the last years.
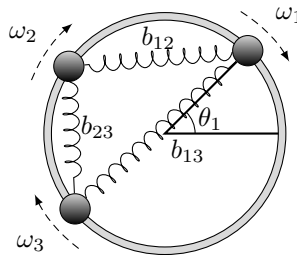
Figure 1.3: Mechanical analogy of the coupled swing equation (1.4), due to Dörfler *et al.* [22]. Any deviation in phase angle θ_i or frequency $\dot{\theta}_i = \omega_i$ is propagated over the springs (power lines) across the network.

Synchronization in power networks is typically studied through a system of coupled swing equations, which describe the electromechanical oscillations in synchronous generators, as in, for example, [22, 53]. The linearized swing equation can, under some simplifying assumptions, be written as:

$$m_i\ddot{\theta}_i + d_i\dot{\theta}_i = \sum_{j\in\mathcal{N}_i} b_{ij}(\theta_j - \theta_i) + P_{m,i}. \tag{1.4}$$

where θ_i is the phase angle at node i, $\dot{\theta}_i = \omega_i$ is the frequeny, and m_i and d_i are, respectively, the inertia and damping coefficients of the ith generator. $P_{m,i}$ can be regarded as the net power injection at the generator, and $\mathcal{N}_i$ is the neighbor set of

node i. This swing equation (1.4) can be illustrated by the mechanical analogy in Figure 1.3.

Even if the network is synchronously stable, lack of synchrony will arise when the system is subject to disturbances due to, for example, generation and load fluctuations that change $P_{m,i}$. For the network to function properly, without damage to the generators and other equipment, it is important that the frequency and phase angles are kept close to their nominal operating points. It is therefore desirable to keep the transient fluctuations "small". This is a question of the power system's *performance*, which is what we will address in this thesis.

Example 1.4 (Control of power electronics in microgrids) One of the main trends in today's electric power system is the transition from a centralized generation paradigm towards a more distributed one. Local, small-scale generation resources are expected to become prevalent in future power networks, as the penetration of renewable energy sources increases [91, 30]. The *microgrid* concept has gained popularity as a key strategy to facilitate this transition [50, 44]. Microgrids are networks composed of distributed generation (DG) units, loads and energy storage elements which can either connect to a larger power grid, or operate independently from it, in "islanded" mode.

The DG units within the microgrid are typically interfaced with the AC network via DC/AC or AC/AC power electronic converters, or *inverters*, and the operation of the network depends on control actions taken in these inverters [61, 89]. The main control objectives are:

(1) to maintain stability and power balance,

(2) to achieve active power sharing, that is, a desired steady-state distribution of the power injections from the individual inverter units, and,

(3) to maintain a steady frequency close to the nominal frequency ω^{ref}.

The standard control scheme employed to achieve these goals is *droop control*, which is a decentralized proportional controller that controls the voltage phase angle θ_i at the ith inverter according to

$$\dot{\theta}_i = \omega^{\mathrm{ref}} - k_i(\hat{P}_i - P_i^{\mathrm{ref}}), \tag{1.5}$$

where ω^{ref}, P_i^{ref} are the respective setpoints for frequency and active power injection. k_i is a constant gain and $\hat{P}_i$ is the measured power injection at the inverter. We show in Chapter 5 how this control law can be cast in the same form as the swing equation (1.4). The droop control law is, under reasonable conditions (see e.g. [72]), successful at fulfilling the control objectives (1) and (2). However, as it is effectively proportional control, it causes the steady-state network frequency ω^{ss} to deviate from its nominal value ω^{ref} [61], and does therefore not achieve (3).

This deficiency motivates so-called secondary control, the goal of which is to eliminate the static error. In order to achieve this goal, control architectures with various degrees of centralization have been proposed. Completely decentralized controllers will, unless carefully tuned, destroy the power sharing properties established by droop control, and may lead to a violation of generation constraints [5, 23]. Conversely, centralized control requires a dense communication architecture that conflicts with the microgrid paradigm of autonomous management and scalability. This has motivated the development of distributed control algorithms which simultaneously eliminate frequency errors and maintain the optimality properties of droop control [5, 72, 73, 88]. One such algorithm is the *distributed averaging proportional-integral (DAPI)* controller:

$$
\begin{aligned}
\dot{\theta}_i &= \omega^{\mathrm{ref}} - k_i(\hat{P}_i - P_i^{\mathrm{ref}}) + \Omega_i, \\
q_i \dot{\Omega}_i &= \omega^{\mathrm{ref}} - \omega_i - \sum_{j \in \mathcal{N}_i} c_{ij}(\Omega_i - \Omega_j),
\end{aligned}
\tag{1.6}
$$

where Ω_i is the secondary control variable and q_i and $c_{i,j}$ are nonnegative parameters. One of the main objectives of this thesis is to compare dynamic control laws, such as the DAPI controller (1.6), to static control laws such as (1.5), with respect to certain performance objectives.

1.2 Problem formulation

1.2.1 System model

In this thesis, we consider a number of distributed control problems with analogous mathematical settings. We will consider first-order systems, where there is one local state x_k at each site (or node) k of the network, as well as second-order systems, in which there are two such states: x_k and $\dot{x}_k$. The state x_k may, for example, represent the phase angle of the kth generator in an electric power network, while $\dot{x}_k$ represents its angular frequency.

Throughout, we will assume that the systems are subject to distributed disturbances w_k, which will in most cases be modeled as white noise[1] that is uncorrelated across the network. The systems can then be written as

$$
\dot{x}_k(t) = u_k(t) + w_k(t),
\tag{1.7}
$$

in the first-order case, and

$$
\ddot{x}_k(t) = u_k(t) + w_k(t),
\tag{1.8}
$$

---

[1] We refer to "white noise" in continuous time as a stationary zero-mean stochastic process with autocorrelation $\mathbb{E}\{w(\tau)w^*(t)\} = \delta(t - \tau)I$, where $\delta(t)$ denotes the Dirac delta distribution. This idealized process can be thought of as the time derivative of a Brownian motion, dB/dt, although such a derivative does not formally exist, see [76, Theorem 4.1].

in the second-order case. Here, $u_k(t)$ represents a control input.

The control objective in these systems is *global*; to drive the states at all nodes to a common equilibrium, such as a constant cruising speed in a vehicle platoon or synchrony in a power system. However, in all of the problems that we consider, the control is *distributed*, meaning that the control signal at any given node will only depend on *local* feedback from that node itself and from neighboring nodes, as illustrated in Figure 1.4. As we shall see, this fact leads to limitations in the system performance.

We consider linear feedback throughout and can therefore write the control input for the second-order system (1.8) as

$$u_k(t) = \sum_{j \in \mathcal{N}_k} f_{jk}(x_j(t) - x_k(t)) + \sum_{j \in \mathcal{N}_k} g_{jk}(\dot{x}_j(t) - \dot{x}_k(t)) - f_k^o x_k(t) - g_k^o \dot{x}_k(t), \quad (1.9)$$

where $\mathcal{N}_k$ denotes the neighbor set of the kth node and f_{jk}, g_{jk}, f_k^o, g_k^o are constant gains. (In the first-order case (1.7), the control input can be written as in (1.9), but without the terms containing $\dot{x}_k(t)$.)

Throughout the thesis, we will distinguish between and compare *relative* and *absolute* state feedback. In (1.9) the terms $-f_k^o x_k(t)$ and $-g_k^o \dot{x}_k(t)$ represent absolute feedback (or self-damping) from the states x_k and $\dot{x}_k$ respectively. If $f_k^o = g_k^o = 0$, the control relies only on relative differences between neighboring nodes. The availability of these types of feedback depends on the application. For example, the self-damping of the angular frequency in the swing equation (1.4) is part of the generator dynamics, while similar feedback from phase angles would require additional phasor measurement units (PMUs).

1.2.2   Performance measures

The systems (1.7) – (1.8) are subject to persistent stochastic disturbances w_k, which will cause the states at each network site to fluctuate around their equilibrium points, even when the system is stable. Since this thesis limits the analysis to linear systems, we can without loss of generality move these equilibrium points to the origin through a change of variables. Throughout this thesis, we will then characterize system performance by quantifying how "tightly" the states in the network stay together. Larger relative fluctuations between the network sites reflect a more disordered network, while small variances imply better performance. More precisely, we consider quantities such as:

Global error (coherence)

$$V_k^{\text{dav}}(t) := \mathbb{E}\left\{ \left(x_k(t) - \frac{1}{N} \sum_{j=1}^{N} x_j(t) \right)^2 \right\}, \qquad (1.10)$$

that is, the variance of the kth node's deviation from the global average over all N nodes in the network. For a vehicular platoon, for example, (1.10) characterizes how closely the platoon resembles a rigid body. In general, (1.10) is quantifies the amount of "disorder" in the network. In stationarity, this measure captures the notion of network *coherence.*

Local error (lack of synchrony)

$$V_k^{\text{loc}}(t) := \mathbb{E}\left\{ \left(\sum_{j \in \mathcal{N}_k} a_{j,k}(x_k(t) - x_j(t)) \right)^2 \right\}, \tag{1.11}$$

that is, the variance of the kth node's deviation from a local weighted average over its neighboring nodes. The measure (1.11) captures the amount of local disorder in the network, and quantifies the amount of interactions between neighboring nodes. The $a_{j,k}$ here are appropriately selected weights.

In power networks, where the state x_k represents phase angles, the quantity (1.11) signifies *lack of synchrony.* When the phase angles at neighboring nodes make excursions from their nominal values, non-equilibrium circulating currents will pass between them [84]. Such non-equilibrium current fluctuations act as a signaling mechanism that indicates the system needs to be re-synchronized, but they also result in resistive losses over the power lines. These losses are essentially the cost of using power flow fluctuations as the signaling mechanism to achieve synchronization and we therefore refer to them as the "price of synchrony". We will show in Chapter 4 that the price of synchrony can be written as a weighted sum of local errors over the entire network.

While the performance measures (1.10) and (1.11) may appear very similar, they capture two distinct phenomena in networked systems. For example, we will show in Chapter 4 that it is possible for two networks with very different global properties to have the same performance in terms of local errors. Conversely, a given network may appear well-regulated locally, although the network, when viewed as a whole, has unregulated modes. Such situations are explored in Chapter 3.

1.2.3 Objective

The objective of this thesis is to characterize performance of networked dynamical systems that can be written in the forms (1.7) and (1.8). We focus on two types of problem settings. First, we consider problems modeled over regular lattice structures. Here, we treat the consensus and vehicular formation problems as examples of the first- and second-order dynamics in (1.7) and (1.8), and evaluate performance in terms of measures of network coherence. Second, we consider electric power networks, which we treat as dynamical systems modeled over general graphs. Here, we
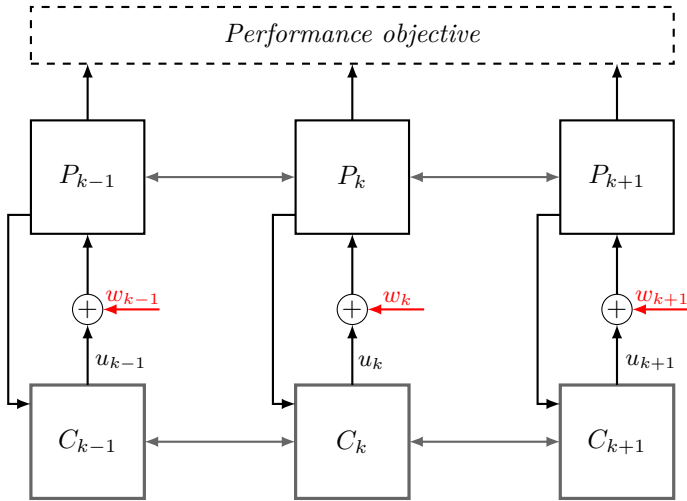
Figure 1.4: Illustration of the distributed networked control problem. P_k represents a plant controlled by the controller C_k. There is a common, global, performance objective.

focus on performance in terms of the resistive power losses incurred in maintaining network synchrony. For all of these systems, and their associated control laws u_k, we address questions such as

- How does performance scale with network size?

- How does performance depend on network topology and controller structure?

- How does performance depend on the order of the system dynamics?

The focus of the thesis is to identify and characterize *fundamental limitations* to performance, in particular as networks grow large. Such limitations imply that a control law cannot be designed to satisfy any given performance objective, as long as control effort is finite. They are therefore important in engineering applications, where resources are always limited. Fundamental performance limitations indicate a need to optimize the control under the given constraints, change the network design, or revert to alternative control strategies for which the limitations do not apply.

One of the main objectives of this thesis is therefore to address the question of whether *dynamic feedback*, where the controllers are equipped with memory, may alleviate performance limitations that hold for the standard, static feedback law in (1.9). We consider different structures of dynamic feedback laws with a single memory state and characterize under which conditions they may improve performance in large-scale networked systems.

1.3 Outline and contributions

The outline of the remainder of this thesis and its main contributions can be summarized as follows:

Chapter 2: Preliminaries

In this chapter, we provide some technical preliminaries on signal and system norms, graph theory and spatially invariant systems that are of relevance for this thesis.

Chapter 3: Coherence of large-scale networks with distributed dynamic feedback

As the first contribution of this thesis, we consider consensus and vehicular formation control problems modeled over a d-dimensional toric lattice. We evaluate performance of these systems in terms of notions of network coherence, quantified through the measure (1.10). In particular, we study the asymptotic scaling of this performance measure with respect to the lattice size. In [7], fundamental limitations to performance were derived for consensus and vehicular formation problems with local, static feedback on the form (1.9). The objective of Chapter 3 is to address the question of whether dynamic feedback laws can alleviate these limitations.

We evaluate the systems and their asymptotic performance scalings through a novel approach, where we exploit spatial invariance properties to study them in the limit of an infinite lattice. This allows us to formulate stability conditions for the dynamic feedback laws, revealing that several classes of controllers will inevitably de-stabilize large networks.

This chapter's main result shows that it is *not possible* to design a dynamic feedback law, based on *relative* state measurements, with better performance than static feedback. If the controller, however, can access some *absolute* state measurements, we show that dynamic feedback has the potential to improve asymptotic performance scalings compared to static feedback. We give examples of such feedback laws and discuss their limitations.

Chapter 3 is mainly based on

- E. Tegling, P. Mitra, H. Sandberg, B. Bamieh. Coherence and stability in large-scale networks with distributed dynamic feedback. *In prep.* To be presented at *22nd International Symposium on Mathematical Theory of Networks and Systems*, Minneapolis, USA, Jul 2016.

Chapter 4: The price of synchrony: resistive losses in synchronizing power networks

In the second main contribution of the thesis, we introduce the "price of synchrony" as a notion of performance in electric power networks. That is, the transient resistive power losses that are incurred in keeping a network of synchronous generators

in a synchronous state. We show how the total network's resistive losses can be quantified using an $\mathcal{H}_2$ norm of a linear system of coupled swing equations with an appropriately defined performance output. We evaluate this norm for general network topologies and provide a number of numerical examples as well as relevant bounds on performance.

This chapter's main results show that the price of synchrony scales unboundedly with network size, while being only weakly dependent on the network topology. These results point to a fundamental limitation to performance in networks where the frequency synchronization relies on power flows, and provide a basis for the analysis in Chapters 5 – 6.

The developments and results in Chapter 4 have been published in

- E. Tegling, B. Bamieh and D. F. Gayme. The price of synchrony: Evaluating the resistive losses in synchronizing power networks. *IEEE Transactions on Control of Network Systems*, Vol. 2, No. 3, pp.254-266, Sep 2015

Chapter 5: Renewable energy integrated power systems

In Chapter 5, we extend the model from Chapter 4 to account for certain aspects of renewable energy integrated power networks. We first extend the network model from Chapter 4 to explicitly include the frequency dynamics of loads and asynchronous generation, which results in a system of coupled first- and second-order dynamics. Second, we model a so-called microgrid, which is a low to medium voltage grid with the ability to operate independently from the main transmission network, in which renewable generation units are connected via controllable power inverters. Such networks typically require tighter voltage control than transmission systems. Therefore, we extend previous models to account for variable voltage dynamics, and quantify the additonal losses that arise through fluctuating voltages. The results in this chapter have been published in the following articles:

- E. Sjödin[2] and D.F. Gayme. Transient losses in synchronizing renewable energy integrated power networks. In *Proceedings of the American Control Conference*, pages 5217-5223, Jun 2014.

- E. Tegling, D. F. Gayme, and H. Sandberg. Performance metrics for droop-controlled microgrids with variable voltage dynamics. In *Proceedings of the 54th IEEE Conference on Decision and Control*, pages 7502-7509, Dec 2015.

Chapter 6: Improving performance of microgrids through distributed dynamic feedback

In the last main contribution of this thesis, we return to the question of whether performance can be improved through dynamic feedback. As in parts of Chapter 5, we consider inverter-based microgrids, where frequency synchronization is

---

[2]The name Sjödin was changed to Tegling in 2014.

achieved through controllable power electronics. We compare the standard, static control scheme to both a centralized and a distributed proportional-integral (PI) controller. We show that while performance is unchanged with centralized PI control, the distributed PI controller has the potential to significantly reduce transient power losses compared to the standard scheme. This performance improvement is also shown to depend on network topology and we discuss optimal tunings of the controller for loss reduction. The results in Chapter 6 have partly been published in:

- E. Tegling, M. Andreasson, J. W. Simpson-Porco, and H. Sandberg. Improving performance of droop-controlled microgrids through distributed PI-control. In *Proceedings of the American Control Conference*, Jul 2016. *To appear.*

Chapter 7: Conclusions

In this chapter, we conclude the findings of this thesis. In particular, we discuss the implications of the fundamental performance limitations found throughout this thesis for the applications introduced in the introduction. We also discuss limitations of the results as well as potential directions for future work.

Other publications

The contributions in the following two articles are not explicitly covered in this thesis.

- E. Sjödin, U. Topcu and D. F. Gayme. Risk-mitigated optimal power flow for wind powered grids. In *Proceedings of the American Control Conference*, pages 4431-4437, Jun 2012.

- N. Govindrajan, H. Arbabi, L. van Blargian, T. Matchen, E. Tegling and I. Mezic. An operator-theoretic viewpoint to non-smooth dynamical systems: Koopman analysis of a hybrid pendulum. *Submitted.*

Chapter 2

Preliminaries

In this chapter, we briefly review parts of the mathematical framework that will be used in this thesis. We first introduce the signal and system norms that are used for performance evaluations throughout. In Section 2.2, we then go through definitions and notation for the theory of spatially invariant systems, which is the basis for studying systems that are modeled over regular lattice structures. In Section 2.3 we introduce relevant concepts from graph theory, which will later be used to model electric power networks with general topologies.

2.1 Signal and system norms

Performance of control systems is often described in terms of the "size" of certain signals of interest. In this thesis, we will consider such signals that in some sense quantify the amount of network disorder, as described in Section 1.2.2. The size of these signals is then measured through relevant signal and system norms. In this section, we introduce the L_2 and $\mathcal{H}_2$ norms and discuss how they can be computed and interpreted. The theory is based on [90].

2.1.1 The L_2 norm

Consider a vector-valued signal $v(t) = [v_1(t), \ldots, v_n(t)]^T$ defined for $t \geq 0$. Its L_2 norm is defined as the square root of the integral of $v(t)^* v(t)$:

$$||v||_2 = \left(\int_0^\infty v(t)^* v(t) \mathrm{d}t \right)^{1/2}. \tag{2.1}$$

Here, and throughout the thesis, we use $*$ to denote the complex conjugate transpose of a vector or matrix. The L_2 norm can also be evaluated in the frequency domain. We then use the Laplace-transformed signal $\hat{v}(s)$, evaluated on the imagi-

nary axis $s = j\omega$:

$$||\hat{v}||_2 = \left(\frac{1}{2\pi} \int_{-\infty}^{\infty} \hat{v}(j\omega)^* v(j\omega) \mathrm{d}\omega \right)^{1/2}. \tag{2.2}$$

By Parseval's theorem, the time-domain and frequency-domain norms are equal, that is,

$$||v||_2 = ||\hat{v}||_2.$$

2.1.2   The $\mathcal{H}_2$ norm

Now, consider a general linear MIMO system in the Laplace domain: $\hat{y}(s) = G(s)\hat{w}(s)$, with input w, output y and transfer matrix $G(s)$. If the system is input-output stable, meaning that all controllable and observable system modes are asymptotically stable, the $\mathcal{H}_2$ norm is defined in analogy with the L_2 norm in (2.2) as

$$||G||_2 = \left(\frac{1}{2\pi} \int_{-\infty}^{\infty} \mathrm{tr}(G(j\omega)^* G(j\omega)) \mathrm{d}\omega \right)^{1/2}. \tag{2.3}$$

The $\mathcal{H}_2$ norm characterizes the system's input-output behavior by, in a sense, quantifying the size of the output y, as an average over all frequencies, given certain inputs w. In control design, it is often a control objective to keep the $\mathcal{H}_2$ norm below a given limit, and the feedback is chosen accordingly.

The integral in (2.3) is, however, rarely evaluated in the frequency domain using $G(j\omega)$. It can instead be evaluated conveniently in the time domain, directly from the corresponding state space representation:

$$\begin{aligned} \dot{\psi}(t) &= \mathcal{A}\psi(t) + \mathcal{B}w(t) \\ y(t) &= \mathcal{C}\psi(t), \end{aligned} \tag{2.4}$$

where $G(s) = \mathcal{C}(sI - \mathcal{A})^{-1}\mathcal{B}$. Again using Parseval's theorem, it is straightforward to show that $||G||_2$ is equal to the time-domain norm of the function $H(t) = \mathcal{C}e^{\mathcal{A}t}\mathcal{B}$ for $t \geq 0$ ($H(t) = 0$ for $t < 0$). We get that

$$||H||_2^2 = \mathrm{tr}\left(\int_0^{\infty} \mathcal{B}^* e^{\mathcal{A}^* t} \mathcal{C}^* \mathcal{C} e^{\mathcal{A}t} \mathcal{B} \mathrm{d}t \right). \tag{2.5}$$

Now, we define the *observability Gramian* as the matrix

$$X = \int_0^{\infty} e^{\mathcal{A}^* t} \mathcal{C}^* \mathcal{C} e^{\mathcal{A}t} \mathrm{d}t, \tag{2.6}$$

which allows (2.5) to be written as

$$||H||_2^2 = \mathrm{tr}\left(\mathcal{B}^* X \mathcal{B} \right). \tag{2.7}$$

The observability Gramian is given by the *Lyapunov equation*:

$$\mathcal{A}^* X + X\mathcal{A} = -\mathcal{C}^* \mathcal{C}. \tag{2.8}$$

We can also calculate $||H||_2^2$ using the *controllability Gramian* X_C; $||H||_{\mathcal{H}_2}^2 = \mathrm{tr}(\mathcal{C}X_C\mathcal{C}^*)$, with $\mathcal{A}X_C + X_C\mathcal{A}^* = -\mathcal{B}\mathcal{B}^*$.

Unitary invariance

The $\mathcal{H}_2$ norm from the input w to to the output y of the system (2.4) is unitarily invariant. This means that the norm does not change if the input and output are transformed through a unitary change of variables. Throughout this thesis, we will exploit this property when evaluating system $\mathcal{H}_2$ norms through spectral decompositions.

For this purpose, consider a unitary matrix U and assume that it (block) diagonalizes the system matrix $\mathcal{A}$, so that $U^*\mathcal{A}U = \hat{\mathcal{A}}$, with $\hat{\mathcal{A}} = \text{diag}\{\hat{\mathcal{A}}_n\}$, where $\hat{A}_n$, $n = 1, \ldots, N$ are either the eigenvalues of $\mathcal{A}$, or small block matrices, whose eigenvalues are, in turn, eigenvalues of $\mathcal{A}$. We use the matrix U to transform the state vector $\psi(t)$ according to:

$$\psi(t) =: U\hat{\psi}(t).$$

The system dynamics (2.4) in terms of the transformed states $\hat{\psi}$ become (recall that a unitary matrix U has the property that $U^*U = I$):

$$\dot{\hat{\psi}}(t) = U^*\mathcal{A}U\hat{\psi}(t) + U^*\mathcal{B}w(t)$$
$$y(t) = \mathcal{C}U\hat{\psi}(t),$$

Now, since the $\mathcal{H}_2$ norm is unitarily invariant, we can multiply the input and output by the unitary matrix U, without changing the $\mathcal{H}_2$ norm. We therefore define $\hat{w}(t) := U^*w(t)$ to $\hat{y}(t) := U^*y(t)$, and obtain the system $\hat{H}$ from $\hat{w}$ to $\hat{y}$ as

$$\dot{\hat{\psi}}(t) = U^*\mathcal{A}U\hat{\psi}(t) + U^*\mathcal{B}U\hat{w}(t) =: \hat{\mathcal{A}}\hat{\psi}(t) + \hat{\mathcal{B}}\hat{w}(t)$$
$$\hat{y}(t) = U^*\mathcal{C}U\hat{\psi}(t) =: \hat{\mathcal{C}}\hat{\psi}(t).$$

Now, assume that $\mathcal{B}$ and $\mathcal{C}$ are such that they are like $\mathcal{A}$ (block) digonalized by U. That is, $\hat{\mathcal{B}} = \text{diag}\{\hat{\mathcal{B}}_n\}$ and $\hat{\mathcal{C}} = \text{diag}\{\hat{\mathcal{C}}_n\}$. The norm (2.5), which can now be written as

$$||\hat{H}||_2^2 = \text{tr}\left(\int_0^\infty \hat{\mathcal{B}}^* e^{\hat{\mathcal{A}}^* t} \hat{\mathcal{C}}^* \hat{\mathcal{C}} e^{\hat{\mathcal{A}}t} \hat{\mathcal{B}} \mathrm{d}t \right),$$

is then, since all the matrices are diagonal, equivalent to

$$||\hat{H}||_2^2 = \text{tr}\left(\sum_{n=1}^N \int_0^\infty \hat{\mathcal{B}}_n^* e^{\hat{\mathcal{A}}_n^* t} \hat{\mathcal{C}}_n^* \hat{\mathcal{C}}_n e^{\hat{\mathcal{A}}_n t} \hat{\mathcal{B}}_n \mathrm{d}t \right). \tag{2.9}$$

Since the trace and the sum can switch places, we recognize that this is the sum of the respective squared $\mathcal{H}_2$ norms of N decoupled subsystems $\hat{H}_n$:

$$\dot{\hat{\psi}}_n(t) = \hat{\mathcal{A}}_n\hat{\psi}_n(t) + \hat{\mathcal{B}}_n\hat{w}_n(t)$$
$$\hat{y}_n(t) = \hat{\mathcal{C}}_n\hat{\psi}_n(t),$$

which allows us to simply evaluate the $\mathcal{H}_2$ norm of (2.4) as

$$||H||_2^2 = ||\hat{H}||_2^2 = \sum_{n=1}^{N} ||\hat{H}_n||_2^2.$$

In the first part of the thesis, we consider spatially invariant systems modeled over regular, periodic, lattice structures. In this case, the systems are constructed using circulant matrices, which can all be diagonalized using a spatial discrete Fourier transform, which we introduce in Section 2.2.3. This is a unitary transformation U, which allows us to use the spectral decomposition approach summarized in this section to evaluate system $\mathcal{H}_2$ norms. This approach will also be useful when analyzing systems modeled over general graphs in Chapters 4 – 6. In that case, we use the fact that the graph Laplacians used to model the network are unitarily diagonalizable (see Section 2.3.1).

2.1.3   Interpretations of the $\mathcal{H}_2$ norm

In this thesis, we will use input-output $\mathcal{H}_2$ norms to characterize system performance in various scenarios. This usage is supported by some of the $\mathcal{H}_2$ norm's standard interpretations, which we recap here. Denote by H the LTI system (2.4) and consider the following three scenarios:

  i. **Response to a white stochastic input.** When the input w is a white second order process with unit covariance (i.e. $\mathbb{E}\{w(\tau)w^*(t)\} = \delta(t-\tau)I$), the (squared) $\mathcal{H}_2$ norm of the system is the steady-state total variance of all of the output components, i.e.
$$||H||_2^2 \;=\; \lim_{t\to\infty} \mathbb{E}\{y^*(t)y(t)\}. \tag{2.10}$$

 ii. **Response to a random initial condition.** With zero input and an initial condition that is a random variable ψ_o with correlation $\mathbb{E}\{\psi_o\psi_o^*\} = \mathcal{B}\mathcal{B}^*$, the $\mathcal{H}_2$ norm is the time integral
$$||H||_2^2 \;=\; \int_0^\infty \mathbb{E}\{y^*(t)y(t)\} \; \mathrm{d}t \tag{2.11}$$

of the resulting response y. This interpretation is closely related to interpretation (iii):

iii. **Sum of impulse responses.** Let e_i refer to the vector with a 1 in the ith component and zero everywhere else. Consider N experiments where in each experiment, the system is fed an impulse at the ith input channel, that is, $w_i(t) \;=\; e_i\delta(t)$. Denote the corresponding output by y_i. The (squared) $\mathcal{H}_2$ norm is then the total sum of the L_2 norms of these outputs, i.e.
$$||H||_2^2 \;=\; \sum_{i=1}^{N} \int_0^\infty y_i^*(t)y_i(t) \; \mathrm{d}t. \tag{2.12}$$

A stochastic version of this scenario corresponds to a system where the inputs w_i can occur with equal probability. Under this assumption $\|H\|_2^2$ becomes the expected value of this integral.

2.2 Spatially invariant systems

In Chapter 3, we will consider networked control systems over regular lattice structures. We will assume these systems to be *spatially invariant* with respect to the network, which essentially means that the control dynamics are identical at each site in the network. The spatial invariance property simplifies the analysis of these systems by allowing us to block-diagonalize the system using spatial Fourier transforms. The details of this technical framework are presented in Section 3.3, but we provide some preliminaries here.

2.2.1 Topology

We will consider the problems over the undirected d-dimensional torus $\mathbb{Z}_N^d$, with $M = N^d$ nodes. In the one-dimensional case ($d = 1$), $\mathbb{Z}_N$ is simply the N node ring graph, which we can represent by the set of integers $\{-\frac{N}{2}, \ldots, -1, 0, 1, \ldots, \frac{N}{2} - 1\}$ mod N for N even, and $\{-\frac{N-1}{2}, \ldots, -1, 0, 1, \ldots, \frac{N-1}{2}\}$ mod N for N odd. $\mathbb{Z}_N^d$ is the direct product of d such rings. It will also be useful to define the infinite d-dimensional torus $\mathbb{Z}^d$, which is the direct product of d copies of the integers.

2.2.2 Functions and operators

We define real-valued function arrays over the network $\mathbb{Z}_N^d$, such as $a : \mathbb{Z}_N^d \mapsto \mathbb{R}$, where we will use multi-index notation to denote the kth array entry $a_k = a_{(k_1, \ldots, k_d)}$. Similarly, we denote the state at node $k = (k_1, \ldots, k_d)$ in the d-dimensional torus as

$$x_{(k_1, \ldots, k_d)}(t),$$

which is a scalar in $\mathbb{C}$ in the consensus problems and a vector-valued signal in $\mathbb{R}^d$ in the vehicular formation problems. We will in most cases omit the time dependence in the notation.

Linear operators, denoted by upper case letters, will be used to define multi-dimensional circular convolutions with function arrays over $\mathbb{Z}_N^d$. For example, the convolution operator A associated with the array a is defined as follows:

$$
\begin{aligned}
h = Ax = a \star x \\
\Updownarrow \\
h_{(k_1, \ldots, k_d)} = \sum_{(l_1, \ldots, l_d) \in \mathbb{Z}_N^d} a_{(k_1, \ldots, k_d) - (l_1, \ldots, l_d)} x_{(l_1, \ldots, l_d)},
\end{aligned}
\tag{2.13a}
$$

or, in short,

$$h_k = (Ax)_k = \sum_{l \in \mathbb{Z}_N^d} a_{k-l} x_l. \tag{2.13b}$$

In cases where the state $x \in \mathbb{R}^d$, the array element a_k is a $d \times d$ matrix, which in this thesis will be assumed to be diagonal due to coordinate decoupling. The arithmetic for $k+l = (k_1, \dots, k_d) + (l_1, \dots, l_d)$ is done in $\mathbb{Z}_N^d$ as follows: $(k_1, \dots, k_d) + (l_1, \dots, l_d) = (k_1+l_1, \dots, k_d+l_d) \bmod N$. Here, mod N implies that the operation is circulant. Note that all when considering systems over $\mathbb{Z}_N^d$, we assume all operators to be *spatially invariant* with respect to $\mathbb{Z}_N^d$. They can therefore be represented by convolution operators with single-index arrays as in (2.13).

2.2.3   Spatial Fourier transforms

The spatial Discrete Fourier Transform (DFT) of the array a will be denoted with $\hat{a}$, and we will use the letter n to denote the index, or *wavenumber*, of the spatial Fourier transform. For example, the function array $a_{(k_1, k_2, \dots, k_d)}$ has $\hat{a}_{(n_1, n_2, \dots, n_d)}$ as its Fourier transform, where the wavenumber $(n_1, n_2, \dots, n_d)$ can be thought of as a spatial frequency variable. When analyzing systems over $\mathbb{Z}_N^d$, we will use the DFT, which for functions $a_k : \mathbb{Z}_N^d \mapsto \mathbb{C}$ is defined as:

$$\hat{a}_n := \sum_{k \in \mathbb{Z}_N^d} a_k e^{-j \frac{2\pi}{N} n \cdot k}, \tag{2.14}$$

where $j = \sqrt{(-1)}$ denotes the imaginary number and $n \cdot k = n_1 k_1 + \cdots + n_d k_d$. The inverse Fourier transform is defined as $a_k = \frac{1}{M} \sum_{k \in \mathbb{Z}_N^d} \hat{a}_k e^{j \frac{2\pi}{N} n \cdot k}$.

Function arrays can also be defined over the infinite d-dimensional torus $\mathbb{Z}^d$. We then use the subscript ∞ for the array, as in a_∞, with entries $a_{(k_1, \dots, k_d)}$ for $k \in \mathbb{Z}^d$. The corresponding convolution operator is denoted A_∞. The Z-transform of a_∞ evaluated on the d-dimensional unit torus $\mathbb{T}^d = [-\pi, \pi]^d$ is defined as:

$$\hat{a}_\infty(\theta) := \sum_{k \in \mathbb{Z}^d} a_k e^{-j\theta \cdot k}, \tag{2.15}$$

where $\theta = (\theta_1, \dots, \theta_d)$. Note that unlike DFT, which is discrete in the wavenumbers n, the Z-transform is continous in θ. Under certain conditions, which we will exploit in Chapter 3, the DFT at wavenumbers n can be seen as subsamples of the Z-transform at the points $\theta = \frac{2\pi}{N}$.

We will use the term *(generalized) Fourier symbol* of convolution operators for the Fourier transform or Z-transform of the corresponding function array. For example, $\hat{a}$ in (2.14) is the Fourier symbol of the operator A. The values that $\hat{a}$ takes are exactly the eigenvalues of A [8]. In cases where a is matrix valued, the eigenvalues of A are the union of all eigenvalues of $\hat{a}_{(n_1, \dots, n_d)}$ as $(n_1, \dots, n_d)$ runs through $\mathbb{Z}_N^d$ (correspondingly, for A_∞, of $\hat{a}_\infty(\theta_1, \dots, \theta_d)$ for $(\theta_1, \dots, \theta_d) \in \mathbb{T}^d$).

2.3 Systems over general graphs

2.3.1 Graph theory

Let $\mathcal{G} = \{\mathcal{V}, \mathcal{E}\}$ be a graph, where $\mathcal{V} = \{1, \ldots, N\}$ is the set of nodes, or vertices, and $\mathcal{E} = \{e_{ij}\} \subset (\mathcal{V} \times \mathcal{V})$ represents the set of edges, or network lines. Let $\mathcal{N}_i$ denote the neighbor set of node i, that is, all nodes j such that $e_{ij} \in \mathcal{E}$.

Throughout this thesis, we will consider *weighted* graphs. That means that each edge is associated with a constant, nonnegative, weight a_{ij}. We can then define the weighted graph Laplacian L by

$$L_{ij} := \begin{cases} \displaystyle\sum_{k \in \mathcal{N}_i} a_{ik}, & \text{if } i = j, \\ -a_{ij} & \text{if } i \neq j \text{ and } j \in \mathcal{N}_i, \\ 0 & \text{otherwise,} \end{cases} \tag{2.16}$$

The elements on the diagonal L_{ii}, are called the *degree* of node i and is equal to the sum of the weights of all edges incident to that node. We denote the node degree by δ_i. In the special case where all edge weights $a_{ij} = 1$, δ_i is the number edges incident to node i, which is then equal to $|\mathcal{N}_i|$.

Weighted graph Laplacians can be used to compactly describe the consensus type dynamics in networked control problems as in the following simple example.

Example 2.1 (Average consensus) Consider a network of N agents, depicted in Figure 2.1, each with a scalar information state x_i, that is controlled according to: $\dot{x}_i = u_i$. The control objective is for all agents to reach consensus over this state, so that $x_1(t) = x_2(t) = \cdots = x^{\mathrm{avg}}$, where x^{avg} is the average of the initial states. This can be achieved through the standard average consensus algorithm:

$$u_i(t) = \sum_{j \in \mathcal{N}_i} a_{ij}(x_j - x_i).$$

Now, if we define the state vector $x = (x_1, \ldots, x_N)^T$, we can use the graph Laplacian (2.16) to write the control dynamics as:

$$\dot{x} = -Lx. \tag{2.17}$$

If the graph is connected, that is, if there is a path between any two agents in the network, then it is well known that the control objective, i.e., consensus, will be achieved (see for example [64]). That is, as $t \to \infty$, we have $x_1(t) = x_2(t) = \cdots = x^{\mathrm{avg}}$ (in the absence of disturbances).
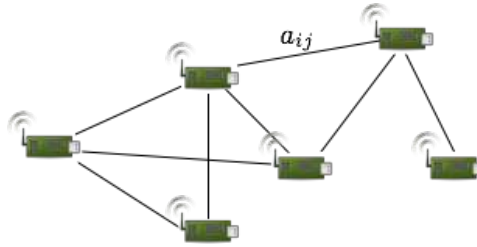
Figure 2.1: A network of N sensors, where the lines symbolize communication links with positive weights a_{ij}.

Properties of graph Laplacians

We now consider a $N \times N$ weighted graph Laplacian L defined as in (2.16) and list some of its properties:

i. **Symmetry.** For undirected graphs, the edge from node i to node j is identical to the edge from node j to node i. Therefore, $L_{ij} = L_{ji} \quad \forall i, j \in \{1, \ldots, N\}$, and L is symmetric.

ii. **Zero row/column sums.** Since $L_{ii} = -\sum_{j \neq i} L_{ij}$, all rows and columns sum to 0. That means that all graph Laplacians have as common eigenvector the vector $\mathbf{1}$ with all components equal to 1 that corresponds to the eigenvalue 0. That is,

$$L\mathbf{1} = 0.$$

Graph Laplacians are thus singular.

iii. **Positive semidefiniteness.** If the graph underlying the Laplacian is connected (that is, any two nodes are connected by a path of edges), then, apart from the simple zero eigenvalue, remaining $N - 1$ eigenvalues are positive. If the graph is not connected, the multiplicity of the zero eigenvalue will equal the number of isolated subgraphs.

iv. **Diagonalizability by unitary matrix.** Since L is symmetric, it can be diagonalized by a unitary matrix U whose columns are orthonormal (i.e., $U^*U = I$), such that $L = U^*\Lambda U$, where $\Lambda = \mathrm{diag}\{\lambda_1, \ \lambda_2, \ldots, \lambda_N\}$ is a diagonal matrix of L's eigenvalues $0 = \lambda_1 \leq \lambda_2 \leq \ldots \leq \lambda_N$.

2.3.2   Representation of power networks

A power network can be modeled as a graph $\mathcal{G} = (\mathcal{V}, \mathcal{E})$, where the nodes $\mathcal{V}$ are generator or load buses, and the edges $\mathcal{E}$ represent power lines. Each power line has an impedance $z_{ij} = r_{ij} + \mathbf{j}x_{ij}$, where r_{ij} is the line's resistance and x_{ij} is its reactance. Here, $\mathbf{j} = \sqrt{(-1)}$ denotes the imaginary number in order to avoid

confusion with the index j. An example of such a network for $N = 7$ is found in Figure 4.1. The inverse of the impedance is called *admittance*:

$$y_{ij} = \frac{1}{z_{ij}} = g_{ij} - \mathbf{j}b_{ij},$$

where $g_{ij} = \frac{r_{ij}}{r_{ij}^2 + x_{ij}^2}$ and $b_{ij} = \frac{x_{ij}}{r_{ij}^2 + x_{ij}^2}$ are respectively the *conductance* and *susceptance* of the line. Furthermore, each node $i \in \mathcal{V}$ may have a shunt conductance $\bar{g}_i$ and a shunt susceptance $\bar{b}_i$ which represent the node's connection to ground.

The power network is generally modeled through the network admittance matrix Y defined as:

$$Y_{ij} := \begin{cases} \bar{g}_i + \bar{b}_i + \sum_{k \in \mathcal{N}_i} (g_{ik} - \mathbf{j}b_{ik}), & \text{if } i = j, \\ -(g_{ij} - \mathbf{j}b_{ij}), & \text{if } i \neq j \text{ and } j \in \mathcal{N}_i, \\ 0 & \text{otherwise.} \end{cases} \tag{2.18}$$

where $\mathcal{N}_i$ denotes the neighbor set of node i. The diagonal elements Y_{ii} of the admittance matrix is the *self-admittance* of node i and is equal to the sum of the admittances of all lines incident (including the shunt) to that node.

Y can be partitioned into a real and an imaginary part and we define

$$Y = (L_G + \text{diag}\{\bar{g}_i\}) - \mathbf{j}(L_B + \text{diag}\{\bar{b}_i\}) \tag{2.19}$$

where L_G is called the conductance and L_B the susceptance matrix. The matrices L_G and L_B are each weighted graph Laplacians, where the weights are, respectively, the conductance and susceptance of each edge in the graph.

Chapter 3

Coherence of large-scale networks with distributed dynamic feedback

In this chapter, we treat the consensus and vehicular formation problems modeled over a d-dimensional toric lattice. We assume that the systems are subject to distributed stochastic disturbances, and evaluate performance in terms of notions of *coherence*, quantified through the steady state variance of nodal state fluctuations with respect to a global mean, as in (1.10). In particular, we study the asymptotic scaling of this performance measure with respect to network size. We call a system that exhibits a better scaling *more coherent* than a system with bad scaling, as the former will form a more rigid formation as the network grows.

Recent work has focused on characterizing performance limits in these types of systems in various settings [7, 47, 9, 59, 70]. In [7], fundamental limitations to performance in terms of network coherence were examined for consensus and vehicular formation problems with *relative, static feedback* as in (1.9). In the most problematic case, a 1-dimensional vehicle platoon, these limitations imply that even though the network is stable and has only small errors between neighboring nodes, it cannot be made coherent on a large scale. Instead, the formation exhibits an "accordion-type" motion, which limits the throughput performance of the platoon. It was shown that access to *absolute* measurements of all states are necessary to achieve full coherence in such platoons.

The objective of this chapter is to address the question of whether *dynamic feedback*, where the controllers are equipped with memory, may alleviate the fundamental performance limitations of local feedback found in [7]. We consider general dynamic control laws with a single internal controller state at each network site.

Performance is evaluated through input-output $\mathcal{H}_2$ norms, which according to the theory in Section 2.1 can be calculated using traces of Gramians. These traces are, in turn, sums involving eigenvalues of system matrices, which due to spatial invariance can be calculated as the values of the Fourier symbols of the corresponding feedback operators. In order to evaluate the asymptotic performance of the systems,

bounds on the $\mathcal{H}_2$ norms are established in terms of the scaling of the respective sums with increasing network size. As a key contribution of the present work, we propose a novel approach to evaluating such sums and their asymptotic scalings based on general Fourier analysis, see e.g. [8]. We study the systems in the limit of infinite toric lattices, and can therefore bound the discrete sums in the traces of system Gramians through corresponding integrals. We show that the asymptotic scalings of performance, as well as stability conditions, can be determined through simple properties of these integrals.

This chapter's main results show that it is *not possible* to design a dynamic feedback law, based on *relative* state measurements, with better performance than static feedback. If the controller, however, can access some *absolute* state measurements, we show that dynamic feedback has the potential to improve asymptotic performance scalings compared to static feedback. We give examples of such feedback laws and discuss their limitations.

The remainder of this chapter is outlined as follows. We first introduce the static and dynamic control laws for the consensus and the vehicular formation problem in Section 3.1. We define the performance meausure and give a preview of our main result in Section 3.2 and provide the mathematical framework needed to derive this result in Section 3.3. In Section 3.4, we evaluate the dynamic feedback laws with respect to stability properties and performance, and discuss our main findings in Section 3.5. We summarize and conclude this chapter in Section 3.6.

3.1   The consensus and vehicular formation problems

We now formulate models for two types of problems: *consensus* and *vehicular formations*. Both problems are modeled on networks over the discrete torus $\mathbb{Z}_N^d$. In the consensus problem there is a local, scalar information state x_k at each network site, while there are two such states (position and velocity) in the vehicular formation case.

For both models, we introduce a *static controller*, as considered in [7], which we will compare to a *dynamic controller* with an additional memory state at each network site, see Figure 3.1.

We also assume additive stochastic disturbances at each network site. These persistent stochastic disturbances will cause the nodes to fluctuate around the equilibrium point, and it is the variance of those fluctuations that we will consider as the *performance* of the systems.

3.1.1   Consensus

We first consider the first order consensus algorithm in continuous time over the discrete torus $\mathbb{Z}_N^d$. The single integrator dynamics at each site k in the network is then given by

$$\dot{x}_k = u_k + w_k, \quad k \in \mathbb{Z}_N^d, \tag{3.1}$$
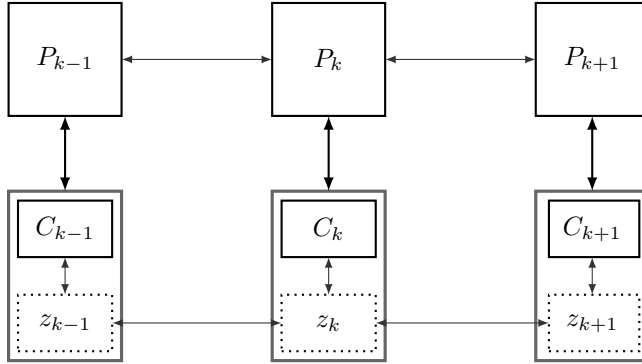
Figure 3.1: Controller structure for the dynamic feedback laws.

where u_k denotes the control signal. The process disturbance w_k, modeling random insertions and deletions, is mutually uncorrelated across nodes, and we will model it as a zero mean white noise.

We now introduce the two types of linear feedback control for the system (3.1).

Static feedback

In the case of static feedback, the control signal depends directly on the current state, such that

$$u_k = (Fx)_k. \tag{3.2}$$

The feedback operator F, can be suitably designed to fulfill the control objectives. A common example of such a control scheme is the one where the control signal at each node is the weighted average of the differences between that node and its $2d$ neighbors, i.e.,

$$u_k = \tilde{f}[(x_{(k_1-1,\ldots,k_d)} - x_k) + (x_{(k_1+1,\ldots,k_d)} - x_k) + \cdots \\ + (x_{(k_1,\ldots,k_d-1)} - x_k) + (x_{(k_1,\ldots,k_d+1)} - x_k)], \tag{3.3}$$

where $\tilde{f}$ is a positive scalar. The algorithm (3.3) will be referred to as the *standard consensus algorithm*. The associated function array is:

$$f_{(k_1,\ldots,k_d)} = \begin{cases} -2d\tilde{f} & k_1 = \cdots = k_d = 0 \\ \tilde{f} & k_i = \pm 1, \text{ and } k_j = 0, \text{ for } i \neq j \\ 0 & \text{otherwise.} \end{cases} \tag{3.4}$$

In the general case, we can write the consensus algorithm (3.1) with static feedback as

$$\dot{x} = Fx + w. \tag{3.5}$$
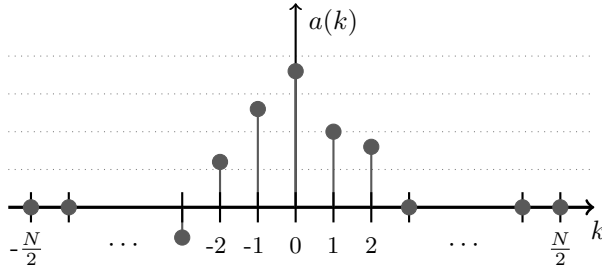
Figure 3.2: A local function array a defined over $\mathbb{Z}_N$.

Dynamic feedback

To model the dynamic feedback, we let the controller have access to an internal controller state $z_{(k_1,\ldots,k_d)}$, which is a scalar at each network site k:

$$u_k = z_k + (Fx)_k$$
$$\dot{z}_k = (Az)_k + (Bx)_k,$$

where A, B, F are linear feedback operators, the properties of which will be discussed shortly. We can now write the consensus algorithm (3.1) with dynamic feedback as:

$$\begin{bmatrix} \dot{z} \\ \dot{x} \end{bmatrix} = \begin{bmatrix} A & B \\ I & F \end{bmatrix} \begin{bmatrix} z \\ x \end{bmatrix} + \begin{bmatrix} 0 \\ I \end{bmatrix} w. \tag{3.6}$$

3.1.2   Structural assumptions for the consensus algorithm

We now list the assumptions imposed on the system and on the feedback operators A, B, F in the consensus algorithm. Assumptions 3.1-3.2 will also carry over to the vehicular formation problems.

Assumption 3.1 (Spatial invariance)   All feedback operators are spatially invariant and fixed with respect to $\mathbb{Z}_N^d$, and are therefore circular convolution operators, as defined in (2.13).

   For example, the standard consensus algorithm (3.3) can be written as the convolution of the state x with the array (3.4).

Assumption 3.2 (Locality)   All feedback operators use only local information from a neighborhood of width $2q$, where q is independent of N. For example, for the function array f, associated with the operator F, this means that

$$f_{(k_1,\ldots,k_d)} = 0 \quad \text{if} \quad |k_i| > q, \tag{3.7}$$

for any $i \in \{1, 2, \ldots, d\}$. The same condition holds for the operators A and B. The situation is illustrated in Figure 3.2.

Assumption 3.3 (Relative state measurements) We assume that all controllers can only access relative measurements of the physical state x. Hence, the feedback can only involve differences between states of neighboring nodes. For example, this means that each term of the form $\tilde{f} x_k$ in the convolution Fx is accompanied by another term $-\tilde{f} x_l$, for some other index l, so that we obtain $\tilde{f}(x_k - x_l)$.

In particular, this implies that the operators F and B in (3.5) and (3.6) have the property

$$\sum_{k \in \mathbb{Z}_N^d} f_k = 0, \quad \sum_{k \in \mathbb{Z}_N^d} b_k = 0. \tag{3.8}$$

Since the state z is internal to the controller and is therefore always measurable, we need not impose any similar requirements on A.

3.1.3   Vehicular formations

For the vehicular formation problem, consider $M = N^d$ identical vehicles arranged in the d-dimensional torus $\mathbb{Z}_N^d$. The double integrator dynamics at each site $k = (k_1, \ldots, k_d)$ in the torus is then

$$\ddot{x}_k = u_k + w_k, \tag{3.9}$$

where, as above, u_k is the control signal and w_k is white process noise, which models random forcings at each site.

The position vector $x_k = [x_k^1 \ \cdots \ x_k^d]^T$ at each network site, and its time derivative, the velocity vector $v_k = [v_k^1 \ \cdots \ v_k^d]^T$, are both d-dimensional vectors. Without loss of generality, we will assume that they each represent absolute deviations from a desired trajectory $\bar{x}_k$ and constant heading velocity $\bar{v}$, with

$$\bar{x}_k := \bar{v} t + k \Delta_x.$$

Here, Δ_x is the constant spacing between the vehicles in $\mathbb{Z}_N^d$.

We now introduce the two types of linear feedback control for the system (3.9).

Static feedback

The control input is here assumed to be full state feedback that is linear in the variables x and v:

$$u_k = (Fx)_k + (Gv)_k.$$

An example of such feedback would be the combined look-ahead and look-behind controller in a 1-D string:

$$\begin{aligned} u_k =& f_+(x_{k+1} - x_k) + f_-(x_{k-1} - x_k) + g_+(v_{k+1} - v_k) + \\ &+ g_-(v_{k-1} - v_k) + f_o x_k + g_o v_k, \end{aligned} \tag{3.10}$$

where the f's and g's are positive design parameters. If f_o and g_o are both zero, this control law satisfies Assumption 3.3 of relative state measurements. If $f_o \neq 0$

or $g_o \neq 0$, we will refer to those terms in the feedback law as *absolute feedback* from either position or velocity.

Suppressing the spatial index of all variables, the vehicular formation algorithm (3.9) with the static feedback becomes

$$\begin{bmatrix} \dot{x} \\ \dot{v} \end{bmatrix} = \begin{bmatrix} 0 & I \\ F & G \end{bmatrix} \begin{bmatrix} x \\ v \end{bmatrix} + \begin{bmatrix} 0 \\ I \end{bmatrix} w. \tag{3.11}$$

Dynamic feedback

To model the dynamic feedback law, we introduce the internal controller state $z_{(k_1,\dots,k_d)}$ at each network site k, which is a d-dimensional vector containing a memory of past position and velocity errors in each coordinate direction. We get:

$$u_k = z_k + (Fx)_k + (Gv)_k$$
$$\dot{z}_k = (Az)_k + (Bx)_k + (Cv)_k.$$

An example of dynamic feedback control for double integrator systems is the *distributed averaging proportional-integral* (DAPI) control from Example 1.4, which has received much recent attention in the context of coupled oscillator systems and control of microgrids [5, 72, 88, 79]. These systems are analogous to the present vehicular formation problem under certain assumptions, such as absolute velocity feedback. One DAPI control algorithm is:

$$u_k = z_k + f_+(x_{k+1} - x_k) + f_-(x_{k-1} - x_k) - g_o v_k$$
$$\dot{z}_k = a_+(z_{k+1} - z_k) + a_-(z_{k-1} - z_k) - c_o v_k \tag{3.12}$$

where the operator A achieves a weighted averaging of the internal state z across nodes, which prevents unfavorable drift in the memory states at different nodes (see e.g. [5]). Such drift would, in practice, de-stabilize the system if $A = 0$, in which case one has retrieved a decentralized *proportional-integral* (PI) controller with respect to the velocity.

In general, we can write the equations of motion for the closed loop system with dynamic feedback as:

$$\begin{bmatrix} \dot{z} \\ \dot{x} \\ \dot{v} \end{bmatrix} = \begin{bmatrix} A & B & C \\ 0 & 0 & I \\ I & F & G \end{bmatrix} \begin{bmatrix} z \\ x \\ v \end{bmatrix} + \begin{bmatrix} 0 \\ 0 \\ I \end{bmatrix} w. \tag{3.13}$$

3.1.4   Structural assumptions for the vehicular formation problems

For the vehicular formation systems, we impose a number of assumptions in addition to Assumptions 3.1 – 3.2 listed in Section 3.1.2:

Assumption 3.4 (Relative vs. absolute feedback)   While we assume only relative state measurements to be available in the consensus case, we will also consider the

consequences of *absolute state feedback* from x and v for the vehicular formation control. In particular, while relative feedback means that a given operator satisfies the condition (3.8), we use the term absolute feedback when it does not.

The presence of viscous damping can be treated as a special case of absolute state feedback. The model (3.9) can then be modified according to:

$$\ddot{x}_k = -\mu \dot{x}_k + u_k + w_k, \tag{3.14}$$

where $\mu \geq 0$ is the drag coefficient. Comparing this to (3.10) we can identify μ with g_0, the absolute velocity feedback term.

The results presented in [7] showed that absolute state feedback is necessary to avoid an unfavorable scaling of performance. In this thesis, we show that this conclusion remains valid with dynamic feedback and list the results with the various types of feedback in Theorem 3.1.

Assumption 3.5 (Reflection symmetry) The interactions between the vehicles on $\mathbb{Z}_N^d$ are symmetric around each site k. This implies that the arrays associated with the operators A, B, C, F, G have even symmetry, so that for each term like $\alpha f_{(k_1, \ldots, k_d)}$ there is a term $\alpha f_{(-k_1, \ldots, -k_d)}$. In the examples (3.10) and (3.12) this condition requires $a_+ = a_-$, $b_+ = b_-$, $f_+ = f_-$ and $g_+ = g_-$.

A particular implication of this assumption is that the Fourier symbols of the operators will be real valued.

This symmetry property, while not always enforced, will be relevant also in the consensus case. By slight abuse of terminology, we will in the following refer to a feedback operator as *symmetric* if the associated array has this property, and *asymmetric* if it does not.

Assumption 3.6 (Coordinate decoupling) We assume that the feedback control in each of the d coordinate directions is entirely decoupled from the vector components in the other coordinates. We furthermore assume that the array elements associated with the operators A, B, C, F, G are isotropic. By this assumption, the array elements are diagonal and the convolution in (2.13b) will turn into d decoupled, identical, scalar convolutions.

3.2 Performance measure and main result

We are concerned with the performance of the consensus and vehicular formation problems in terms of the amount of global "disorder" of the system at steady state. This can be quantified as the steady state variance of nodal state fluctuations, which are caused by persistent stochastic disturbances. In particular, we are interested in the scaling of this performance measure with the system size. We call a system which exhibits a better scaling *more coherent* than a system with bad scaling, as the former will form a more rigid formation when the system grows. If the scaling is such that the variance per node is bounded, the system is said to be fully *coherent*.

To define the relevant performance measure, we adopt the approach in [7], but restrict our attention to one of the three performance measures evaluated there. First, recall from Section 2.1 a general linear MIMO system driven by zero mean white noise w with unit intensity (that is, $\mathbb{E}\{w(\tau)w^*(t)\} = \delta(t-\tau)I$):

$$\dot{\psi} = \mathcal{A}\psi + \mathcal{B}w \tag{3.15a}$$

$$y = \mathcal{C}\psi. \tag{3.15b}$$

In our case, equation (3.15a) represents, for example, the feedback system in (3.13), for which a performance output as in (3.15b) will now be defined.

Provided that the system (3.15) is input-output stable, its squared $\mathcal{H}_2$ norm from w to y can be intepreted as the total steady state variance of the output:

$$V := \sum_{k \in \mathbb{Z}_N^d} \lim_{t \to \infty} \mathbb{E}\{y_k^*(t)y_k(t)\}. \tag{3.16}$$

Throughout this chapter, we are considering spatially invariant systems over the discrete torus $\mathbb{Z}_N^d$. This implies that the variance of the output at all sites k, $\mathbb{E}\{y_k^*(t)y_k(t)\}$ in the network will be equal. We obtain this *individual output variance* by simply dividing the total $\mathcal{H}_2$ norm by the system size $M = N^d$:

$$V_M = \mathbb{E}\{y_k^*(t)y_k(t)\} = \frac{V}{M}. \tag{3.17}$$

We next define the relevant output measurement:

Definition 3.1 (Deviation from average performance output) The deviation of each state from the average of all states is measured as:

$$y_k := x_k - \frac{1}{M} \sum_{l \in \mathbb{Z}_N^d} x_l \tag{3.18}$$

In operator form, this becomes

$$y = (I - \frac{1}{M} J_{\mathbf{1}})x =: H^{dav}x, \tag{3.19}$$

where $J_{\mathbf{1}}$ is the convolution operator corresponding to the array of all elements equal to 1.

We use this operator to define outputs for the consensus problems as $y = H^{dav}x$ in the case of static feedback and as

$$y = \begin{bmatrix} 0 & H^{dav} \end{bmatrix} \begin{bmatrix} z \\ x \end{bmatrix}$$

in the case of dynamic feedback. In the vehicular formation case, the output will involve positions only, so we set

$$y = \begin{bmatrix} H^{dav} & 0 \end{bmatrix} \begin{bmatrix} x \\ v \end{bmatrix} \quad \text{or} \quad y = \begin{bmatrix} 0 & H^{dav} & 0 \end{bmatrix} \begin{bmatrix} z \\ x \\ v \end{bmatrix},$$

for static and dynamic feedback respectively.

It is well known that systems with consensus type dynamics, such as the ones considered in this thesis, typically have a single marginally stable mode at the origin corresponding to the motion of the mean state (this is a consequence of Assumption 3.3 of relative measurements). In order for the steady state variance in (3.16) to be finite, any unstable system modes must be unobservable from the output. Here, the output operator H^{dav} is such that the corresponding array $\{h_k\}$ has the property $\sum_{k \in \mathbb{Z}_N^d} h_k = 0$ (condition (3.8)). Therefore, this mean mode is unobservable from the output, and the $\mathcal{H}_2$ norm in (3.16) will be finite, provided remaining system modes are stable.

3.2.1   Performance scalings with static and dynamic feedback

Our main objective is to determine whether dynamic feedback in the forms (3.6) and (3.13) may improve performance compared to the static feedback laws (3.5) and (3.11) that were also evaluated in [7]. Throughout the following sections, we introduce the methodology that we use to establish asymptotic scalings of the individual output variances in (3.17). At this point, we summarize our main results as follows:

Theorem 3.1   *The asymptotic scalings of individual output variances* (3.17) *for the consensus problem satisfying Assumptions 3.1 - 3.3 and the vehicular formation problem satisfying Assumptions 3.1 - 3.2, 3.4 - 3.6 are as follows:*

1. *Consensus*

    a) *Static feedback* or *dynamic feedback*

$$V_M \sim \frac{1}{\beta} \begin{cases} M & d = 1 \\ \log M & d = 2 \\ 1 & d \geq 3, \end{cases} \qquad (3.20)$$

2. *Vehicular formations*

    a) *Static feedback* or *dynamic feedback with* relative *position and* relative *velocity feedback*

$$V_M \sim \frac{1}{\beta^2} \begin{cases} M^3 & d = 1 \\ M & d = 2 \\ M^{1/3} & d = 3 \\ \log M & d = 4 \\ 1 & d \geq 5, \end{cases} \qquad (3.21)$$

    b) *Static feedback* or *dynamic feedback with* absolute *position and* relative *velocity feedback,*

Static feedback with relative *position and* absolute *velocity feedback*

$$V_M \sim \frac{1}{\beta} \begin{cases} M & d = 1 \\ \log M & d = 2 \\ 1 & d \geq 3, \end{cases} \tag{3.22}$$

c) *Dynamic feedback with* relative *position and* absolute *velocity feedback,*

Static feedback or *dynamic feedback with* absolute *position and* absolute *velocity feedback*

$$V_M \sim 1, \tag{3.23}$$

where $M = N^d$ is the total network size, β is an algorithm parameter reflecting control effort, and the notation $\sim$ implies scaling up to a multiplicative factor that is independent of M and β.

There are therefore no dynamic feedback laws on the forms (3.6) and (3.13) based on only relative state measurements, that exhibit better coherence properties than static, memoryless feedback. In the vehicular formation case, the same conclusion holds also in the case of absolute position and relative velocity feedback.

However, with absolute feedback from velocities it is, in theory, possible to achieve full coherence in any spatial dimension using a dynamic feedback protocol, even though position measurements are relative. This is in contrast to static feedback, where absolute measurements of all states are required to achieve the same result. We will discuss implications of these results in more detail in Section 3.4.4.

Remark 3.1 All controllers we consider are strictly proper. This implies that in the case 2b) of Theorem 3.1, absolute velocity feedback cannot be derived instantaneously from the absolute position measurements that are available. In order to obtain full coherence, the controller must therefore access absolute velocity measurements directly.

3.3   The limit from finite to infinite lattices

We now introduce the technical framework that will be used to determine the asymptotic scalings of the $\mathcal{H}_2$ norms in Theorem 3.1, for the consensus and vehicular formation systems.

This novel framework is based on the idea of mapping the system dynamics onto an infinite lattice. The $\mathcal{H}_2$ norms, which are calculated using traces of system Gramians that lead to sums involving system eigenvalues, can then, in the limit of large systems, instead be estimated through integrals over continuous functions. We show how the asymptotic scaling of the $\mathcal{H}_2$ norm can be determined through simple properties of that integral.

3.3.1 Spatial convolution operators on infinite lattices

All feedback operators considered in this chapter define convolutions with *local* arrays on $\mathbb{Z}_N^d$, by Assumption 3.2. Hence, for a given operator A we have that $a_k = 0$ if $|k| > q$ for some fixed q. This means that any operator array a can be unambiguously re-defined on $\mathbb{Z}_{N'}$ for *any* given $N' > 2q$ by filling it with zero components wherever $|k| > q$. This also means that any such local array can be used to define a convolution over the *infinite* $\mathbb{Z}^d$, see Figure 3.3. As we shall see, it will be useful to think of the sites in the finite lattice $\mathbb{Z}_N^d$ as sampling points of the infinite torus $\mathbb{Z}_N^d$.

Let a be a local array defined over $\mathbb{Z}_N^d$ and a_∞ its counterpart defined on $\mathbb{Z}^d$, where the elements $\{a_k\}$ have been filled out with zeros for $|k| > q$ up until infinity. The Discrete Fourier Transform (DFT) of a becomes (see Section 2.2)

$$\hat{a}_n := \sum_{k \in \mathbb{Z}_N^d} a_k e^{-j \frac{2\pi}{N} n \cdot k} \tag{3.24}$$

We now take the Z-transform of a_∞ evaluated on the d-dimensional unit torus $\mathbb{T}^d = [-\pi, \pi]^d$:

$$\hat{a}_\infty(\theta) := \sum_{k \in \mathbb{Z}^d} a_k e^{-j \theta \cdot k}, \tag{3.25}$$

where $\theta = (\theta_1, \ldots, \theta_d)$. Comparing (3.24) with (3.25) it is clear that the DFT of a is simply the samples of the Z-transform of a_∞ at the grid points $\theta = \frac{2\pi}{N} n$, for $n \in \mathbb{Z}_N^d$. That is,

$$\hat{a}_n = \hat{a}_\infty\left(\frac{2\pi}{N} n\right), \quad n \in \mathbb{Z}_N^d. \tag{3.26}$$

Given that we are interested in system behaviors as $N \to \infty$, it will be convenient to consider these *generalized Fourier symbols* (Z-transforms) of operators over $\mathbb{Z}^d$, and their behavior in the continuous variable $\theta \in [-\pi, \pi]^d$ rather than for discrete wavenumbers.

For this purpose, let us take the general state space system (3.15) and map the system operators $\mathcal{A}$, $\mathcal{B}$, $\mathcal{C}$ onto $\mathbb{Z}^d$ to obtain $\mathcal{A}_\infty, \mathcal{B}_\infty, \mathcal{C}_\infty$. For example, in the system (3.5), we have $\mathcal{A} = F$. If we let F represent the standard consensus algorithm (3.3), then $\mathcal{A}_\infty = F_\infty$ has the associated function array f_∞, defined just as in (3.4), but filled with infinitely many zero components for $|k| > 1$.

By virtue of the spatial invariance property, $\mathcal{A}_\infty$, $\mathcal{B}_\infty$ and $\mathcal{C}_\infty$ are circulant convolution operators and the Z-transform can be used to *(block) diagonalize* them, see [8]. Then, at each $\theta \in [-\pi, \pi]^d$, we obtain the matrix-valued $\hat{\mathcal{A}}_\infty(\theta)$, $\hat{\mathcal{B}}_\infty(\theta)$ and $\hat{\mathcal{C}}_\infty(\theta)$.

The DFTs $\hat{\mathcal{A}}_n$, $\hat{\mathcal{B}}_n$, $\hat{\mathcal{C}}_n$ of $\mathcal{A}$, $\mathcal{B}$, $\mathcal{C}$ are now precisely the values of $\hat{\mathcal{A}}_\infty(\theta)$, $\hat{\mathcal{B}}_\infty(\theta)$ and $\hat{\mathcal{C}}_\infty(\theta)$ at $\theta = \frac{2\pi}{N} n$, for all wavenumbers $n \in \mathbb{Z}_N^d$.
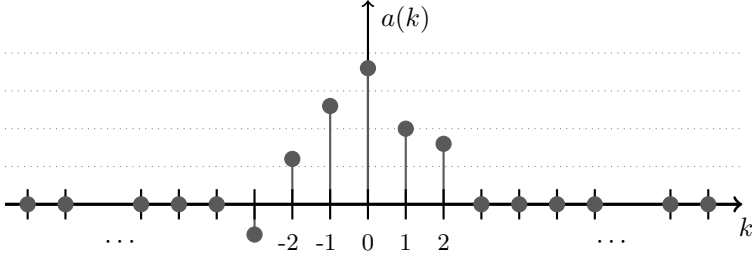
Figure 3.3: Principle for re-defining the local array a onto $\mathbb{Z}$ (compare to Figure 3.2).

3.3.2 $\mathcal{H}_2$ norm evaluation on the infinite lattice

From now on, let us assume that the state space system (3.15) is input-output stable, so that its $\mathcal{H}_2$ norm (3.16) exists. This norm can then be calculated as

$$V = \operatorname{tr}\left(\int_0^\infty \mathcal{B}^* e^{\mathcal{A}^* t} \mathcal{C}^* \mathcal{C} e^{\mathcal{A}t} \mathcal{B} \mathrm{d}t\right).$$

Since $\mathcal{A}, \mathcal{B}$ and $\mathcal{C}$ are circulant convolution operators, their Fourier symbols $\hat{\mathcal{A}}_n, \hat{\mathcal{B}}_n, \hat{\mathcal{C}}_n$ correspond to their eigenvalues. The trace can, according to the discussion in Section 2.1.2, be re-written as

$$V = \operatorname{tr}\left(\sum_{n \in \mathbb{Z}_N^d} \int_0^\infty \hat{\mathcal{B}}_n^* e^{\hat{\mathcal{A}}_n^* t} \hat{\mathcal{C}}_n^* \hat{\mathcal{C}}_n e^{\hat{\mathcal{A}}_n t} \hat{\mathcal{B}}_n \mathrm{d}t\right) \tag{3.27}$$

Now, consider the output operator H^{dav} defined in (3.19). It is easy to verify that its Fourier symbol is $\hat{h}_0 = 0$, and $\hat{h}_n = 1$ for $n \neq 0$. This implies that the output matrix $\hat{\mathcal{C}}_0 = 0$ for all systems we consider (the zero mode is unobservable). Consequently, we can obtain the $\mathcal{H}_2$ norm in (3.27) by summing only over $n \in \mathbb{Z}_N^d \backslash \{0\}$.

Furthermore, following the discussion in the previous section, we can regard the Fourier symbols in (3.27) as subsamples of $\hat{\mathcal{A}}_\infty(\theta), \hat{\mathcal{B}}_\infty(\theta)$ and $\hat{\mathcal{C}}_\infty(\theta)$. Given this relationship, we can state the individual output variances $V_M = V/N^d$ in (3.17), as

$$V_M = \frac{1}{N^d} \sum_{\substack{\theta = \frac{2\pi}{N}n \\ n \in \mathbb{Z}_N^d \backslash \{0\}}} \operatorname{tr}\left(\hat{\mathcal{B}}_\infty^*(\theta) \hat{X}(\theta) \hat{\mathcal{B}}_\infty(\theta)\right). \tag{3.28}$$

where the individual integrals are defined as follows:

Definition 3.2

$$\hat{X}(\theta) := \int_0^\infty e^{\hat{\mathcal{A}}_\infty^*(\theta)t} \hat{\mathcal{C}}_\infty^*(\theta) \hat{\mathcal{C}}_\infty(\theta) e^{\hat{\mathcal{A}}_\infty(\theta)t} \mathrm{d}t \tag{3.29}$$

We call $\hat{X}(\theta)$ the *observability Gramian* at θ.

The observability Gramian at each θ is obtained by solving the Lyapunov equation

$$\hat{\mathcal{A}}_\infty(\theta)^* \hat{X}(\theta) + \hat{X}(\theta)\hat{\mathcal{A}}_\infty(\theta) = -\hat{\mathcal{C}}_\infty(\theta)\hat{\mathcal{C}}_\infty(\theta), \tag{3.30}$$

and is unique and finite provided $\hat{\mathcal{A}}_\infty(\theta)$ is Hurwitz.

For all problem formulations from Section 3.1 that are considered here, $\hat{\mathcal{B}}_\infty(\theta)$ is a vector where one element[1] is 1 and remaining elements are zero. Thus, $\mathrm{tr}\left(\hat{\mathcal{B}}_\infty^*(\theta)\hat{X}(\theta)\hat{\mathcal{B}}_\infty(\theta)\right)$ in (3.28) is just one element of the matrix $\hat{X}(\theta)$ (or the sum of d identical elements). This is a quantity that will be used throughout the following sections and we make the following definition:

Definition 3.3

$$\hat{x}^{\mathrm{tr}}(\theta) := \mathrm{tr}\left(\hat{\mathcal{B}}_\infty^*(\theta)\hat{X}(\theta)\hat{\mathcal{B}}_\infty(\theta)\right) \tag{3.31}$$

Since $\hat{x}^{\mathrm{tr}}(\theta)$ contains all relevant properties of the observability Gramian, we will sometimes, with a slight abuse of terminology, refer to $\hat{x}^{\mathrm{tr}}(\theta)$ simply as "the Gramian".

Now, notice that if the value of $\hat{x}^{\mathrm{tr}}(\theta)$ is bounded for all $\theta \in [-\pi, \pi]^d$, then V_M in (3.28) will remain bounded as $N \to \infty$ and the system in question is to be regarded as *fully coherent*. For the consensus and vehicular formation problems, however, there is typically the single zero eigenvalue at wavenumber $n = 0$ (see Section 5.3.2), which causes a singularity in $\hat{x}^{\mathrm{tr}}(\theta)$ at $\theta = 0$. Even though that mode is unobservable from the system output, the singularity makes the Gramian grow unboundedly for small θ, that is, for small wavenumbers.

For this reason, we use the following appropriate integral to estimate the value of the sum in (3.28) asymptotically:

Definition 3.4

$$I(\Delta) := \int_{\Delta \leq |\theta_1| \leq \pi} \cdots \int_{\Delta \leq |\theta_d| \leq \pi} \hat{x}^{\mathrm{tr}}(\theta) \, \mathrm{d}\theta_1 \cdots \mathrm{d}\theta_d \tag{3.32}$$

where the argument Δ indicates the size of a deleted neighborhood around $\theta = 0$. We recognize the sum in (3.28) as a Riemann sum approximation of the integral (3.32) with volume element $1/N^d$. The integral can therefore be used to bound the sum asymptotically. Consider the following lemma:

Lemma 3.2 *The individual output variances V_M in (3.28) are upper and lower bounded by the integral (3.32) as*

$$I\left(\frac{4\pi}{N}\right) \leq V_M \leq I\left(\frac{2\pi}{N}\right). \tag{3.33}$$

for all $N > \bar{N}$ for some fixed $\bar{N}$.

---

[1]In the vehicular formation case, each "element" is a $d \times d$ diagonal matrix, where each of the d diagonal elements is equal by Assumption 3.6.
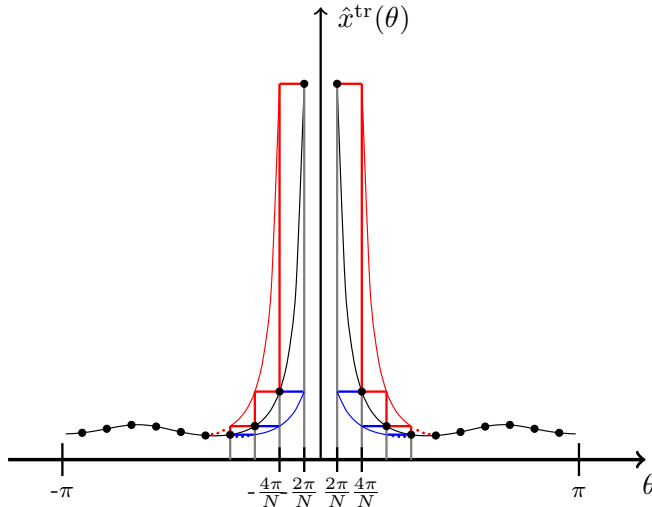
Figure 3.4: Riemann sum approximation in Lemma 3.2.

Proof: *(Full argument provided in the appendix.)* Since the system is assumed input-output stable, the Gramian is continuous and bounded on any compact interval $[\delta, \pi]$ away from zero, and therefore Riemann integrable on that interval. As $\theta \to 0$, that is, for small wavenumbers, the Gramian may grow unboundedly, but is does so montonically. Therefore, on an interval $[\Delta, \delta)$, allowing for $\Delta \to 0$, the Gramian is monotonic and we can bound the sum by standard upper and lower Riemann integral estimates. As N grows large, the part of the sum (3.28) where n is such that $(2\pi n/N) \in [\delta, \pi]$ will converge to the corresponding integral so that, beyond some $\tilde{N}$, the entire sum can be bounded by the upper and lower integral estimates as in (3.33). The integral and the the Riemann sum approximations are illustrated in Figure 3.4.

■

The performance of the consensus and vehicular formation systems can now be evaluated as follows. First, the system operators are re-defined on $\mathbb{Z}^d$ and (block) diagonalized using the Z-transform (3.25). Second, the Lyapunov equation (3.30) is solved to determine $\hat{x}^{\mathrm{tr}}(\theta)$. Bounds on the individual output variances V_M are then found through Lemma 3.2. Next, we derive general expressions for the asymptotic scaling (in N) of the integral (3.32).

3.3.3   Bounds on asymptotic scalings

We are interested in the scaling of the individual output variances V_M in (3.28), with the total number of nodes $M = N^d$ as this number grows large. Using the

integral in (3.32) and the bounds in Lemma 3.2, we can now derive asymptotic scalings of V_M by exploiting properties of the Gramian $\hat{x}^{\mathrm{tr}}(\theta)$.

As we described earlier, V_M will be bounded asymptotically if the value of $\hat{x}^{\mathrm{tr}}(\theta)$ is bounded for all θ. However, when the system has a zero eigenvalue, the Gramian has a singularity and grows unboundedly as $\theta \to 0$. This causes an unfavourable scaling of performance. We give a simple example:

Example 3.1 Consider the standard consensus algorithm (3.3) and for simplicity let the dimension $d = 1$. The Lyapunov equation (3.30) is scalar and solved by

$$\hat{X}(\theta) = \hat{x}^{\mathrm{tr}}(\theta) = \frac{1}{2} \frac{-\hat{h}_\infty^2(\theta)}{\hat{f}_\infty(\theta)} \tag{3.34}$$

for all $\theta \in [-\pi, \pi]$. The array f was given by $f_0 = -2\tilde{f}$, $f_1 = f_{-1} = \tilde{f}$ and $f_k = 0$ for $|k| > 1$ and f_∞ was constructed on $\mathbb{Z}$ by letting $k \to \infty$. Its Z-transform (3.25) is then:

$$\hat{f}_\infty(\theta) = \tilde{f}(-2 + e^{j\theta} + e^{-j\theta}) = -2\tilde{f}(1 - \cos\theta). \tag{3.35}$$

Recall, the output H^{dav} is defined such that $\hat{h}_\infty(\theta) = 1$ for $\theta \neq 0$ and $\hat{h}_\infty(0) = 0$.

Substituting this into (3.39), the integral in (3.32) becomes

$$I(\Delta) = \frac{1}{4\tilde{f}} \int_{\Delta \leq |\theta| \leq \pi} \frac{1}{1 - \cos\theta} d\theta.$$

The lower bound in (3.33) is then

$$I\left(\frac{4\pi}{N}\right) = \frac{-1}{2\tilde{f}} \left[\cot\frac{\theta}{2}\right]_{\frac{4\pi}{N}}^{\pi} = \frac{1}{2\tilde{f}} \cot\frac{2\pi}{N},$$

A series expansion of the cotangent function reveals that this scales as $\frac{1}{\tilde{f}} N$ asymptotically. The same holds for the upper bound in (3.33). This is in line with the result in [7, Table 1].

In general, let us assume that the Gramian is such that

$$\hat{x}^{\mathrm{tr}}(\theta) \sim \frac{1}{\beta^{p/2}} \frac{1}{(\theta_1^2 + \theta_2^2 + \cdots + \theta_d^2)^{p/2}}, \tag{3.36}$$

for some non-negative p. The number p characterizes the order of the singularity of the Gramian at $\theta = 0$. That is, how fast $\hat{x}^{\mathrm{tr}}(\theta)$ grows as $\theta \to 0$. Throughout the thesis, we let the notation $u(\theta) \sim v(\theta)$ imply that $\underline{c}v(\theta) \leq u(\theta) \leq \bar{c}v(\theta)$, for some fixed constants $\underline{c}, \bar{c}$ and all $\theta \in [\pi, \pi]^d$. We have also introduced β as an algorithm parameter that reflects control effort (c.f. $\tilde{f}$ in Example 3.1).

Example 3.2 The operator for the standard consensus algorithm (3.3) has the (generalized) Fourier symbol $\hat{f}_\infty(\theta) = -2\tilde{f}(d - \cos\theta_1 - \cdots - \cos\theta_d)$. Using standard bounds of the cosine function, it is straightforward to show that the Gramian $\hat{X}(\theta) = \hat{x}^{\text{tr}}(\theta) = \frac{-1}{\hat{f}(\theta)}$ satisfies (3.36) with $p = 2$.

The number p, that is, the order of the singularity at $\theta = 0$ of $\hat{x}^{\text{tr}}(\theta)$, determines the coherence properties for a given system. If $p = 0$, the system is fully coherent. Otherwise, performance depends on the spatial dimension d of the network. We now state the main result of this section:

Lemma 3.3 *Assume $\hat{x}^{\text{tr}}(\theta)$ defined in (3.31) fulfills (3.36). The individual output variances (3.28) then scale asymptotically as*

$$V_M \sim \frac{1}{\beta^{p/2}} \begin{cases} N^{p-d} & \text{if } d \neq p \\ \log N & \text{if } d = p \\ 1 & \text{if } d > p \end{cases} \tag{3.37}$$

up to some constant, which is independent of the lattice size N and the algorithm parameter β.

Proof: First, substitute the approximation (3.36) into the integral $I(\Delta)$ in (3.32) and denote the resulting integral $\tilde{I}(\Delta)$. Using hyperspherical coordinates we obtain:

$$\tilde{I}(\Delta) = \int_{\Delta \leq |\theta_1| \leq \pi} \cdots \int_{\Delta \leq |\theta_d| \leq \pi} \frac{1}{\beta^{p/2}} \frac{1}{(\theta_1^2 + \cdots + \theta_d^2)^{p/2}} \mathrm{d}\theta_1 \cdots \mathrm{d}\theta_d$$

$$= \int_\Delta^\pi \int_0^{2\pi} \int_0^\pi \cdots \int_0^\pi \frac{1}{\beta^{p/2} r^p} r^{d-1} \sin^{d-2}\phi_1 \cdots \sin\phi_{d-2} \mathrm{d}r \mathrm{d}\phi_{d-1} \cdots \mathrm{d}\phi_1$$

$$= \frac{1}{\beta^{p/2}} \mathcal{V}_d \int_\Delta^\pi r^{d-p-1} \mathrm{d}r, \quad (3.38)$$

where $\mathcal{V}_d$ is a constant that is proportional to the the volume of the d-dimensional unit ball, but independent of all other variables.

By Lemma 3.2, we know that the individual output variances V_M are bounded as

$$\underline{c}\tilde{I}\left(\frac{4\pi}{N}\right) \leq I\left(\frac{4\pi}{N}\right) \leq V_M \leq I\left(\frac{2\pi}{N}\right) \leq \bar{c}\tilde{I}\left(\frac{2\pi}{N}\right),$$

for all $N \geq \bar{N}$ for some $\bar{N}$, and with the constants $\underline{c}, \bar{c}$ from (3.36). Now, substituting for Δ in (3.38) the values $\frac{2\pi}{N}$ and $\frac{4\pi}{N}$ from these upper and lower bounds gives that

$$
V_M \leq \bar{c} \mathcal{V}_d \frac{1}{\beta^{p/2}} \begin{cases} \frac{1}{p-d} \pi^{d-p} \left(\left(\frac{N}{2}\right)^{p-d} - 1 \right) & \text{if } d \neq p \\ \log N - \log 2 & \text{if } d = p \end{cases}
$$

$$
V_M \geq \underline{c} \mathcal{V}_d \frac{1}{\beta^{p/2}} \begin{cases} \frac{1}{p-d} \pi^{d-p} \left(\left(\frac{N}{4}\right)^{p-d} - 1 \right) & \text{if } d \neq p \\ \log N - \log 4 & \text{if } d = p \end{cases}
$$

Noticing that these bounds are identical up to a constant for any given d, the result (3.37) follows.

∎

In the following sections we will show that all input-output stable formulations of the systems considered in this chapter give observability Gramians that satisfy (3.36) with $p \in \{0, 2, 4\}$.

3.4 Evaluation of dynamic feedback

The objective of this chapter is to study the dynamic feedback laws introduced in Section 3.1, to determine whether they give different coherence properties in large-scale networks than static feedback. We now use the mathematical framework introduced in the previous section to systematically evaluate these feedback laws.

We procede as follows. First, we examine stability properties of the dynamic feedback protocols, in order to identify any feedback configurations that de-stabilize the systems as networks grow large and which are therefore infeasible. We then follow the approach introduced in Section 3.3 to derive asymptotic performance scalings for feasible configurations of the consensus and the vehicular formation problems separately. We end the section by discussing some practical implications of our results as well as the role of control effort bounds.

3.4.1 Conditions for input-output stability of dynamic feedback

The performance measure (3.17) is only meaningful if the system (3.15) is input-output stable. By the theory of Section 3.3.1, this is equivalent to ensuring that the individual Fourier symbols are stable in their own right. We begin by re-stating the following Theorem from previous work:

Theorem 3.4 *[8, Corollary 1] The system* (3.15) *on $\mathbb{Z}_N^d$ is exponentially stable if and only if for each $n \in \mathbb{Z}_N^d$, the matrix $\hat{\mathcal{A}}_n$ is stable.*

Proof: See [8, Theorem 1] and note that the group $\mathbb{Z}_N^d$ is compact.

∎

In our case, since the mode at $n = 0$ is unobservable from the considered output, input-output stability is guaranteed by ensuring $\hat{\mathcal{A}}_n$ is stable for $n \in \mathbb{Z}_N^d \backslash \{0\}$.

Now, since we are evaluating these systems asymptotically, we must require that they remain input-output stable for any given lattice size N, as this number grows. Since the Fourier symbols $\hat{\mathcal{A}}_n$ can be seen as subsamples of $\hat{\mathcal{A}}_\infty(\theta)$, see Section 3.3.1, the only way to ensure stability for *any* lattice size N is to make sure that $\hat{\mathcal{A}}_\infty(\theta)$ is stable for any θ away from zero:

Corollary 3.5 *The system* (3.15) *on* $\mathbb{Z}_N^d$ *with output defined as in* (3.19) *will be input-output stable for any lattice size N if and only if the matrix* $\hat{\mathcal{A}}_\infty(\theta)$ *is stable for all* $\theta \in [-\pi, \pi]^d \backslash \{0\}$.

In the case of static feedback, it is easy to verify that the systems will be input-output stable for any choice of feedback operators F, G in (3.5) and (3.11) such that $\hat{f}_\infty(\theta)$, $\hat{g}_\infty(\theta) < 0$ for all $\theta \in [-\pi, \pi]^d \backslash \{0\}$. With dynamic feedback, however, the stability conditions are less straightforward, and it turns out that not all feedback configurations can guarantee stability as networks grow large. We now present such conditions on the feedback structures for the consensus and vehicular formation problems.

Consensus

Consider the consensus protocol (3.6) with fixed feedback operators A, B, F. Corollary 3.5 can only be fulfilled under certain conditions on these operators. The following theorem provides necessary conditions for stability:

Theorem 3.6 *The system* (3.6) *can be input-output stable with respect to the output* (3.19) *for any lattice size N only if at least one of the following conditions holds:*

a) The operator B is symmetric, implying that $\hat{b}_\infty(\theta)$ *is real*

b) The operator A involves absolute feedback, *that is, A does not satisfy* (3.8).

Proof: See appendix.

∎

Vehicular formations

For the vehicular formations, we consider the cases with relative and absolute state feedback (see Assumption 3.4) separately and provide necessary conditions for stability.

Theorem 3.7 *Assume that only relative measurements of the states x and v are available, so that the operators F and G have the property (3.8). The system (3.13) can be input-output stable with respect to the output (3.19) for any lattice size N only if at least one of the following conditions holds:*

a) The operator $B = 0$, while $A \neq 0$

b) The operator A involves absolute feedback, *that is, A does not fulfill (3.8).*

Proof: See appendix.

■

Theorem 3.7 implies that integral control based on position measurements cannot be implemented for arbitrarily large networks, unless there is built-in "self-damping" of the memory state through an absolute feedback term in A. If absolute measurements of position or velocity are available to the controller, or if viscous damping according to (3.14) is present, the criterion b) can be relaxed. Integral control based on *absolute* position measurements, however, cannot be implemented regardless of choice of A, unless absolute feedback from velocity measurements is present:

Theorem 3.8 *If the operator B involves absolute feedback from positions x (i.e., B does not have the property (3.8)), a necessary condition for stability of the system (3.13) for any lattice size N is that the control also involves absolute feedback from velocities v.*

Proof: See appendix.

■

Remark 3.2 The stability criteria in Theorems 3.6 – 3.8 hold under the assumption of *fixed* feedback laws, that is, that feedback gains do not change with the lattice size N. If specific gains can increase arbitrarily as the network grows, stability can, in theory, be maintained for any size of the network. We are, however, interested in asymptotic scalings of performance and therefore require the feedback laws to be "robust" with respect to system size N.

3.4.2   Performance evaluation for the consensus case

We begin by deriving the asymptotic performance scaling for the static case (3.2). In this case, the Lyapunov equation (3.30) is a scalar equation, which is solved by

$$\hat{X}(\theta) = \hat{x}^{\text{tr}}(\theta) = \frac{-1}{2\text{Re}\{\hat{f}_\infty(\theta)\}}, \tag{3.39}$$

The real part of the generalized Fourier symbol (3.25) of F_∞ is

$$\begin{aligned} \text{Re}\{\hat{f}_\infty(\theta)\} &= \sum_{k\in\mathbb{Z}^d} f_k \cos(\theta \cdot k) \\ &= \sum_{k\in\mathbb{Z}^d} f_k \left[1 - (1 - \cos(\theta \cdot k))\right] \\ &= -\sum_{k\in\mathbb{Z}^d} f_k \left(1 - \cos(\theta \cdot k)\right), \end{aligned} \tag{3.40}$$

where we have used Assumption 3.3 of relative measurements, which implies that $\sum_{k\in\mathbb{Z}^d} f_k = \sum_{k\in\mathbb{Z}_N^d} f_k = 0$. Now, since for any x, it holds that $1 - \cos x \leq x^2$, we have

$$\begin{aligned} \left|\sum_{k\in\mathbb{Z}^d} f_k \left(1 - \cos(\theta \cdot k)\right)\right| &\leq \sum_{k\in\mathbb{Z}^d} |f_k| \left(k_1\theta_1 + \cdots + k_d\theta_d\right)^2 \\ &\leq \sum_{0\neq k\in\mathbb{Z}^d} ||f||_\infty q^2 \left(|\theta_1| + \cdots + |\theta_d|\right)^2 \\ &\leq (2q)^d ||f||_\infty q^2 (2d+1)(\theta_1^2 + \cdots + \theta_d^2), \quad (3.41) \end{aligned}$$

where the second inequality follows from the locality assumption (3.7) and the third from the fact that for any d numbers:

$$\begin{aligned} \left(\sum_{i=1}^d x_i\right)^2 &= \sum_{i=1}^d x_i^2 + \sum_{i=1}^d \sum_{j\neq i} x_i x_j \leq \sum_{i=1}^d x_i^2 + \sum_{i=1}^d \sum_{j\neq i}(x_i^2 + x_j^2) \\ &\leq \sum_{i=1}^d x_i^2 + 2d\sum_{i=1}^d x_i^2 = (2d+1)\sum_{i=1}^d x_i^2. \end{aligned} \tag{3.42}$$

The corresponding lower bound is established by considering a "minimal" feedback strategy; nearest neighbor look-ahead control, $u_k = \tilde{f}[(x_{(k_1+1,\ldots,k_d)} - x_k) + \cdots + (x_{(k_1,\ldots,k_d+1)} - x_k)]$. The corresponding Fourier symbol is:

$$\hat{f}_\infty(\theta) = -\tilde{f}\left(d + \sum_{i=1}^d e^{-j\theta_i}\right) = -\tilde{f}\sum_{i=1}^d (1 - \cos\theta_i) - j\tilde{f}\sum_{i=1}^d \sin\theta_i, \tag{3.43}$$

and $\text{Re}\{\hat{f}_\infty(\theta)\} = -\tilde{f} \sum_{i=1}^d (1 - \cos\theta_i)$. Using the fact that for any $x \in [-\pi, \pi]$, $1 - \cos x \geq \frac{2}{\pi^2} x^2$ we get

$$\tilde{f} \sum_{i=1}^d (1 - \cos\theta_i) \geq \tilde{f} \sum_{i=1}^d \frac{2}{\pi^2} \theta_i^2 = \frac{2d}{\pi^2} \tilde{f}(\theta_1^2 + \theta_2^2 + \cdots + \theta_d^2). \tag{3.44}$$

Combining (3.41) and (3.44) with (3.39), we obtain

$$\frac{1}{2} \frac{1}{(2q)^d ||f||_\infty q^2 (2d+1)(\theta_1^2 + \cdots + \theta_d^2)} \leq \hat{x}^{\text{tr}}(\theta) \leq \frac{1}{2} \frac{1}{\frac{2}{\pi^2} \tilde{f} d(\theta_1^2 + \cdots + \theta_d^2)}. \tag{3.45}$$

Now, we can identify the algorithm parameter $\beta = \tilde{f} = c||f||_\infty$ for some constant $c \leq 1$. These parameters are bounded in terms of control effort, which we discuss in Section 3.4.5. Remaining coefficients are independent of network size N, and we therefore have that

$$\hat{x}^{\text{tr}}(\theta) = \frac{-1}{2\text{Re}\{\hat{f}_\infty(\theta)\}} \sim \frac{1}{\beta} \frac{1}{(\theta_1^2 + \cdots + \theta_d^2)}, \tag{3.46}$$

that is, $\hat{x}^{\text{tr}}(\theta)$ satisfies (3.36) with $p = 2$. The individual output variances under the feedback scheme (3.2) thus scale according to Lemma 3.3 with $p = 2$.

Note that the performance of the consensus system with static feedback is independent of any imaginary parts of the Fourier symbols $\hat{f}_\infty(\theta)$, as seen from (3.39). It is therefore independent of whether the feedback operator F is symmetric or not. When answering the question of whether dynamic feedback, that is, an additional layer of control, may improve performance, it is therefore reasonable to make the following assumption:

Assumption 3.7 The operator F in the dynamic consensus protocol (3.6) is symmetric, that is, it fulfills the properties listed in Assumption 3.5.

Now we turn to the case of dynamic feedback (3.6), and assume that the choice of operators A, B, F is feasible, that is, that the stability conditions from Section 3.4.1 are fulfilled. The solution to the Lyapunov equation (3.30) then gives that

$$\hat{x}^{\text{tr}}(\theta) = \frac{-1}{2\hat{f}_\infty(\theta) + 2\varphi^c(\hat{a}_\infty(\theta), \hat{f}_\infty(\theta), \hat{b}_\infty(\theta))}, \tag{3.47}$$

where $\varphi^c(\hat{a}_\infty(\theta), \hat{f}_\infty(\theta), \hat{b}_\infty(\theta))$ is a function of the respective Fourier symbols. This Gramian would give an asymptotic scaling different from (3.46) if the function φ^c were non-zero and scaled differently in θ than $\hat{f}_\infty(\theta)$, for which we established $\hat{f}_\infty(\theta) \sim -\beta(\theta_1^2 + \ldots + \theta_d^2)$. This is, however, not the case for any admissible configuration of the feedback operators A and B. Consider the following lemma:

Lemma 3.9 *For any feasible choice of the operators A, B, F in (3.6) satisfying Assumptions 3.1 - 3.3, 3.7, the function φ^c in (3.47) is such that*

$$\hat{f}_\infty(\theta) + \varphi^c(\hat{a}_\infty(\theta), \hat{f}_\infty(\theta), \hat{b}_\infty(\theta)) \sim -\beta(\theta_1^2 + \ldots + \theta_d^2). \qquad (3.48)$$

Therefore, $\hat{x}^{\mathrm{tr}}(\theta)$ in (3.47) will fulfill (3.36) with $p = 2$ for any design of the dynamic feedback.

Proof: See appendix.

∎

The asymptotic performance scaling will thus be unchanged compared to static feedback. Rewriting the asymptotic scalings from Lemma 3.3 in terms of total network size $M = N^d$ gives the result in Theorem 3.1.

3.4.3   Performance evaluation for vehicular formations

Following the outline of the previous section, we begin by evaluating the static feedback case (3.11). The solution to the Lyapunov equation (3.30) gives that

$$\hat{x}^{\mathrm{tr}}(\theta) = \frac{d}{2\hat{f}_\infty(\theta)\hat{g}_\infty(\theta)}. \qquad (3.49)$$

In the case of *relative position and relative velocity feedback*, each of $\hat{f}_\infty(\theta)$ and $\hat{g}_\infty(\theta)$ looks like $\mathrm{Re}\{\hat{f}_\infty(\theta)\}$ in the consensus case, see (3.46). We can therefore bound (3.49) as

$$\hat{x}^{\mathrm{tr}}(\theta) = \frac{d}{2\hat{f}_\infty(\theta)\hat{g}_\infty(\theta)} \sim \frac{1}{\beta^2(\theta_1^2 + \ldots + \theta_d^2)^2}.$$

The individual output variances thus scale as in Lemma 3.3 with $p = 4$.

In the case of *absolute velocity and relative position feedback*, we can use (3.40) to write $\hat{g}_\infty(\theta) = \hat{g}_0 - \sum_{k \in \mathbb{Z}^d} g_k \left(1 - \cos(\theta \cdot k)\right)$, where $\hat{g}_0 = \sum_{k \in \mathbb{Z}^d} g_k < 0$ to ensure stability. In this case, $\hat{g}_\infty(\theta)$ is uniformly bounded while $\hat{f}_\infty(\theta)$ scales as before. We then have that $\hat{x}^{\mathrm{tr}}(\theta) \sim 1/(\beta \left(\theta_1^2 + \ldots + \theta_d^2\right))$. The same argument holds if absolute position feedback is available, but velocity feedback is relative. In these cases, performance scales as in Lemma 3.3 with $p = 2$.

In cases where there is *absolute feedback from both position and velocity*, $\hat{f}_\infty(\theta)$ and $\hat{g}_\infty(\theta)$ are both uniformly bounded. Therefore, $\hat{x}^{\mathrm{tr}}(\theta)$ in (3.49) remains bounded for all $\theta \in [-\pi, \pi]^d$ (so $p = 0$ in Lemma 3.3) and the system is fully coherent.

These results for the static case, which are in line with those in [7, Table 1], are summarized in Theorem 3.1.

Now, consider dynamic feedback on the form (3.13). Provided the feedback configuration is feasible, that is, that the stability conditions from Section 3.4.1 are fulfilled, the solution to the Lyapunov equation (3.30) gives that

$$\hat{x}^{\mathrm{tr}}(\theta) = \frac{d}{2\hat{f}\hat{g} + 2\varphi^v(\hat{a}, \hat{b}, \hat{c}, \hat{f}, \hat{g})}, \tag{3.50}$$

where $\varphi^v(\hat{a}, \hat{b}, \hat{c}, \hat{f}, \hat{g})$ is a function of the respective Fourier symbols (we have omitted the ∞-subscripts and the θ-arguments for notational compactness).

First, we note that in the case of *absolute feedback from both position and velocity*, dynamic feedback can yield a fully coherent system just like static feedback. This can be recognized by noting that if (3.49) is bounded, then so is (3.50) if φ^v is non-negative. This is easy to achieve, for example by choosing A as in the standard consensus algorithm (3.3) and $C = -c_o I$. In this case we have, using (3.71), $\varphi^v \sim c_o g_o$, where g_o is the absolute feedback term in G.

We analyze (3.50) for remaining cases below:

Relative position and relative velocity feedback

In order for $\hat{x}^{\mathrm{tr}}(\theta)$ in (3.50) to give a different asymptotic scaling than (3.49), the function φ^v would need to scale differently in θ from the product $\hat{f}_\infty(\theta)\hat{g}_\infty(\theta)$, for which we established $\hat{f}_\infty(\theta)\hat{g}_\infty(\theta) \sim \beta^2 \left(\theta_1^2 + \ldots + \theta_d^2\right)^2$. This is, however, not the case for any feasible configuration of the operators A, B, C, F, G with feedback only from relative measurements of position and velocity. Consider the following lemma:

Lemma 3.10 *For any feasible choice of the operators A, B, C, F, G in (3.13) with* only *relative feedback in B, C, F, G, the function φ^v in (3.50) is such that*

$$\hat{f}\hat{g} + \varphi^v(\hat{a}, \hat{b}, \hat{c}, \hat{f}, \hat{g}) \sim \beta^2(\theta_1^2 + \ldots + \theta_d^2)^2, \tag{3.51}$$

Therefore, $\hat{x}^{\mathrm{tr}}(\theta)$ in (3.50) will satisfy (3.36) with $p = 4$ for any design of the dynamic feedback.

Proof: See appendix.

■

We conclude that in the case of relative position and relative velocity feedback, dynamic feedback on the form (3.13) cannot improve asymptotic performance scaling compared to static feedback.

Remark 3.3 Certain choices of A, B, C, F, G in (3.13) may make it seem as if one could achieve $\varphi^v \sim -\beta(\theta_1^2 + \ldots + \theta_d^2)^2$, and thereby make $\hat{x}^{\mathrm{tr}}(\theta)$ scale as in (3.37) with $p = 2$. For example, if $A = 0$, it holds $\varphi^v(\hat{a}, \hat{b}, \hat{c}, \hat{f}, \hat{g}) = \hat{b} + \hat{c}\hat{g}$ and one could choose B as the standard consensus operator (3.3). However, such a choice always

de-stabilizes the system at some given system size N, as seen from Theorem 3.7. The performance metric (3.17) is therefore not defined asymptotically.

Absolute position and relative velocity feedback

By Theorem 3.8 it is not possible to design a stable distributed integral controller based on absolute measurements of position, unless absolute velocity measurements are available. Dynamic feedback on the form (3.13) can therefore not improve performance compared to static feedback in this case:

Lemma 3.11 *For any feasible choice of the A, B, C, F, G in (3.13) with absolute position and relative velocity feedback, the denominator in (3.50) satisfies*

$$\hat{f}\hat{g} + \varphi^v(\hat{a}, \hat{b}, \hat{c}, \hat{f}, \hat{g}) \sim \beta(\theta_1^2 + \ldots + \theta_d^2). \tag{3.52}$$

Therefore, (3.50) will satisfy (3.36) with $p = 2$ for any design of the dynamic feedback.

Proof: See appendix.

∎

Relative position and absolute velocity feedback

In this case, we first consider the distributed averaging proportional integral (DAPI) controller (3.12) for the 1-dimensional vehicular platoon. The solution to the Lyapunov equation yields

$$\hat{x}_{\text{DAPI}}^{\text{tr}}(\theta) = \frac{1}{2\hat{f}\hat{g} - 2\frac{\hat{c}\hat{f}(\hat{a}+\hat{g})}{\hat{a}^2+\hat{g}\hat{a}-\hat{f}}}, \tag{3.53}$$

where we have, again, left out the $\infty-$subscript and the arguments of the individual Fourier symbols.

By Assumption 3.5, A and F in the DAPI algorithm are just standard consensus operators with Fourier symbols as in (3.35), while $G = -g_o I$ and $C = -c_o I$, with $c_o, g_o > 0$ to ensure stability. Inserting into (3.53) yields (after some simplifications):

$$\hat{x}_{\text{DAPI}}^{\text{tr}}(\theta) = \frac{1}{4g_o f_+(1 - \cos\theta) + 2\frac{c_o g_o f_+ + 2c_o f_+ a_+(1-\cos\theta)}{f_+ + a_+ g_o + 2a_+^2(1-\cos\theta)}},$$

which is uniformly bounded in θ. By Lemma 3.3, the 1D vehicular platoon with DAPI control is therefore *fully coherent*. This is in contrast to static feedback, which for this feedback type yields the asymptotic performance scaling in (3.22), and therefore requires 3 spatial dimensions to be fully coherent.

Other designs of the dynamic feedback in (3.13) with absolute velocity measurements can give the same result as the DAPI strategy. In particlular, G and C can include feedback from velocity errors with respect to neighboring vehicles and B can be non-zero. To achieve full coherence, however, all of these algorithms require perfect measurements of the velocities. We discuss such limitations in Section 3.4.4.

The asymptotic performance scalings for all cases of the vehicular formation algorithm with static and dynamic feedback are summarized in Theorem 3.1, where they have been re-written in terms of total network size $M = N^d$.

3.4.4   Limitations of distributed integral control

In the previous section, we established that dynamic feedback such as the DAPI algorithm (3.12) can yield a fully coherent vehicular formation in any spatial dimension provided that it has access to absolute measurements of velocities with respect to a global reference frame. This situation is reasonable in actual vehicular platoons, where one can assume that each vehicle's speedometer can provide absolute velocity measurements, while absolute position data, which would have to rely on GPS, is less readily available.

An intuitive explanation to this result is that a dynamic feedback protocol can serve as a distributed integral controller, which integrates absolute measurements of velocities in time to yield a substitute for absolute position data. With absolute data from both position and velocity, formations are known to be fully coherent. However, this strategy is essentially so-called "dead reckoning" and, as may be intuitively evident, it is sensitive to faulty measurements.

One issue arises when different controllers' memory states z_k diverge due to slight measurement errors. This issue appears in completely decentralized integral control, but can be solved through distributed averaging of the memory states between controllers, see e.g. [5]. In our case, distributed averaging is achieved by allowing A in (3.13) to be a consensus-type operator, as in the DAPI example (3.12).

Unfortunately, though, measurement errors still cause deteriorated coherence properties in distributed integral control. As a simple analysis, consider the case where the velocity measurements in (3.12) are subject to white measurement noise w_k^m, in addition to the previously assumed process noise w_k in (3.9). We get:

$$\ddot{x}_k = z_k + f_+(x_{k+1} - x_k) + f_-(x_{k-1} - x_k) - g_o v_k + w_k$$
$$\dot{z}_k = a_+(z_{k+1} - z_k) + a_-(z_{k-1} - z_k) - c_o v_k + \varepsilon w_k^m, \qquad (3.54)$$

where ε is a scaling factor. Since the input matrix $\mathcal{B}$ in (3.15) has changed, it now holds that $\text{tr}\left(\hat{\mathcal{B}}_\infty^*(\theta)\hat{X}(\theta)\hat{\mathcal{B}}_\infty(\theta)\right) = \hat{x}_{\text{DAPI}}^{\text{tr}}(\theta) + \hat{x}^z(\theta)$, where $\hat{x}_{\text{DAPI}}^{\text{tr}}(\theta)$ was given in (3.53) and

$$\hat{x}^z(\theta) = \varepsilon^2 \frac{\hat{a} + \hat{g}}{2(-\hat{a}\hat{f})(\hat{a}\hat{c} + \hat{c}\hat{g} + \hat{f}\hat{g} - \hat{a}\hat{g}^2 - \hat{a}^2\hat{g})}. \qquad (3.55)$$

Inserting the Fourier symbols from Section 3.4.3 reveals that $\hat{x}^z(\theta) \sim \varepsilon^2/(a_+ f_+(1-\cos\theta)^2)$, and by the bounds established in Section 3.4.2, it holds $\hat{x}^z(\theta) \sim \varepsilon^2/(\beta^2\theta^4)$. By Lemma 3.3, the individual output variances then scale like $V_M \sim (\varepsilon^2/\beta^2)N^3$ in the 1-dimensional platoon. Through a simple modification of the algorithm, for example an addition of the terms $b_+(x_{k+1} - x_k) + b_-(x_{k+1} - x_k)$ to the z-dynamics in (3.54), we can instead obtain

$$V_M \sim \frac{\varepsilon^2}{\beta}N. \tag{3.56}$$

If the noise is small relative the feedback gains (making the quotient ε/β small), variances remain small, but their scaling is unfavorable, preventing the system from being fully coherent.

The result (3.56) shows that, unless measurements are faultless, performance still scales badly asymptotically in 1-dimensional vehicular platoons. This indicates that the limitation to performance of large-scale networks relying (partly) on relative feedback described in [7] remains and cannot be alleviated in practice using dynamic feedback on the form (3.13).

However, for moderately sized platoons, the performance measure in (3.17) can still be improved in absolute terms, in particular if the factor ε is small. In Figure 6.3 we compare simulations of a 100-vehicle platoon with, respectively, static feedback as in (3.10) and dynamic feedback of the type (3.54) (with $b_+(x_{k+1} - x_k) + b_-(x_{k+1} - x_k)$ added to the z-dynamics.) We note that the best performance is achieved with the DAPI-type dynamic feedback, despite noisy measurements.

3.4.5   Control effort bounds

In the above derivations, we introduced the algorithm parameter β, which reflects the size of the feedback gains. This parameter affects the performance scaling, as evident from our main result in Theorem 3.1. In particular, if feedback gains, and thereby β, could be increased unboundedly and at the rate M (or $M^{3/2}$ in the case of (3.21)), coherence could be achieved in any spatial dimension. This is clearly not feasible in any realistic control problem, where the amount of control effort is bounded. In fact, the feedback array elements are bounded by the total control effort at each network site, which we quantify through:

$$\mathbb{E}\{u_k^* u_k\}, \tag{3.57}$$

that is, the steady state variance of the control signal at each network site. In [7, Lemma 5.1], such bounds are presented for the case of static feedback. Here, we present bounds for the dynamic feedback case, but limit the analysis to the consensus algorithm with symmetric feedback for the sake of brevity:
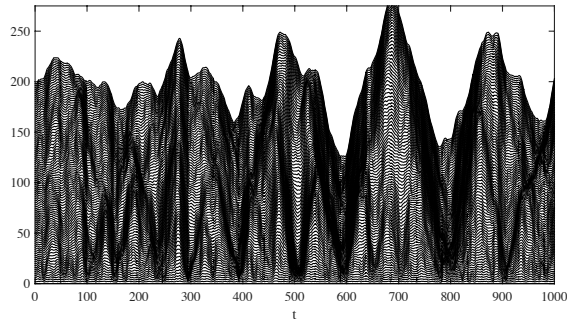
(a) Static feedback, rel. velocity, rel. position
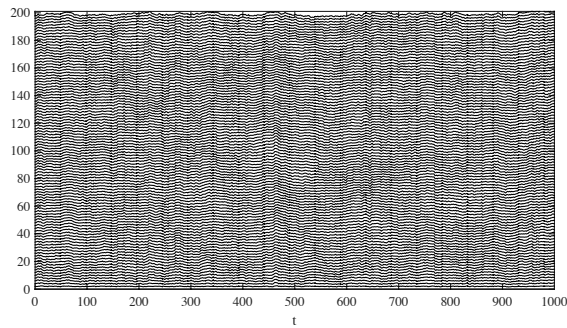
(b) Static feedback, abs. velocity, rel. position
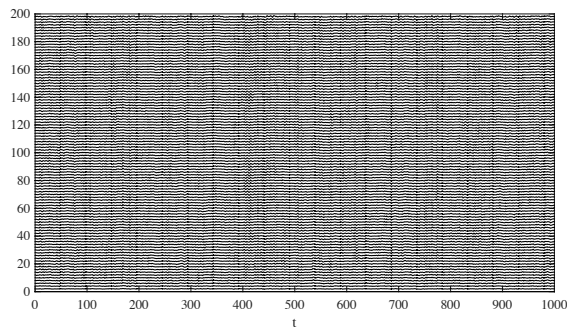
(c) Dynamic feedback, abs. velocity, rel. position

Figure 3.5: Vehicle position trajectories (relative to lead vehicle) for a 100 vehicle formation subjct to random disturbances. With only relative state measurements, the formation has an accordion-type motion (a). Such motion is also present to a lesser extent in (b), which displays the static feedback law in (3.10) with absolute velocity and relative position feedback. With dynamic feedback (c) the formation is more coherent, even though measurement noise is present. In the example $\varepsilon = 0.1$, and all feedback gains are 1.

Lemma 3.12 *Consider the consensus problem with dynamic feedback* (3.6), *where the feedback operators A, B, F satisfy Assumptions 3.2 and 3.5. The following bounds hold:*

$$\mathbb{E}\{u_k^* u_k\} \geq \frac{1}{2}||f||_\infty \tag{3.58a}$$

$$\mathbb{E}\{u_k^* u_k\} \geq \sqrt{\left(\frac{||a||_\infty}{4}\right)^2 + \frac{||b||_\infty}{4(2q)^d}} - \frac{||a||_\infty}{4} \tag{3.58b}$$

Proof: See appendix.

■

Note that the constants in the bounds are independent of network size. We can conclude that the asymptotic scalings for the consensus problem in Theorem 3.1 will apply to any algorithm with control effort constraints.

3.5   Discussion

We now discuss some implications of our main results along with key limitations and open questions.

3.5.1   Limitations of dynamic feedback

The main results of this chapter say that for consensus as well as for vehicular formation systems, it is not possible to design a dynamic feedback protocol on the forms (3.6) and (3.13), based on relative state measurements, that exhibits better coherence properties than static, memoryless feedback. In this sense, the fundamental performance limitation of local feedback that was derived in [7] remains valid also in the case where the controller at each site has a single memory state. In the most problematic case, a 1-dimensional vehicle platoon, these limitations imply that even though the network is stable and has only small and well-regulated errors between neighboring nodes (see Figure 3.6), it cannot be made coherent on a large scale [7]. Instead, it will exhibit an "accordion-type" motion, as displayed in Figure 3.5a. We remark that the performance of a given network depends strongly on the lattice dimension or, in other words, on how well-interconnected the network is. For example, a vehicle platoon with relative feedback can, in theory, be fully coherent if its feedback links build up a 5-dimensional lattice.

If the controller, however, has access to absolute state information at each network site, we showed that a dynamic feedback protocol can be designed so that it suffices to have absolute information of one of the states to achieve full coherence in a 1-dimensional formation, provided that measurement is noiseless. In contrast, a static feedback protocol requires absolute measurements of all states. This implies
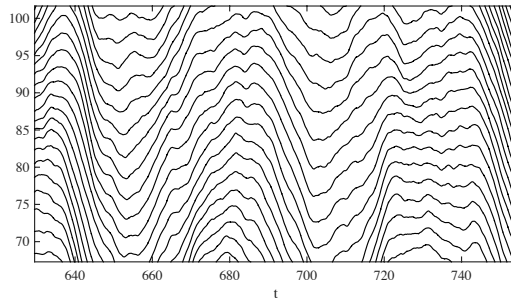
Figure 3.6: Zoomed-in view of position trajectories in a 100 vehicle formation with only relative feedback. Locally, errors are well-regulated. The system is, for example, string stable (see Example 1.1). On a global scale, however, the platoon lacks coherence, as seen in Figure 3.5a. We remark that the same comparison was also made in [7].

that a distributed integral controller utilizing absolute measurements of velocity can, in theory, make a 1-dimensional vehicular platoon fully coherent, even though position is measured locally. While this result requires perfect velocity measurements to hold, it indicates that dynamic feedback can improve coherence, and thus rigidity and throughput, in large vehicular platoons, where velocity information is typically more readily available than position data.

The reason for this apparent performance improvement in the double-integrator system (3.9) is that the dynamic feedback law serves as a distributed integral controller, that integrates absolute measurements of one state to yield a substitute for an absolute measurement of the other state. Intuitively, this idea can be extended to systems with n-integrator dynamics. In that case, $n-1$ internal controller states would be required to integrate one absolute state measurement and thereby make absolute feedback of all states available. In practice, however, such a "dead reckoning" strategy performs badly due to measurement noise and bias.

In the process of deriving these results, we showed that several classes of dynamic feedbacks will de-stabilize large networks, in particular in the case where only relative, local, measurements are available. Therefore, many distributed dynamic feedback laws that may work well for small formations, will become unstable if the formation grows. In general, we show that this can be avoided if absolute feedback is present, either from the physical states or from the internal memory state.

3.5.2 Model extensions

We made a number of limiting assumptions in the present study, partly to limit the scope and partly for tractability purposes. The limitation of the scope to dynamic feedback laws with a single memory state is arguably the most important restriction, and for a complete evaluation of dynamic feedback, the number of memory states should be arbitrary. In particular, it is an open question whether a controller with

infinitely many memory states can eliminate the singularity in the system Gramian, which otherwise causes unfavorable performance scaling.

We also restricted the feedback laws in the vehicular formation case to exhibit reflection symmetry. The results in the consensus case were, however, derived without such a limitation on the dynamic feedback layer. We therefore conjecture that this assumption can be relaxed also for the vehicular formation system without affecting the results.

The effect of different control architectures was not considered in the present study. A possible alternative architecture is one in which each controller can affect the plants at neighboring nodes as well as the own plant. The the dynamic control law would then look like $u_k = (Dz)_k + (Fx)_k$ in the consensus case and $u_k = (Dz)_k + (Fx)_k + (Gv)_k$ in the vehicular formation case, where D is any feedback operator. Preliminary evaluations show that this does not affect our main result. Since this model, while being theoretically intriguing, may not be meaningful in a realistic control system, we have limited the scope here to the control architecture depicted in Figure 3.1. In Chapter 6, we also discuss a centralized control architecture in the context of frequency control in power networks.

3.6   Concluding summary of Chapter 3

We have treated consensus and vehicular formation control problems modeled over regular lattice structures. We evaluated performance in terms of notions of coherence, quantified through the variance of nodal state fluctuations, for which we studied asymptotic scalings with respect to the network size. As the main contribution of this chapter, we addressed the question of whether a dynamic feedback law can improve performance compared to static feedback.

We developed a novel technical framework to evaluate the systems and their asymptotic performance scalings based on general Fourier analysis. We exploited the locality property of the feedback operators to redefine them on an infinite toric lattice, which allowed us to regard the system's discrete Fourier symbols as subsamples of a Z-transform. The $\mathcal{H}_2$ norms used to evaluate input-output performance, which are calculated using sums involving Fourier symbols, could then be approximated through corresponding integrals over functions of the Z-transform. The asymptotic performance scalings were then derived using simple properties of such integrals.

We found that it is not possible to design a dynamic feedback law based on *relative* state measurements that improves performance compared to static feedback. With relative feedback, connections in 3 spatial dimensions are instead needed to achieve full coherence in the consensus case, while 5 dimensions are needed in the vehicular formation case. If the controller, however, can access some *absolute* state measurements, dynamic feedback can improve asymptotic performance scalings compared to static feedback, provided the absolute state measurements are noiseless. This implies that a 1-dimensional vehicular formation using a dy-

namic feedback protocol could in theory become fully coherent. Since noiseless measurements are, however, never available in practice, our results show that the fundamental limitation to feedback based on local, relative measurements that were found in [7] remain valid with dynamic feedback.

Appendix to Chapter 3

Proof of Lemma 3.2

Given that $\hat{\mathcal{A}}_\infty(\theta)$ is Hurwitz, possibly except the unobservable mode $\hat{\mathcal{A}}_\infty(0)$, the integrand $\hat{x}^{\mathrm{tr}}(\theta) \, [-\pi, \pi]^d \mapsto \mathbb{R}$ is continuous and bounded over the compact domain given by the punctured multivariable rectangle. The function $\hat{x}^{\mathrm{tr}}(\theta)$ is therefore Riemann integrable on that domain. In particular, it is Riemann integrable on the domain $\delta \leq |\theta_i| \leq \pi$ for $i = 1, \ldots, d$ and any fixed $\delta > 0$.

In the interval $\Delta < |\theta_i| < \delta$, allowing for $\Delta \to 0$ the integrand will instead be monotonic. For simplicity, we show this through the scalar case in which $\hat{\mathcal{A}}_\infty(\theta) = \hat{a}_\infty(\theta) = \sum_{k \in \mathbb{Z}^d} a_k e^{-j\theta \cdot k}$, which we know to be negative outside $\theta = 0$ for stability reasons. Solving the Lyapunov equation (3.30) then gives $\hat{X}(\theta) = \hat{x}^{\mathrm{tr}}(\theta) = \frac{-1}{2 \sum_{k \in \mathbb{Z}^d} a_k \cos(\theta \cdot k)}$ for $\theta \in [-\pi, \pi]^d \setminus \{0\}$. Its derivative in each coordinate direction $i = 1, \ldots, d$ is

$$\frac{\mathrm{d}\hat{x}^{\mathrm{tr}}(\theta)}{\mathrm{d}\theta_i} = \frac{-2 \sum_{k \in \mathbb{Z}^d} a_k k_i \sin(k_1 \theta_1 + \cdots k_d \theta_d)}{(2 \sum_{k \in \mathbb{Z}^d} a_k \cos(k_1 \theta_1 + \cdots k_d \theta_d))^2}.$$

By the locality asssumption (3.7), it satisfies $\frac{\mathrm{d}\hat{x}^{\mathrm{tr}}(\theta)}{\mathrm{d}\theta_i} < 0$ for $\theta_i \in (0, \delta)$ and $\frac{\mathrm{d}\hat{x}^{\mathrm{tr}}(\theta)}{\mathrm{d}\theta_i} > 0$ for $\theta_i \in (-\delta, 0)$ with $\delta \geq \pi/q$, since it holds

$$\mathrm{sgn}(\sin(kx)) = \mathrm{sgn}(x) \quad \text{for} |x| \leq \frac{\pi}{k}.$$

The integrand $\hat{x}^{\mathrm{tr}}(\theta)$ is thus monotonically decreasing away from zero for $|\theta_i| \leq \delta$, where δ can always be fixed.

A similar argument holds for when $\hat{\mathcal{A}}_\infty(\theta)$ is matrix-valued, in which case one considers matrix-valued coefficients of the Z-transform.

It is well-known that integrals of monotonic functions $f(x)$ can be estimated by upper and lower Riemann sums; $\int_m^{n+1} f(x)\mathrm{d}x \leq \sum_{k=m}^n f(k) \leq \int_{m-1}^n f(x)\mathrm{d}x$ if $f(x)$ decreasing (and the opposite if $f(x)$ increasing). We use this to bound the monotonic part of the sum in (3.28):

$$V_M^\delta = \frac{1}{N_\delta^d} \sum_{\substack{\theta = \frac{2\pi}{N} n \\ |n_i| < \frac{\delta N}{2\pi}}} \mathrm{tr}\left(\hat{\mathcal{B}}_\infty^*(\theta) \hat{X}(\theta) \hat{\mathcal{B}}_\infty(\theta)\right) \tag{3.59}$$

by the integral from Δ to δ:

$$I^\delta(\Delta) := \int_{\Delta \leq |\theta_1| \leq \delta} \cdots \int_{\Delta \leq |\theta_d| \leq \delta} \hat{x}^{\mathrm{tr}}(\theta)\mathrm{d}\theta_1 \cdots \mathrm{d}\theta_d \tag{3.60}$$

as

$$I^\delta\left(\frac{4\pi}{N}\right) \leq V_M^\delta \leq I^\delta\left(\frac{2\pi}{N}\right), \tag{3.61}$$

since $2\pi/N$ and $4\pi/N$ are the first two wavenumbers (or sampling points in the sum). Here, N_δ is the number of summands for which $|n_i| < \frac{\delta N}{2\pi}$. For the remainder of the sum, we use the Riemann integrability away from zero. That is, let

$$V_M^\pi = \frac{1}{(N - N_\delta)^d} \sum_{\substack{\theta = \frac{2\pi}{N} n \\ |n_i| \geq \frac{\delta N}{2\pi}}} \text{tr} \left(\hat{\mathcal{B}}_\infty^*(\theta) \hat{X}(\theta) \hat{\mathcal{B}}_\infty(\theta) \right)$$

and note that $\lim_{N \to \infty} V_N^\pi = I^\pi$, where $I^\pi := \int_{\delta \leq |\theta_1| \leq \pi} \cdots \int_{\delta \leq |\theta_d| \leq \pi} \hat{x}^{\text{tr}}(\theta) \mathrm{d}\theta_1 \cdots \mathrm{d}\theta_d$. Therefore, at some $\bar{N}$, we will have that $|V_{\bar{N}}^\pi - I^\pi| < I^\delta(\frac{2\pi}{N}) - I^\delta(\frac{4\pi}{N})$, so that

$$I^\delta(\frac{4\pi}{N}) + I^\pi \leq V_M^\delta + V_M^\pi \leq I^\delta(\frac{2\pi}{N}) + I^\pi,$$

for all $N > \bar{N}$, which is precisely equivalent to the statement of Lemma 3.2.

∎

Proof of Theorem 3.6

Each block matrix $\hat{\mathcal{A}}_\infty(\theta) = \begin{bmatrix} \hat{a}_\infty(\theta) & \hat{b}_\infty(\theta) \\ 1 & \hat{f}_\infty(\theta) \end{bmatrix}$ has eigenvalues

$$\lambda_{1,2} = \frac{\hat{f} + \hat{a}}{2} \pm \sqrt{\left(\frac{\hat{f} - \hat{a}}{2} \right)^2 + \hat{b}}, \tag{3.62}$$

where we omit the ∞−subscript and the argument θ of the individual Fourier symbols for notational compactness. The system is input-output stable if and only if $\text{Re}\{\lambda_{1,2}(\theta)\} < 0$ for every $\theta \neq 0$. To find necessary conditions for stability, it suffices that we study this condition along one of the coordinate directions, so we let $\theta = (\theta_1, 0, \ldots, 0)$.

A necessary condition for stability becomes:

$$\left| \text{Re} \left\{ \frac{\hat{f} + \hat{a}}{2} \right\} \right| > \left| \text{Re} \left\{ \sqrt{\left(\frac{\hat{f} - \hat{a}}{2} \right)^2 + \hat{b}} \right\} \right|. \tag{3.63}$$

If $\hat{a}, \hat{b}, \hat{f}$ are real, (3.63) holds as long as $\hat{b} < \hat{a}\hat{f}$, which is true if $\hat{b}, \hat{a}, \hat{f} < 0$.

If $\hat{a}, \hat{b}, \hat{f}$ are not all real, the number under the square root on the right hand side of (3.63) will be complex-valued. Recall that for any complex number $z = |z|e^{j\phi}$, $\arg\{z^{1/2}\} = \frac{1}{2}\arg\{z\}$. Therefore, in particular, if the argument is near $\pm\pi/2$, then $\text{Re}\{\sqrt{z}\} = \sqrt{|z|}\cos(\phi/2)$ can become large compared to $\text{Re}\{z\} = |z|\cos(\phi)$. In our case, this means that in order to satisfy (3.63), the imaginary part of the number under the square root cannot become too large compared to the real part.

Consider therefore the standard Maclaurin expansions of the Z-transforms $\hat{a}, \hat{b}, \hat{f}$ along $\theta = (\theta_1, 0, \ldots, 0)$. To derive necessary conditions for stability, it suffices to consider the first approximations of the Z-transforms near $\theta = 0$, which are $\hat{a}_\infty(\theta) \approx \hat{a}_0 + j\hat{a}_1\theta_1 + \hat{a}_2\theta_1^2$, $\hat{b}_\infty(\theta) \approx j\hat{b}_1\theta_1 + \hat{b}_2\theta_1^2$, and $\hat{f}_\infty(\theta) \approx j\hat{f}_1\theta_1 + \hat{f}_2\theta_1^2$ ($\hat{b}_0 = \hat{f}_0 = 0$ due to Assumption 3.3). Note that the coefficients $\hat{a}_0, \hat{a}_1$ and $\hat{b}_1$ can be zero if the corresponding operator is symmetric and/or lacks absolute feedback, but $\hat{b}_2, \hat{f}_2$ must be nonzero for a meaningful feedback design.

Expanding the radicand on the RHS of (3.63) with these Maclaurin expansions gives

$$
R =: \left(\frac{\hat{f} - \hat{a}}{2} \right)^2 + \hat{b} \approx
$$
$$
\frac{\hat{a}_0^2}{4} + \frac{(\hat{a}_2 - \hat{f}_2)^2}{4}\theta_1^4 + \left(\hat{b}_2 - \frac{(\hat{a}_1 - \hat{f}_1)^2}{4} + \frac{\hat{a}_0(\hat{a}_2 - \hat{f}_2)}{2} \right)\theta_1^2
$$
$$
+ j\left[\frac{(\hat{a}_1 - \hat{f}_1)(\hat{a}_2 - \hat{f}_2)}{2}\theta_1^3 + \left(\hat{b}_1 + \frac{\hat{a}_0(\hat{a}_1 - \hat{f}_1)}{2} \right)\theta_1 \right]. \quad (3.64)
$$

Now, note that if $\hat{b}_1 \neq 0$, then the imaginary part of R, $\text{Im}\{R\}$, can grow linearly in θ_1 near zero. Unless $\hat{a}_0 \neq 0$, the real part, on the other hand, will grow quadratically in θ_1, causing $\text{Im}\{R\}$ to become arbitrarily many times larger than $\text{Re}\{R\}$ as $\theta_1 \to 0$. This puts $\arg\{R\}$ near $\pm\pi/2$ and $\text{Re}\{\sqrt{R}\}$ can become arbitrarily many times larger than $\text{Re}\{R\}$. The LHS of (3.63) also grows quadratically in θ_1 unless $\hat{a}_0 \neq 0$:

$$
\left| \text{Re}\left\{ \frac{\hat{f} + \hat{a}}{2} \right\} \right| \approx \left| \frac{\hat{a}_0}{2} + \frac{\hat{a}_2 + \hat{f}_2}{2}\theta_1^2 \right|,
$$

and will therefore also be smaller than $\text{Re}\{\sqrt{R}\}$ near $\theta_1 = 0$. We conclude that (3.63) cannot be fulfilled in the case where $\hat{b}_1 \neq 0$, $\hat{a}_0 = 0$.

Necessary conditions for input-output-stability are therefore that $\hat{b}_1 = 0$, i.e., $\hat{b}$ real (B symmetric), or that $\hat{a}_0 \neq 0$ (absolute feedback in A).

■

Proof of Theorems 3.7 and 3.8

The characteristic polynomial of the matrix $\hat{\mathcal{A}}_\infty(\theta)$ is

$$
p(\lambda, \theta) = \lambda^3 - (\hat{a} + \hat{g})\lambda^2 + (\hat{a}\hat{g} - \hat{f} - \hat{c})\lambda + \hat{a}\hat{f} - \hat{b}, \quad (3.65)
$$

where we have again omitted the ∞−subscript and the argument θ of the Fourier symbols. As in the previous proof, we study stability along the coordinate θ_1, while letting $\theta_2, \cdots, \theta_d = 0$. Recall that all Fourier symbols are now real-valued by Assumption 3.5. We can therefore use the Routh-Hurwitz stability criteria which state that; given a characteristic polynomial $p(\lambda) = m_3\lambda^3 + m_2\lambda^2 + m_1\lambda + m_0$, then necessary and sufficient criteria for stability are that

(i) $m_i > 0$, $i = 0, 1, 2, 3$,

(ii) $m_2 m_1 > m_3 m_0$.

In the case of (3.65), a necessary condition for fulfilling (i) is that we do *not* have $\hat{a} = 0$, $\hat{b} = 0$ simultaneously. The condition (i) can otherwise easily be fulfilled, e.g., by ensuring $\hat{a}, \hat{b}, \hat{c}, \hat{f}, \hat{g} < 0$. Assuming (i) is fulfilled, consider (ii), which says that:

$$-(\hat{a} + \hat{g})(\hat{a}\hat{g} - \hat{f} - \hat{c}) > \hat{a}\hat{f} - \hat{b}. \tag{3.66}$$

First, we note that if $\hat{b} = 0$, then (3.66) reduces to $-\hat{a}^2\hat{g} - \hat{a}\hat{g}^2 + \hat{a}\hat{c} + \hat{g}\hat{f} + \hat{g}\hat{c}$, which is also automatically fulfilled if $\hat{a}, \hat{b}, \hat{c}, \hat{f}, \hat{g} < 0$.

For the case where $\hat{b} \neq 0$, we follow the approach in the previous proof and substitute the Maclaurin expansions of the Fourier symbols into (3.66). That is, we set $\hat{a}_\infty(\theta) \approx \hat{a}_0 + \hat{a}_2\theta_1^2$ and analogously for $\hat{b}$, $\hat{c}$, $\hat{f}$, $\hat{g}$. Note that the absolute term is only nonzero if absolute feedback is present. To a first approximation near $\theta_1 = 0$ (3.66) then becomes:

$$-(\hat{a}_0 + \hat{g}_0 + (\hat{a}_2 + \hat{g}_2)\theta_1^2)(\hat{a}_0\hat{g}_0 - \hat{f}_0 - \hat{c}_0 + (\hat{a}_0\hat{g}_2 + \hat{a}_2\hat{g}_0 - \hat{f}_2 - \hat{c}_2)\theta_1^2 + \hat{a}_2\hat{g}_2\theta_1^4)$$
$$> -\hat{b}_0 - \hat{b}_2\theta_1^2 + \hat{a}_0\hat{f}_0 + (\hat{a}_0\hat{f}_2 + \hat{a}_2\hat{f}_0)\theta_1^2 + \hat{a}_2\hat{f}_2\theta_1^4 \quad (3.67)$$

By condition (i), both sides of the inequality are positive. Now, if the RHS scales in lower powers of θ_1 than the LHS, then near $\theta_1 = 0$ it becomes arbitrarily many times larger than the LHS, and (3.67) cannot be fulfilled. In particular, if $\hat{b}_0 = 0$, but $\hat{b}_2 \neq 0$, then the RHS scales as θ_1^2, and it must hold that at least one of $\hat{a}_0, \hat{c}_0, \hat{f}_0, \hat{g}_0$ is nonzero for the LHS to have the same scaling. If only relative feedback from the states x and v is available, then it is only possible to set $\hat{a}_0 < 0$, which is then also necessary. This concludes the proof of Theorem 3.7.

If $\hat{b}_0 \neq 0$ (absolute position feedback in B), we must by (3.67) require that $\hat{g}_0$ and at least one of $\hat{f}_0$, $\hat{c}_0$ or $\hat{a}_0$ are nonzero, alternatively $\hat{a}_0$ and $\hat{c}_0$ nonzero. In either case, this requires access to absolute velocity feedback, in G and/or C. This concludes the proof of Theorem 3.8.

∎

Proof of Lemma 3.9

To prove Lemma 3.9 we treat the two feasible feedback configurations given by Theorem 3.6 separately.

Case a) B symmetric

If $\hat{b}_\infty(\theta)$ is real, then

$$\varphi^c(\hat{a}, \hat{f}, \hat{b}) = \frac{\hat{b}\mathrm{Re}\{\hat{a}\}(\mathrm{Re}\{\hat{a}\} + \hat{f})}{\hat{b}\hat{f} + \mathrm{Re}\{\hat{a}\}(\hat{b} - \mathrm{Im}\{\hat{a}\}^2 - (\mathrm{Re}\{\hat{a}\} + \hat{f})^2)}, \tag{3.68}$$

where we have again omitted the ∞-subscript and the argument of the individual Fourier symbols. We notice immediately, that if $\hat{a} \equiv 0$, i.e., if $A = 0$, then $\varphi^c(\hat{a}, \hat{f}, \hat{b}) \equiv 0$, and $\hat{f} + \varphi^c(\hat{a}, \hat{f}, \hat{b})$ scales just as $\hat{f}$.

For the case $\hat{a} \neq 0$, recall that the notation $u(\theta) \sim v(\theta)$ implies $\underline{c}v(\theta) \leq u(\theta) \leq \bar{c}v(\theta)$, where $\underline{c}, \bar{c}$ are positive constants. For a product and/or sum of two such functions, it simply holds $u_1(\theta)u_2(\theta) + u_3(\theta) \sim v_1(\theta)v_2(\theta) + v_3(\theta)$, which means that the bounds are $\underline{c}_1\underline{c}_2 v_1(\theta)v_2(\theta) + \underline{c}v_3 \leq u(\theta) \leq \bar{c}_2 v_2(\theta)\bar{c}_2 v_2(\theta) + \bar{c}v_3(\theta)$. For a quotient: $u_1(\theta)/u_2(\theta) \sim v_1(\theta)/v_2(\theta)$ implies $(\underline{c}_1/\bar{c}_2)v_1(\theta)/v_2(\theta) \leq u_1(\theta)/u_2(\theta) \leq (\bar{c}_1/\underline{c}_2)v_1(\theta)/v_2(\theta)$. To determine the scaling of the function $\varphi^c(\hat{a}, \hat{f}, \hat{b})$, we can therefore derive the scalings of its individual terms, and simply substitute in (3.68).

We already established in (3.46) that $\hat{f} \sim -\beta(\theta_1^2 + \ldots + \theta_d^2)$, for some $\beta \leq ||f||_\infty$, and we will write $\hat{f} \sim -\beta\theta^2$ for short. Under the given assumptions, B has the same structure as F, so also $\hat{b} \sim -\beta\theta^2$. For A on the other hand, we do not impose Assumption 3.3 of relative measurements. Therefore, in general, the condition (3.8) is not fulfilled and $\sum_{k \in \mathbb{Z}_N^d} a_k := \hat{a}_0$, where $\hat{a}_0 \leq 0$ to guarantee stability. By (3.40), we then have that $\text{Re}\{\hat{a}\} = \hat{a}_0 - \sum_{k \in \mathbb{Z}^d} a_k(1 - \cos(\theta \cdot k))$. Since the term $\sum_{k \in \mathbb{Z}^d} a_k(1 - \cos(\theta \cdot k))$ has the same structure as $\hat{f}$, and we can write $\text{Re}(\hat{a}) \sim \hat{a}_0 + \beta\theta^2$.

If A is asymmetric, the imaginary part of the Z-transform (2.15) is $\text{Im}\{\hat{a}\} = -\sum_{k \in \mathbb{Z}^d} a_k \sin(\theta \cdot k)$. Making use of the inequality (3.42), its square can be upper bounded as

$$\text{Im}\{\hat{a}\}^2 \leq (2(2q)^d + 1) \sum_{k \in \mathbb{Z}^d} a_k^2 \sin^2(\theta \cdot k)$$

$$= ((2q)^d + \frac{1}{2}) \sum_{k \in \mathbb{Z}^d} a_k^2 \left(1 - \cos(2\theta \cdot k)\right) \qquad (3.69)$$

$$\leq ((2q)^d + \frac{1}{2})(2q)^{(d+2)}||a||_\infty^2(\theta_1^2 + \cdots + \theta_d^2),$$

where the last inequality is derived in analogy with (3.41). We can thus write $\text{Im}\{\hat{a}\}^2 \leq \bar{c}_a\beta\theta^2$ with $\bar{c} \geq 0$ for short. It is also evident that $\text{Im}\{\hat{a}\}^2 \geq 0$.

Now, consider the terms $\hat{b} - (\text{Im}\{\hat{a}\})^2$ in the denominator of (3.68). We already established $\hat{b} \sim -\beta\theta^2$, which implies $-\underline{c}\beta\theta^2 \leq \hat{b} \leq -\bar{c}\beta\theta^2$ for some positive constants $\underline{c}, \bar{c}$. Therefore, it also holds $-\underline{c}\beta\theta^2 - c_a\beta\theta^2 \leq \hat{b} - \text{Im}\{\hat{a}\}^2 \leq -\bar{c}\beta\theta^2$, i.e., $\hat{b} - \text{Im}\{\hat{a}\}^2 \sim -\beta\theta^2$.

We now insert $\hat{f}, \hat{b} \sim -\beta\theta^2$, $\text{Re}\{\hat{a}\} \sim \hat{a}_0 - \beta\theta^2$, $\hat{b} - (\text{Im}\{\hat{a}\})^2 \sim -\beta\theta^2$ into (3.68), which gives

$$\varphi^c(\hat{a}, \hat{f}, \hat{b}) \sim \beta\theta^2 \frac{-2\beta\theta^2 + 2\hat{a}_0}{2\beta^2\theta^4 + \beta(1 - 3\hat{a}_0)\theta^2 + \hat{a}_0^2}.$$

This can be written as $\varphi^c(\hat{a}, \hat{f}, \hat{b}) \sim -\tilde{\varphi}\beta\theta^2$, and it is easy to see that $\tilde{\varphi}$ will be a bounded, positive constant for any β and all $\theta \in [-\pi, \pi]^d$. In fact, $\tilde{\varphi} \leq 2$ if $\hat{a}_0 = 0$, or $\tilde{\varphi} \leq \frac{2}{|\hat{a}_0|}$ if $\hat{a}_0 < 0$.

Therefore, $\hat{f} + \varphi^c(\hat{a}, \hat{f}, \hat{b}) \sim -\beta\theta^2 - \tilde{c}\beta\theta^2 \sim -\beta\theta^2$, which is precisely (3.48).

∎

Case b) B asymmetric

If B is not chosen to be symmetric, we must by Theorem 3.6 require A to have a sufficient amount of absolute (negative) feedback, so that $\hat{a}_0 < 0$. Since the Fourier symbol of A is then bounded by some scalar multiple of $\hat{a}_0$, it is not restrictive to assume $\hat{a}_\infty(\theta) = a_o$ for some $a_o < 0$ from the beginning. We obtain:

$$\varphi^c(\hat{a}, \hat{f}, \hat{b}) = \frac{a_o \mathrm{Re}\{\hat{b}\}(a_o + \hat{f}) + \mathrm{Im}\{\hat{b}\}^2}{a_o(\mathrm{Re}\{\hat{b}\} - (a_o + \hat{f})^2) + \hat{f}\mathrm{Re}\{\hat{b}\}}. \tag{3.70}$$

In analogy to the discussion above, we have that $\hat{f} \sim -\beta\theta^2$ and $\mathrm{Re}\{\hat{b}\} \sim -\beta\theta^2$. We can treat $\mathrm{Im}\{\hat{b}\}^2$ in the same way as in (3.69) and derive $0 \leq \mathrm{Im}\{\hat{b}\}^2 \leq \bar{c}_b\beta\theta^2$. Now, regard the term $a_o^2\mathrm{Re}\{\hat{b}\} + \mathrm{Im}\{\hat{b}\}^2$, for which it will hold that $-a_o^2\underline{c}\beta\theta^2 \leq a_o^2\mathrm{Re}\{\hat{b}\} + \mathrm{Im}\{\hat{b}\}^2 \leq -a_o^2\underline{c}\beta\theta^2 + \bar{c}_b\beta\theta^2$. Therefore, provided that $a_o^2\bar{c} \geq \bar{c}_b \geq 1$ (which signifies that the amount of absolute feedback in A is sufficient to ensure stability), we have $a_o^2\mathrm{Re}\{\hat{b}\} + \mathrm{Im}\{\hat{b}\}^2 \sim -a_o^2\beta\theta^2$.

Inserting in (3.70) gives

$$\varphi^c(\hat{a}, \hat{f}, \hat{b}) \sim \beta\theta^2 \frac{a_o^2 + a_o}{\beta^2(a_o - 1)\theta^4 + \beta a_o(-2a_o + 1)\theta^2 + a_o^3} = -\tilde{\varphi}\beta\theta^2$$

Here, $\tilde{\varphi}$ is a positive constant, which for any β and all $\theta \in [-\pi, \pi]^d$ satisfies $\tilde{c} \leq \frac{1}{|a_o|}$. We can again conclude that $\hat{f} + \varphi^c(\hat{a}, \hat{f}, \hat{b}) \sim -\beta\theta^2$.

∎

Proof of Lemma 3.10

The function φ^v in (3.50) is

$$\varphi^v(\hat{a}, \hat{b}, \hat{c}, \hat{f}, \hat{g}) = \frac{\hat{b}^2 + \hat{b}(\hat{a}\hat{c} + \hat{c}\hat{g} - \hat{a}\hat{f} - \hat{a}\hat{g}^2 - \hat{a}^2\hat{g}) - \hat{c}\hat{f}\hat{a}(\hat{a} + \hat{g})}{\hat{b} - \hat{a}\hat{f} + \hat{a}^2(\hat{a} + \hat{g})} \tag{3.71}$$

From the proof of Lemma 3.9, we have that $\hat{a} \sim \hat{a}_0 - \beta\theta^2$, $\hat{b}, \hat{c}, \hat{f}, \hat{g} \sim -\beta\theta^2$ (where $\theta^2 = (\theta_1^2 + \cdots \theta_d^2)$). For stability purposes, we require $\hat{a}_0 \leq 0$.

We consider the two cases given by Theorem 3.7 separately.

Case a) $B = 0$

Substituting the scalings of the individual Fourier symbols into (3.71) gives:

$$\varphi^v(\hat{a}, \hat{b}, \hat{c}, \hat{f}, \hat{g}) \sim \beta^2 \theta^4 \frac{2\beta\theta^2 - \hat{a}_0}{2\beta^2\theta^4 + \beta(1 - 3\hat{a}_0)\theta^2 + \hat{a}_0^2} = \tilde{\varphi}\beta^2\theta^4.$$

For any β and for all $\theta \in [-\pi, \pi]^d$, we identify $\tilde{\varphi}$ as a positive constant, with $\tilde{\varphi} \leq \frac{1}{|\hat{a}_0|}$ if $\hat{a}_0 \neq 0$, $\tilde{\varphi} \leq 2$ if $\hat{a}_0 = 0$. Therefore, $\hat{f}\hat{g} + \varphi^v(\hat{a}, \hat{b}, \hat{c}, \hat{f}, \hat{g}) \sim \beta^2\theta^4 + \tilde{\varphi}\beta^2\theta^4 \sim \beta^2\theta^4$, which is precisely (3.52).

Case b) $B \neq 0$

If the operator B is nonzero, by Theorem 3.7 A is required to have a sufficient amount of absolute (negative) feedback, so $\hat{a}_0 < 0$. We can then set $\hat{a} \sim \hat{a}_0 < 0$ and:

$$\varphi^v \sim \beta^2\theta^4 \frac{\beta(1 - 2\hat{a}_0)\theta^2 + 2\hat{a}_0^2 - 1}{\beta\hat{a}_0(\hat{a}_0 + 1)\theta^2 - \hat{a}_0^3} = \tilde{\varphi}\beta^2\theta^2.$$

Again, $\tilde{\varphi}$ can be identified as a bounded positive constant, so $\hat{f}\hat{g} + \varphi^v(\hat{a}, \hat{b}, \hat{c}, \hat{f}, \hat{g}) \sim \beta^2\theta^4$ also in this case (provided $\hat{a}_0 \geq 1$, which signifies that the amount of absolute feedback in A is sufficient to guarantee stability).

If we choose to set the operator $C = 0$, then

$$\varphi^v \sim \beta^2\theta^4 \frac{2\beta^2\theta^4 - \beta(3\hat{a}_0 + 1)\theta^2 + \hat{a}_0^2 + \hat{a}_0 - 1}{2\beta^3\theta^6 + \beta^2(1 - 5\hat{a}_0)\theta^4 + \beta(4\hat{a}_0^2 - \hat{a}_0 + 1)\theta^2 - \hat{a}_0^3},$$

and the same conclusion for the scaling holds as above. Notice that the case $C = 0$ is not a meaningful control design if $B = 0$, which is why it is not considered under case a).

$\blacksquare$

Proof of Lemma 3.11

The function φ^v in (3.50) is still given by (3.71). All Fourier symbols scale as in the previous proof, except $\hat{f}$, due to the absolute feedback term. Let us therefore write $\hat{f} \sim f_o$, in analogy with the proof of Lemma 3.9, case b). Recall that by Theorem 3.8, there can be no absolute feedback term in B, even though absolute position measurements are available.

It is possible to set either of A, B, C to zero (although, if $B = 0$, both C and A must be non-zero for the feedback law to be feasible). To be able to regard all these cases at once, we choose to write the scalings of the individual Fourier symbols as $\hat{a} \sim -\tilde{a}\theta^2$, (the case with an absolute feedback term in A is treated below), $\hat{b} \sim -\tilde{b}\theta^2$, $\hat{c} \sim -\tilde{c}\theta^2$, $\hat{f} \sim f_o$ and $\hat{g} \sim -\tilde{g}\theta^2$. Inserting in (3.50) gives

$$\varphi^v \sim \theta^2 \frac{\tilde{a}\tilde{b}\tilde{g}(\tilde{a} + \tilde{g})\theta^4 + \tilde{c}(\tilde{a} + \tilde{g})(\tilde{b} - \tilde{a}f_o)\theta^2 + \tilde{b}(\tilde{a}f_o - \tilde{b})}{\tilde{a}^2(\tilde{a} + \tilde{g})\theta^4 + \tilde{b} - \tilde{a}f_o}. \tag{3.72}$$

If $B = 0$, i.e., $\tilde{b} = 0$, then, by letting $\tilde{c}, \tilde{a}, \tilde{g} \sim \beta$, (3.72) becomes $\varphi^v \sim -2f_o\beta^2\theta^4\frac{1}{2\beta^2\theta^4+f_o}$. We know that $\hat{f}\hat{g} \sim -f_o\beta\theta^2$, and the sum of these functions scales as $\hat{f}\hat{g}+\varphi^v \sim \beta\theta^2$ (recall, $f_o < 0$).

If B is nonzero, we can write (3.72) as $\varphi^v \sim \tilde{\varphi}\beta\theta^2$. Then for any choice of A, C, $\tilde{\varphi}$ will be bounded, but it may be negative for some $\theta \in [-\pi, \pi]^d$. For example, if $A = C = 0$, then $\varphi^v = -\tilde{b}\theta^2$. However, for any feasible configuration, the system's $\mathcal{H}_2$ norm must be positive, requiring that $\hat{f}\hat{g} + \varphi^v > 0$. In particular, the absolute feedback term $|\hat{f}_0|$ that is necessary to ensure stability according to the proof of Theorem 3.8, must be sufficiently large. Since both $\hat{f}\hat{g}$ and φ^v scale as θ^2, we can then conclude that $\hat{f}\hat{g} + \varphi^v \sim \beta\theta^2$.

If A has an absolute feedback term, i.e., $\hat{a} \sim a_o$, then it suffices to inspect (3.50) to note that there will be a term like $a_o f_o (a_o \tilde{c} + \tilde{b})\theta^2$ in the numerator of φ^v, while in the denominator, there is a term a_o^3. Since we require that at least one of B or C is nonzero for a meaningful feedback law, this means that φ^v will always scale as $\beta\theta^2$ when A has absolute feedback. Thus, also in this case $\hat{f}\hat{g} + \varphi^v \sim \beta\theta^2$.

∎

Proof of Lemma 3.12

By rewriting the dynamics of the consensus algorithm in (3.6) with the control signal as the output;

$$\begin{bmatrix} \dot{z} \\ \dot{x} \end{bmatrix} = \begin{bmatrix} A & B \\ I & F \end{bmatrix} \begin{bmatrix} z \\ x \end{bmatrix} + \begin{bmatrix} 0 \\ I \end{bmatrix} w \tag{3.73}$$
$$u = z + Fx,$$

we can obtain the control signal variance (3.57) through the $\mathcal{H}_2$ norm from w to u, divided by the total network size N^d. We can use the DFT (2.14) to block-diagonalize the system, and solve a Lyapunov equation for each wavenumber n, as discussed in Section 2.1.2. In this case, we obtain that

$$\sum_{k \in \mathbb{Z}_N^d} \mathbb{E}\{u_k^* u_k\} = \sum_{n \in \mathbb{Z}_N^d \setminus \{0\}} \frac{\hat{b}_n - \hat{f}_n(\hat{f}_n + \hat{a}_n)}{2(\hat{a}_n + \hat{f}_n)},$$

which, if $M = N^d$, is equivalent to

$$M\mathbb{E}\{u_k^* u_k\} = \frac{1}{2}\left(||\hat{f}||_1 + ||\frac{\hat{b}}{\hat{a} + \hat{f}}||_1\right), \tag{3.74}$$

where the equivalence of the sum and the l_1-norm follows from the fact that we must have $\hat{f}_n, \hat{b}_n < 0$ and $\hat{f}_n + \hat{a}_n < 0$ for all n in order to guarantee stability (see Theorem 3.4). Now, if $\hat{f}$ is the Fourier transform of a function array f, then

$$||\hat{f}||_\infty \leq ||f||_1, \quad ||f||_\infty \leq \frac{1}{M}||\hat{f}||_1 \tag{3.75}$$

(see [7]). We can use this in (3.74) to obtain the first bound of the Lemma:

$$||f||_\infty \leq \frac{1}{M}||\hat{f}||_1 \leq 2\mathbb{E}\{u_k^* u_k\}. \tag{3.76}$$

It also holds that

$$2M\mathbb{E}\{u_k^* u_k\} \geq ||\frac{\hat{b}}{\hat{a} + \hat{f}}||_1 \geq \frac{||\hat{b}||_1}{||\hat{a} + \hat{f}||_\infty} \geq \frac{||\hat{b}||_1}{||\hat{a}||_\infty + ||\hat{f}||_\infty},$$

where the last equality follows from the triangle inequality. Now, we can use the fact that $||\hat{a}||_\infty \leq ||\hat{a}||_1 \leq (2q)^d||a||_\infty$ (due to the locality assumption) and substitute the bound (3.76) to get:

$$2M\mathbb{E}\{u_k^* u_k\} \geq \frac{||\hat{b}||_1}{(2q)^d(||a||_\infty + 2\mathbb{E}\{u_k^* u_k\})}.$$

Now, we use that $||b||_\infty \leq \frac{1}{M}||\hat{b}||_1$ to rewrite this as:

$$4(2q)^d(\mathbb{E}\{u_k^* u_k\})^2 + 2(2q)^d||a||_\infty \mathbb{E}\{u_k^* u_k\} - ||b||_\infty \geq 0, \tag{3.77}$$

which leads to the second bound of the Lemma.

∎

Chapter 4

The price of synchrony: resistive losses in synchronizing power networks

We now turn to a differrent type of networked dynamical system and study the problem of synchronization in power networks. We model a synchronous generator network as a system of coupled oscillators, as in Example 1.3, and evaluate performance in terms of the resistive losses that are incurred in keeping this network in a synchronous state. These losses, which we refer to as transient losses, are in addition to the static losses associated with steady state flows in the power network. They arise due to the transient power flow flucuations that occur when the system is perturbed from a synchronous state by a small transient event, or in the face of small stochastic disturbances. We term this performance measure the "price of synchrony", as it reflects the cost, in terms of real power losses, associated with lack of synchrony.

In this chapter, we show how the total network's transient power losses can be quantified using the $\mathcal{H}_2$ norm of a linear system of coupled swing equations with an appropriately defined performance output that accounts for local phase deviations, of the type (1.11). We show that the total transient losses will scale unboundedly with the network's size. Furthermore, they are shown to be only weakly dependent on network topology, and it is therefore no longer true, as in Chapter 3, that increasing network connectivity improves performance.

These limitations imply that even though the power losses that arise during synchronization are typically a small percentage of the total real power flow, our results (based on a simplified network model) indicate that these losses may become significant as power networks evolve toward increasingly distributed systems. Furthermore, merely adding links to the network to increase connectivity is unlikely to alleviate the increases in transient power losses as the network grows. In this chapter, we illustrate these findings through a number of numerical examples.

The remainder of this chapter is organized as follows. We begin in Section 4.1 with a short survey of some related work on synchronous stability in power net-

works. We then derive the system model in Section 4.2 and introduce the performance measure (the "price of synchrony") in Section 4.3. Section 4.4 derives algebraic expressions for the $\mathcal{H}_2$ norms and provides the main results. A discussion of generalizations and bounds on the $\mathcal{H}_2$ norm is provided in Section 4.5. Section 4.6 contains some numerical examples to illustrate the theory. We summarize in Section 4.7.

4.1   The problem of frequency synchronization

The electric power network is a highly complex networked dynamical system. It is constantly exposed to disturbances on different scales due to, for example, line failures, load fluctuations and generator rampings. Stability, by which we mean the system's ability to regain a state of operating equilibrium after a disturbance, is therefore a prerequisite for a secure operation of the power network. Lack of stability may lead to blackouts, like the one in southern Sweden in 1983 when 2/3 of the country's network was shut down [43], or the major Northeastern blackout of 2003 which affected 50 million people in the United States and Canada [31]. Although power system stability is essentially a single problem, one typically regards it as three different issues related to, respectively, generation-load balance, voltage stability, and rotor-angular or synchronous stability [56]. Synchronous stability, which is what we consider in this thesis, is the ability of the power grid to recover synchrony after a physical disturbance [56].

Synchrony, in this context, refers to the alignment of the phase and frequency of all generators within a particular power network. In other words, it is when all of the frequencies are equal [53] and the phase differences are at an equilibrium state corresponding to balanced power flows throughout the network. Such a state is reflected by the mechanical analogy in Figure 1.3. Maintaining synchrony thus depends on a network's ability to sustain or restore this condition when it is subjected to disturbances from its nominal operating point.

Synchronous stability properties of power systems are typically studied using a so-called network reduced, or *Kron reduced*, model. This means that loads are modeled as impedances that are absorbed into the "lines" of the reduced network, see for example [57, 83, 14, 53, 21] and the references therein. The resulting system is a set of coupled swing equations that describe the dynamics of a network of generators connected by these lines, as in Example 1.3. This system is then analyzed to determine conditions under which the synchronized state is stable, see for example [53, 22]. These analyses are related to the well-studied transient stability problem [13], which refers to the ability of a system to return to a stable operating condition after a large disturbance.

A recent research trend has been to analyze synchronous stability properties in power systems using tools from systems and control theory. The associated literature is vast and we only highlight a subset of the research. For example, a series of works draws connections between power grids and coupled Kuramoto oscilla-

tors [18, 19, 20, 22]. This modeling framework provides a first-order approximation of the system and Dörfler and Bullo [19, 20] exploit properties of this well-studied problem to provide analytical conditions for frequency synchronization. In a related work [17] these authors also make connections between network reduced models and the structure preserving network model of Bergen and Hill [10], which we will look more into in Chapter 5. Models similar to Kuramoto oscillators have also been used in [49] to investigate the effects of power flow scheduling and increased network connectivity on the rate of convergence.

Control design for synchronizing oscillator networks has been investigated in [29, 23], where synchronization is defined in terms of voltage differences between connected nodes rather than phase angle differences. These authors employ an $\mathcal{H}_2$ system norm as a performance metric for control design. Here, we also evaluate system performance using an $\mathcal{H}_2$ norm based metric. However, since both the system dynamics and the output are defined differently, these are two distinct performance metrics.

The problem that we formulate in this chapter is new in the context of synchronization of power networks. We assume that the synchronous stability conditions are fulfilled and thus that the system will return to a synchronized state after being subjected to small disturbances. We then focus, as already mentioned, on performance in terms of the power losses associated with maintaining this syncronous state. This method for performance evaluation in power networks was originally proposed in [6]. A similar performance measure was used by the authors of [69] to characterize a notion of transient energy in oscillator networks and in [36] it is used to quantify amounts of interaction between generators. Recently, the similarity of this performance measure and the notion of network coherence in Chapter 3 has also been exploited in [63], where it is proposed as an optimization criterion for inertia allocation in networks. In this chapter, we develop analytic expressions for this performance measure under some simplifying assumptions, and discuss ways in which they can be regarded as fundamental limitations to performance in synchronizing power networks.

4.2 Formulation of coupled oscillator dynamics

4.2.1 Network model and swing equation

Consider a network $\mathcal{G} = \{\mathcal{V}, \mathcal{E}\}$, where $|\mathcal{V}| = N$ is the total number of nodes, or buses. $\mathcal{E} = \{e_{i,j}\}$ represents the set of edges, or network lines. Throughout this chapter, we will assume a Kron-reduced network model (see, for example, [58, 13, 21, 54]) where the reduction procedure eliminates the constant-impedance loads and absorbs their effects into the network lines $\mathcal{E}$, along with any phase-shifting transformers (this assumption will be relaxed in Chapter 5). Thus, at every node $i \in \mathcal{V}$, there is a generator with inertia constant m_i, damping coefficient d_i, voltage magnitude V_i and voltage phase angle θ_i. Such a network is depicted in Figure 4.1 for a system where $N = 7$. In the absence of any external control input,
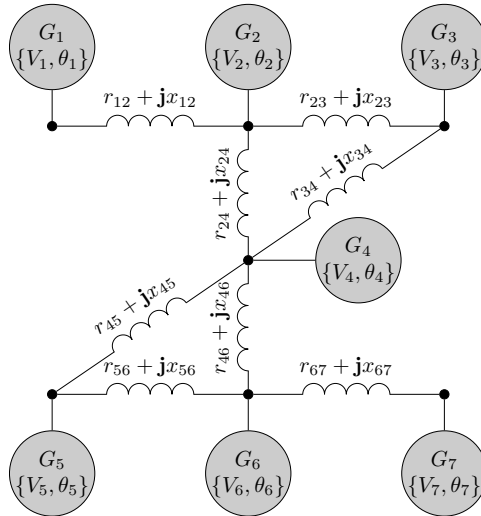
Figure 4.1: An example of a network of $N = 7$ generator nodes.

the dynamics of the ith generator can be described using the following classical machine model [57]:

$$m_i \ddot{\theta}_i + d_i \dot{\theta}_i = P_{m,i} - P_{e,i} \tag{4.1}$$

where $P_{m,i}$ is the mechanical power input from the turbine and $P_{e,i}$ is the real power injected into the grid at node i, for which we will shortly provide an expression.

The swing equation (4.1) describes the physical acceleration or deceleration that arises in a synchronous generator as soon as there is a power imbalance, and which, provided the network is stable, will allow the network to resynchronize. This control is *spontaneous*, as argued in, for example, [53]. Yet, we regard the swing equation as a type of control actuation in accordance with our main problem formulation in (1.8). The spontaneous control is different from a typical control input, like the ones we considered in Chapter 3, in that the controller parameters cannot be tuned freely since they are physical properties. Later in this thesis, in the context of control of power inverters, we will consider control dynamics that are designed to emulate the swing equation (4.1), but where parameters can more readily be tuned.

4.2.2   The power flow equation

The real electric power flow injected to the grid at each node $i \in \mathcal{V}$ is given by

$$P_{e,i} \;=\; \bar{g}_i V_i^2 + \sum_{j \in \mathcal{N}_i} g_{ij} V_i V_j \cos(\theta_i - \theta_j) + \sum_{j \in \mathcal{N}_i} b_{ij} V_i V_j \sin(\theta_i - \theta_j), \tag{4.2}$$

where $\mathcal{N}_i$ denotes the neighbor set of node i in the Kron-reduced network $\mathcal{G}$. The parameters g_{ij} and b_{ij} are respectively the conductance and susceptance associated

with the line e_{ij} and $\bar{g}_i$ is the shunt conductance of node i (see Section 2.3.2 for their computation). As per convention in power flow analysis, we assume that all quantities in (4.2) have been normalized by system constants and are measured in per unit (p.u.).

In what follows, we will use a simplified, linear model in which we consider small deviations from a stable operating point $\begin{bmatrix} \theta^{\mathrm{ss}}, & \omega^{\mathrm{ss}} \end{bmatrix}^T$, which, without loss of generality we can transfer to the origin through a change of variables. This linearization allows us to investigate the effects of small disturbances or persistent small amplitude noise within a neighborhood of the operating point. The standard linear power flow assumptions include assuming constant voltage amplitudes, $V_i = 1$ p.u. for all $i \in \mathcal{V}$ and retaining only the linear terms in (4.2), which leads to

$$P_{e,i} \approx \sum_{j \in \mathcal{N}} b_{ij} \left[\theta_i - \theta_j \right]. \tag{4.3}$$

See for example [42] for a detailed analysis of the applicability of such assumptions. Having transfered the operating point to the origin, we may let deviations in the constant $P_{m,i}$ in (4.1) be absorbed into the disturbance input w_i, which characterizes, for example, fluctuations in generation and loads. Substituting (4.3) into (4.1) then gives

$$m_i \ddot{\theta}_i + d_i \dot{\theta}_i \approx - \sum_{j \in \mathcal{N}_i} b_{ij} \left[\theta_i - \theta_j \right] + w_i. \tag{4.4}$$

Now, we can use the system's suseptance matrix L_B from (2.19) to rewrite this in state space form as follows.

$$\frac{\mathrm{d}}{\mathrm{d}t} \begin{bmatrix} \theta \\ \omega \end{bmatrix} = \begin{bmatrix} 0 & I \\ -M^{-1} L_B & -M^{-1} D \end{bmatrix} \begin{bmatrix} \theta \\ \omega \end{bmatrix} + \begin{bmatrix} 0 \\ M^{-1} \end{bmatrix} w, \tag{4.5}$$

where $M = \mathrm{diag}\{m_i\}$, $D = \mathrm{diag}\{d_i\}$.

4.3 Performance measure

As mentioned in the introduction to this chapter, our concern is not to characterize the stability of the system (4.5) but rather to evaluate its performance in terms of losses associated with transient power flows. We therefore assume that the system matrices are such that the dynamics are stable around the equilibrium manifold for which all phases are equal. We now define the system output, or performance measure, that will be used throuhout this thesis to evaluate the real power losses arising from the fluctuating phase angle differences.

To define the relevant performance measure, we adopt the approach first presented in [6]. Consider the real power loss over the edge e_{ij}, given by Ohm's law as

$$P_{ij}^{\mathrm{loss}} = g_{ij} |v_i - v_j|^2,$$

where $v_i = V_i e^{\mathbf{j}\theta_i}$ denotes complex voltage. If we enforce the linear power flow assumptions and retain only the terms that are quadratic in the state variables, standard trigonometric methods give that $P_{ij}^{\text{loss}} \approx g_{ij}(\theta_i - \theta_j)^2$. Since θ_i, θ_j represent deviations from an operating point, this is equivalent to the power loss over the edge during the transient. The corresponding sum of instantaneous, transient resistive power losses over all links in the network can then be approximated as

$$\mathbf{P}^{\text{loss}} = \sum_{e_{ij} \in \mathcal{E}} g_{ij}(\theta_i - \theta_j)^2. \tag{4.6}$$

We can now make use of the conductance matrix L_G from (2.19) to rewrite (4.6) as the quadratic form

$$\mathbf{P}^{\text{loss}} = \theta^* L_G \theta. \tag{4.7}$$

Since L_G is a positive semidefinite graph Laplacian, it has a unique positive semidefinite square-root $L_G^{1/2}$. We can therefore define an output of the system (4.5) as follows:

Definition 4.1 (Price of synchrony performance output) The instantaneous resistive power losses in a network are measured as $\mathbf{P}_{loss} = y^* y$, where the performance output y is

$$y := L_G^{1/2}\theta \tag{4.8}$$

Note that this performance measure, as most easily seen from (4.6), represents the sum of squared weighted differences in states between neighboring nodes, that is, a sum of squared *local* errors over the networks. The expected value of (4.6) can therefore be written as a sum over local error variances on the form (1.11).

For ease of reference we rewrite the state dynamics (4.5) and the output equation (4.8) together as the MIMO LTI system

$$\frac{\mathrm{d}}{\mathrm{d}t} \begin{bmatrix} \theta \\ \omega \end{bmatrix} = \begin{bmatrix} 0 & I \\ -M^{-1}L_B & -M^{-1}D \end{bmatrix} \begin{bmatrix} \theta \\ \omega \end{bmatrix} + \begin{bmatrix} 0 \\ M^{-1} \end{bmatrix} w, \tag{4.9a}$$

$$y = \begin{bmatrix} L_G^{1/2} & 0 \end{bmatrix} \begin{bmatrix} \theta \\ \omega \end{bmatrix}. \tag{4.9b}$$

This LTI system is a *Linear Quadratic* approximation of the full nonlinear problem in the sense that the dynamics have been linearized around an equilibrium corresponding to the condition where the power flows in the system are balanced and all generators are operating at a nominal frequency. The instantaneous resistive power losses are quadratically approximated by the square of the Euclidean norm of the output signal y. We next describe how these losses can be evaluated through the system's input-output $\mathcal{H}_2$ norm.

Remark 4.1 The system (4.9a) represents linearized dynamics in which line resistances are not present in the first approximation, having been assumed small compared to the line reactances. The output (4.9b) represents a quadratic approximation of the power losses and measures the effect of non-zero line resistances,

given the state trajectories arising from the system dynamics. A justification for these assumptions is given in Chapter 5, where line resistances are accounted for in the dynamics.

4.3.1 $\mathcal{H}_2$ norm interpretations for swing dynamics

The LTI system (4.9) is formulated so that the square of the Euclidean norm of the output $y(t)^*y(t)$ is the instantaneous resistive power loss at time t. The $\mathcal{H}_2$ norm of this system can be interpreted as the average (per time t) power loss in a setting with persistent disturbances, or alternatively as the total (over all time) power loss due to a transient event. These interpretations of the $\mathcal{H}_2$ norm relate to its standard intepretations given in Section 2.1. Here, we summarize physical scenarios which permit the input-output $\mathcal{H}_2$ norm of (4.9) to quantify resistive losses.

i. **Response to a white stochastic input.** When the input w is "white noise", the system's $\mathcal{H}_2$ norm is

$$||H||_2^2 = \lim_{t \to \infty} \mathbb{E}\{y^*(t)y(t)\}. \qquad (4.10)$$

For the swing dynamics (4.9) the disturbance vector w can be thought of as persistent stochastic forcing at each generator. These disturbances, which are uncorrelated across generators, can be due to uncertainties in local generator conditions, such as changes in local load or supplied mechanical power. The expression (4.10) is then exactly the expectation of the total (over the entire network) instantaneous power losses.

ii. **Response to a random initial condition.** For (4.9) it holds that $\mathcal{B}\mathcal{B}^* = \begin{bmatrix} 0 & 0 \\ 0 & M^{-2} \end{bmatrix}$, which is diagonal. Therefore, an initial condition ψ_o which is a random variable with correlation $\mathbb{E}\{\psi_o\psi_o^*\} = \mathcal{B}\mathcal{B}^*$ corresponds to each generator having a random initial velocity perturbation that is uncorrelated across generators and zero initial phase perturbation. In this case, the $\mathcal{H}_2$ norm

$$\|H\|_2^2 = \int_0^\infty \mathbb{E}\{y^*(t)y(t)\} \, \mathrm{d}t \qquad (4.11)$$

quantifies the total (over all time and the entire network) expected resistive power losses due to the system returning to a synchronized state.

iii. **Sum of impulse responses.** Consider a scenario where an impulse can be fed at each generator node with equal probability. For the system (4.9), this input scenario corresponds to each generator being subject to impulse force disturbances (note, w enters into the momentum equation of each generator). Such disturbances could occur, for example, due to changed operation of the

generator, a sudden lost load at the bus or a fault event. In these cases, the $\mathcal{H}_2$ norm

$$\|H\|_2^2 \;=\; \sum_{i=1}^{N} \int_0^{\infty} y_i^*(t) y_i(t) \;\mathrm{d}t. \tag{4.12}$$

quantifies the total (over all time and the entire network) expected resistive power losses due to the system returning to a synchronized state.

4.3.2   Relations to network coherence

The LTI model (4.9a) is very similar to the model of vehicular dynamics studied in Chapter 3. The notion of *network coherence* studied there can be translated into the present context of power networks as quantifying how tightly the phases of all generators drift together. More precisely the following quantity

$$\mathbb{E}\left\{ \left(\theta_i - \frac{1}{N} \sum_{j=1}^{N} \theta_j \right)^2 \right\}, \tag{4.13}$$

expresses the variance of the deviation of the ith node from the average over all nodes in the network. This quantity is never zero when there are stochastic disturbance inputs, even in a stable power network. Larger variances of relative phase deviations would reflect a more disordered network while smaller variances imply a more coherent network.

In Chapter 3, we studied the asymptotic behavior (in network size N) of the performance measure (4.13) for systems with regular network structures. It was, among other things, found that performance depends strongly on the lattice dimesion (see Theorem 3.1), which implies that more interconnected networks tend to be more coherent and vice versa. In that analysis however, performance was considered as *per vehicle*, while in the present context, it is the *total* or aggregate transient resistive power loss over the entire network that is of concern. Thus, although the two settings have analogous dynamics, the performance objectives differ.

We point out that the disorder measure (4.13) is not the Euclidean norm of the output y defined in (4.9b). In other words, the amount of phase disorder in a network as measured by (4.13) is not necessarily related to resistive power losses, and in particular may not scale similarly with network size N or have the same dependence on network connectivity. While networks with high phase coherence may be desirable for other reasons (such as stability of the nonlinear model), the results to be presented shortly indicate that the price of synchrony (total transient resistive power losses) can be large even in highly coherent networks.

4.4   Evaluating resistive losses

In this section we derive a formula for the $\mathcal{H}_2$ norm of the system (4.9) in terms of the system's parameters. We then consider the implications for some important special cases. Throughout this section we make the following simplifying assumption, which allows us to derive analytic expressions for the $\mathcal{H}_2$ norm:

Assumption 4.1 (Identical generators)   All synchronous generators have identical inerta and damping coefficients, that is, $m_i = m$ and $d_i = d$ for all $i \in \mathcal{V}$. This gives $M = mI$ and $D = dI$.

4.4.1   System reduction

As previously discussed, L_G and L_B are weighted graph Laplacians and as such, they each have a zero eigenvalue, see Section 2.3.1. The zero eigenvalue implies that these matrices are singular and that the system (4.9) is not asymptotically stable. However, as in Chapter 3, the corresponding mode is not observable from the performance output y, which is shown formally for the system at hand in the Appendix. Assuming the network to be connected, remaining eigenvalues are strictly in the left half of the complex plane, and the system therefore has a finite $\mathcal{H}_2$ norm.

In order to rigorously evaluate the $\mathcal{H}_2$ norm of (4.9) we perform a system reduction procedure that effectively removes the unobservable mode at zero and enables us to investigate a reduced system that is asymptotically stable.

We derive this reduced system by first defining a reference state $k \in \mathcal{V}$. By then deleting the kth rows and columns of L_G and L_B, we obtain the reduced or *grounded* Laplacians $\tilde{L}_G$ and $\tilde{L}_B$ (see e.g. [34]). The states of the reduced system $\tilde{\theta}$ and $\tilde{\omega}$ are then obtained by discarding the kth elements of each state vector. This leads to a system that is equivalent to one in which $\theta_k = \omega_k \equiv 0$ for some node $k \in \mathcal{V}$. The physical interpretation of the reduced system is that the kth node is connected to ground, and a corresponding mechanical analogy is shown in Figure 4.2. We call the resulting reduced, or grounded, system $\tilde{H}$ and rewrite it as

$$\frac{\mathrm{d}}{\mathrm{d}t} \begin{bmatrix} \tilde{\theta} \\ \tilde{\omega} \end{bmatrix} = \begin{bmatrix} 0 & I \\ -\frac{1}{m}\tilde{L}_B & -\frac{d}{m}I \end{bmatrix} \begin{bmatrix} \tilde{\theta} \\ \tilde{\omega} \end{bmatrix} + \begin{bmatrix} 0 \\ \frac{1}{m}I \end{bmatrix} \tilde{w} =: \mathcal{A}\tilde{\psi} + \mathcal{B}\tilde{w}; \tag{4.14a}$$

$$\tilde{y} = \begin{bmatrix} \tilde{L}_G^{\frac{1}{2}} & 0 \end{bmatrix} \begin{bmatrix} \tilde{\theta} \\ \tilde{\omega} \end{bmatrix} =: \mathcal{C}\tilde{\psi}, \tag{4.14b}$$

where the reduced state vector is $\tilde{\psi} = \begin{bmatrix} \tilde{\theta} & \tilde{\omega} \end{bmatrix}^T$. Assuming a network where the underlying graph is connected, the grounded Laplacians $\tilde{L}_G$ and $\tilde{L}_B$ are positive definite Hermitian matrices (see, for example, [52] for a proof). All eigenvalues of the system $\tilde{H}$ are thus strictly in the left half plane and it is evident that the input-output transfer function from $\tilde{w}$ to $\tilde{y}$ has a finite $\mathcal{H}_2$ norm.
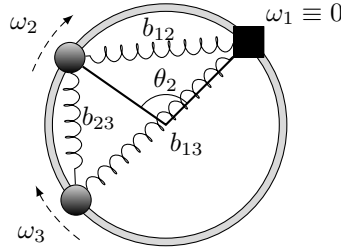
Figure 4.2: Mechanical analogy to the grounded network.

Remark 4.2 The dynamics of the grounded system (4.14) are not equivalent to those of the original system. In particular, the eigenvalues, and thereby the swing modes, differ. This can be understood intuitively by comparing Figure 4.2 to Figure 1.3. However, as we will show, the two systems are equivalent in terms of the performance metric considered here.

4.4.2 $\mathcal{H}_2$ norm calculation

The squared $\mathcal{H}_2$ norm of the system $\tilde{H}$ can be calculated through the equations (2.7) – (2.8). We call the obsevability Gramian X and partition it into four submatrices. The Lyapunov equation (2.8) expanded for our system (4.14) is then

$$
\begin{bmatrix} 0 & -\frac{1}{m}\tilde{L}_B \\ I & -\frac{d}{m}I \end{bmatrix} \begin{bmatrix} X_1 & X_0 \\ X_0^* & X_2 \end{bmatrix} + \begin{bmatrix} X_1 & X_0 \\ X_0^* & X_2 \end{bmatrix} \begin{bmatrix} 0 & I \\ -\frac{1}{m}\tilde{L}_B & -\frac{d}{m}I \end{bmatrix} = -\begin{bmatrix} \tilde{L}_G & 0 \\ 0 & 0 \end{bmatrix},
$$

from which we extract the following two equations:

$$
X_0 - \frac{d}{m}X_2 + X_0^* - X_2\frac{d}{m} = 0 \tag{4.15a}
$$

$$
-\frac{1}{m}\tilde{L}_B X_0^* - X_0 \frac{1}{m}\tilde{L}_B = -\tilde{L}_G. \tag{4.15b}
$$

Then, using (4.15a) it is straightforward to compute $\frac{d}{m}\mathrm{tr}(X_2) = \mathrm{tr}(\mathrm{Re}\{X_0\})$. Equation (4.15b) can be rearranged to yield

$$
\tilde{L}_B X_0^* \tilde{L}_B^{-1} + X_0 = m\tilde{L}_G \tilde{L}_B^{-1},
$$

where we make use of the fact that $\tilde{L}_B$ is nonsingular. Combining these expressions and using standard matrix trace relationships leads to the following expression

$$
\mathrm{tr}\left(X_2\right) = \frac{m^2}{2d}\mathrm{tr}\left(\tilde{L}_B^{-1}\tilde{L}_G\right). \tag{4.16}
$$

Finally, noting that $\mathrm{tr}(\mathcal{B}^* X \mathcal{B}) = \frac{1}{m^2}\mathrm{tr}(X_2)$, we derive the following Lemma.

Lemma 4.1 *The squared $\mathcal{H}_2$ norm of the input-output mapping of the system* (4.14) *is given by*

$$||\tilde{H}||_2^2 = \frac{1}{2d}\mathrm{tr}\left(\tilde{L}_B^{-1}\tilde{L}_G\right),\tag{4.17}$$

where $\tilde{L}_B$ and $\tilde{L}_G$ are the grounded Laplacians obtained using the procedure described above and d is each generator's self damping.

The choice of grounded node k has no influence on the $\mathcal{H}_2$ norm in (4.17). We illustrate this point through the following lemmas, which are used derive the main result of Theorem 4.4.

Lemma 4.2 *Let H denote the input-output mapping (4.9) under Assumption 4.1, and let $\tilde{H}$ denote the corresponding reduced system (4.14). Then, the norm $||H||_2^2$ exists and*

$$||H||_2^2 = ||\tilde{H}||_2^2.$$

Proof: See Appendix.

■

Lemma 4.3 *Let $\tilde{L}_G$ and $\tilde{L}_B$ be the reduced, or grounded, Laplacians obtained by deleting the kth row and column of L_G and L_B respectively. Then*

$$\mathrm{tr}\left(\tilde{L}_B^{-1}\tilde{L}_G\right) = \mathrm{tr}\left(L_B^{\dagger}L_G\right),\tag{4.18}$$

where † denotes the Moore-Penrose pseudo inverse.

Proof: See Appendix.

■

Remark 4.3 Lemma 4.3 extends to *any* pair of weighted graph Laplacians L_G, $L_B \in \mathbb{C}^{N\times N}$, even if they do not have the same underlying graph. It is, however, a requirement that the graph underlying L_B is connected (so that $\tilde{L}_B$ is nonsingular). This implies that the network grounding approach introduced here is amenable to any performance output that satisfies $y^*y = \theta^*L_{G'}\theta$ where $L_{G'}$ is some graph Laplacian. In particular, one could use this to measure performance over a subnetwork of $\mathcal{G}$.

Our main result can now be stated in the following theorem, which was also independently derived in [69].

Theorem 4.4 *Given a network of N synchronous generators whose input-output response is given by (4.9). Under Assumption 4.1, the squared $\mathcal{H}_2$ norm of the system is given by*

$$\boxed{||H||_2^2 = \frac{1}{2d}\mathrm{tr}\left(L_B^\dagger L_G\right).}$$ (4.19)

Thus, the total transient losses of the system are a function of what we term the generalized Laplacian ratio of L_G to L_B.

Proof: The result follows directly from Lemmas 4.1 - 4.3.

∎

In (4.9), we assumed that the mechanical input $P_{m,i}$ to each generator i is lumped into the input w. If, instead, one chooses to scale the input by the generator's inertia, that is, define $w' := \frac{1}{m}w$ and $\mathcal{B}' := [0 \; I]^T$, then the squared $\mathcal{H}_2$ norm of the resulting system can be constructed in an analogous manner, as shown in the following Corollary.

Corollary 4.5 *Consider the modified input-output mapping*

$$\frac{d}{dt}\begin{bmatrix} \theta \\ \omega \end{bmatrix} = \begin{bmatrix} 0 & I \\ -\frac{1}{m}L_B & -\frac{d}{m}I \end{bmatrix}\begin{bmatrix} \theta \\ \omega \end{bmatrix} + \begin{bmatrix} 0 \\ I \end{bmatrix}\mathrm{w}'$$ (4.20)

$$y = \begin{bmatrix} L_G^{1/2} & 0 \end{bmatrix}\begin{bmatrix} \theta \\ \omega \end{bmatrix}.$$

The squared $\mathcal{H}_2$ norm of this system is

$$||H'||_2^2 = \frac{m^2}{2d}\mathrm{tr}\left(L_B^\dagger L_G\right).$$

Proof: Following the proof of Lemma 4.1, we first note that for this modified system $\mathrm{tr}(\mathcal{B}'^* X \mathcal{B}') = \mathrm{tr}(X_2)$. The result then follows directly from Lemmas 4.2 and 4.3.

∎

Theorem 4.4 states that the price of synchrony (the transient resistive losses) are proportional to what can be thought of as a *generalized ratio* between the conductance and susceptance matrices. The ratio of line conductance to susceptance, or equivalently, resistance to reactance, is generally small for transmission

systems and is therefore often neglected in power flow calculations [42] and stability analyses. However, the matrix trace operation in equation (4.19) implies that the transient resistive losses increase with network size (number of generators). Therefore, transient resistive losses may become significant in large networks with highly distributed generation even when line resistances are small. In low to medium voltage networks where distributed generation (DG) units are typically connected, the resistance-to-reactance ratios are higher than in transmission systems[1]. In such networks, this trend would be doubly problematic, as both the network size and the resistance-to-reactance ratio are larger. The next section explores these effects directly for the important special case of uniform resistance-to-reactance ratios across the network.

4.4.3 Special Case: Uniform line ratios

We now consider the special case when the generalized Laplacian ratio in (4.19) is a scalar matrix αI, where

$$\alpha := \frac{g_{ij}}{b_{ij}} = \frac{r_{ij}}{x_{ij}}.$$

In other words, all network lines $e_{ij} \in \mathcal{E}$ have equal resistance-to-reactance ratios. This assumption implies that the conductance matrix is a scalar multiple of the susceptance matrix,

$$L_G = \alpha L_B, \tag{4.21}$$

and, of course, the same holds for the reduced Laplacians: $\tilde{L}_G = \alpha \tilde{L}_B$.

In this case, the Lemmas 4.1 and 4.2 give that

$$||H||_2^2 = \frac{1}{2d}\text{tr}(\tilde{L}_B^{-1}\alpha\tilde{L}_B) = \frac{\alpha}{2d}(N-1), \tag{4.22}$$

which is the result presented in [6]. This result is remarkable in that it says that, for this special case, the size of the transient losses depends only on the network's size and is entirely independent of its topology.

Remark 4.4 If we instead define a network-dependent weighted mean $\overline{\alpha}$ of the line ratios $\alpha_{ij} = \frac{g_{ij}}{b_{ij}}$ for all lines $e_{ij} \in \mathcal{E}$, the result in (4.22) can be generalized to a system with heterogeneous line ratios [69].

Remark 4.5 A choice of $\alpha_{max} \geq \frac{g_{ij}}{b_{ij}}$ for all edges $e_{ij} \in \mathcal{E}$, can be used to define a conservative bound based on (4.22). One can similarly define a lower bound $\alpha_{min} \leq \frac{g_{ij}}{b_{ij}}$ and bound the $\mathcal{H}_2$ norm of the system as:

$$\frac{\alpha_{\min}}{2d}(N-1) \leq ||H||_2^2 \leq \frac{\alpha_{\max}}{2d}(N-1), \tag{4.23}$$

where $\alpha_{min(max)}$ are the respective upper and lower bounds. These bounds, which were also proposed in [69], both increase unboundedly with the number of generators and are independent of the network topology.

---

[1]Typically, this ratio is 1/16 in 400 kV lines but 2/3 in 11 kV systems [32].

Performance scaling and topology independence

Using the notation from Chapter 3, the result (4.23) implies that

$$||H||_2^2 \sim \frac{1}{\beta}N, \tag{4.24}$$

where we can identify the algorithm parameter β with the generator damping d. We can therefore, in the same way as in Chapter 3, regard this result as a fundamental limitation to performance in uniform power networks, in which the swing equation (4.4) is the means by which synchrony is achieved. It is important to note that the scaling (4.24) is independent of the network topology, unlike the coherence scalings in Theorem 3.1.

This topology independence is also in contrast to other measures of power system stability and performance metrics. For example, the topology of the system plays an important role in determining whether a system of this kind can synchronize [62, 18, 19, 67]. The network connectivity of a power system is also directly related to its rate of convergence and damping properties [49]. Some intuition for the price of synchrony being independent of network topology in the case of uniform line ratios can be given as follows. We expect a highly interconnected network to have much more phase coherence than a loosely interconnected network with the same number of nodes. Consequently the power flows per link in a highly connected network are relatively small, but there are many more links than in the loosely connected network. Thus in the aggregate, the total transient power losses are the same for both networks. A more coherent network is, however, in many ways more stable.

Motivation for uniform line ratio assumption

The equal line ratio assumption is not unreasonable for power systems, as the ratio of resistances to reactances of typical transmission links tend to lie within a small interval. This assumption is used in many related studies, such as [48, 23], and it can be motivated by a uniformity in the physical line properties in the network. A recent study [53] also found that the node degrees of Kron-reduced networks tend to be much more uniform than than those of the full power networks that they are derived from. Those results suggest that the "lines" of such reduced systems are also more uniform than those found in actual power networks and therefore the equal line ratio assumption is suitable for the reduced network considered here.

In Example 4.1, we demonstrate numerically that the result (4.22) is a good approximation of (4.19), when is α is chosen as the average line ratio. In other words, the uniform line ratio assumption only leads to small errors with respect to the performance measure of interest. In Chapters 5 – 6 we will return to this assumption in order to make the developments and results more tractable.

4.5 Generalizations and bounds

In this section, we provide bounds on the $\mathcal{H}_2$ norm in Theorem 4.4 and discuss their implications. We also address the more general case of systems with non-identical generators.

4.5.1 Loss Bounds

As previously mentioned, the term $\text{tr}(L_B^\dagger L_G)$ in Theorem 4.4 can be interpreted as a generalized ratio between the power network's conductance matrix L_G and its susceptance matrix L_B. That is, a generalized ratio between the real and imaginary part of the bus admittance matrix (without the shunt admittances). Let us henceforth denote the respective eigenvalues of L_G as $\lambda_N^G \geq ... \geq \lambda_2^G > 0$ and of L_B as $\lambda_N^B \geq ... \geq \lambda_2^B > 0$. The generalized ratio of these two Laplacians can then be lower bounded in terms of their eigenvalues as

$$\text{tr}\left(L_B^\dagger L_G\right) \geq \sum_{i=2}^N \frac{\lambda_i^G}{\lambda_i^B}, \tag{4.25}$$

(see e.g. [87] for a proof). In the case of uniform line ratios, each eigenvalue ratio is equal to α, and the inequality in (4.25) turns into an equality. The unbounded growth of the transient resistive losses with the network size N, which was noted in (4.24), can also be seen from (4.25). In particular, the scaling with network size is evident because the number of eigenvalues, and thus the number of summands, grows with each added node. We illustrate this growth and the tightness of the bound in (4.25) through Example 4.2.

The inequality (4.25) also provides some insight into why the $\mathcal{H}_2$ norm does not have a strong dependence on network connectivity even for networks of non-identical line ratios. Although the eigenvalues of the Laplacian are difficult to characterize precisely for general graphs, it is well known that they relate strongly to the node degrees (see, for example, [15, 86]). In (4.25) however, we consider the ratio between the eigenvalues of L_G and L_B. Since these are two graph Laplacians describing the same topology, their node degrees g_{ii} and b_{ii} can be related through $\bar{\alpha}_i$, the average ratio of line conductances to susceptances of the lines incident to node i. This $\bar{\alpha}_i$ is independent of *how many* such incident lines there are. It is therefore reasonable to infer that each eigenvalue ratio $\frac{\lambda_i^G}{\lambda_i^B}$ is also more strongly related to $\bar{\alpha}_i$ than to the number of lines connected to each node, which would be a measure the network connectivity. We will further explore this notion through the examples in Section 4.6.

As shown in Remark 4.5, the resistive losses can also be bounded as (4.23), which allows for a simple and convenient analysis of the network, which simultaneously reveals the scaling of the performance measure with network size. However, the bound may become loose if the system is heterogenous in terms of the line resistance-to-reactance ratios. This may be the case if a combined transmission and

distribution network is considered, or in cases of highly varying impedance loads. In some cases, it is then better to bound the losses in terms of graph-theoretical quantities. This can be done in the following manner.

$$\lambda_2^G \text{tr}(L_B^\dagger) \leq \text{tr}(L_B^\dagger L_G) \leq \frac{\text{tr}(L_G)}{\lambda_2^B}, \tag{4.26}$$

where λ_2^G and λ_2^B are the *algebraic connectivities* of the graphs weighted by line conductances and susceptances respectively. See [87] for a proof of (4.26).

In general, it holds that $\lambda_2^G \leq \frac{N}{N-1} g_{ii,\min}$ and $\lambda_2^B \leq \frac{N}{N-1} b_{ii,\min}$, where g_{ii}, b_{ii} are the respective node degrees in the weighted conductance and susceptance graphs. Furthermore, the quantity $\text{tr}(L_B^\dagger)$ is proportional to what we can interpret as the *total effective reactance* of the network, in analogy with the concept of graph total effective resistance, as recently discussed in e.g. [34, 28, 37]. By Rayleigh's monotonicity law (see [24]), the total effective reactance can decrease unboundedly by adding lines and increasing line susceptances. However, the algebraic connectivity λ_2 is very small for weakly connected networks and can also be found to decrease with network size. Therefore, while the bounds (4.26) where λ_2 appears in the denominator, are accurate for small and well-connected networks, they become loose for the large, sparsely interconnected networks. The usefulness of the bound (4.26) therefore depends on the network type.

4.5.2   Systems of Non-Identical Generators

The results derived under Assumption 4.1, that is, by considering a grid with identical generators, suggest that the losses scale with the network size as in (4.24). In order to put these results in context it is desirable to understand the extent to which these scaling properties apply to systems of non-uniform generators. In this section we explore these ideas and use the results from previous sections to gain some insight. We begin by examining the special case where one non-uniform generator is added to the network.

From Theorem 4.4 we can deduce that

$$\frac{1}{2d_{\max}} \text{tr}\left(L_B^\dagger L_G\right) \leq \|H\|_2^2 \leq \frac{1}{2d_{\min}} \text{tr}\left(L_B^\dagger L_G\right),$$

where $d_{\min} = \min_{i \in \mathcal{V}} d_i$ and $d_{\max} = \max_{i \in \mathcal{V}} d_i$. The losses are thus lower and upper bounded by the properties of the most strongly and lightly damped generators respectively, and the overall scaling in (4.24) remains valid. However, not only the losses' scaling matters, but also their actual values, since they represent an actual cost in the network. Therefore, some interesting questions that arise are: (1) How does adding a generator to an existing network affect the total resistive losses? and (2) What are the important parameters in determining this incremental cost? The next result addresses one such scenario.

Lemma 4.6 *Consider a network of N generators with transient resistive losses given by $||H_0||_2^2$. If one connects an additional generator with damping d_{N+1} and inertia m_{N+1} to any node $k \in \{1, \dots, N\}$ in the existing network by a single link with line ratio of $\alpha_{k,N+1} = \frac{r_{k,N+1}}{x_{k,N+1}}$, then the new network's losses are given by*

$$||H_1||_2^2 = ||H_0||_2^2 + \frac{1}{2d_{N+1}}\alpha_{k,N+1}.$$

If the dynamics are as per (4.20) the additive term is instead $\frac{m_{N+1}^2}{2d_{N+1}}\alpha_{k,N+1}$.

Proof: See Appendix.

∎

This result can be interpreted as follows. The additional losses incurred through the connecting a "light" (low inertia) or well damped generator are smaller than those incurred due to adding a "heavy" (high inertia) or poorly damped generator. In the face of increasingly distributed generation, this result implies that while the synchronization losses do scale with the network size, the impact of low inertia or small-scale distributed generators is relatively low, compared to that of large conventional generators.

In this thesis, we will not present further analytical results for systems with non-identical generators, but carry out most of the analysis under Assumption 4.1. The numerical Example 4.3, however, provides some further insight into performance of networks with non-uniform generation. That example shows that, although the scaling relationships and topology independence results hold for limited parameter variations, judicious sizing and placement of new generators can in fact improve performance. This fact is further explored in a recent study by Poolla *et al.* [63], which studies optimal placement of inertia in power networks.

4.6 Numerical examples

The results derived in the previous sections indicate that the price of synchrony is highly dependent on the number of generators in the system. They were also found to depend on the system's resistance-to-reactance ratios and the generator properties, but only weakly on the network topology. In this section, we provide some numerical examples to illustrate these results and to explore more general networks.

Example 4.1 (Non-uniform line ratios: increasing line ratio variance) We first investigate the price of synchrony in systems with increasingly non-uniform network line ratios α_{ij} (defined in Section 4.4.3). We consider a hypothetical set of identical generators with $d = 1$ placed at each node of, respectively, the IEEE 14 bus, 30
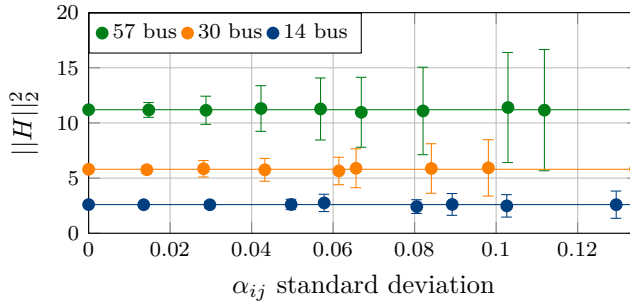
Figure 4.3: $\mathcal{H}_2$ norms from Example 4.1 for the IEEE 14 bus, 30 bus, and 57 bus benchmark networks. The edge weights are randomly generated using increasingly varying resistance-to-reactance ratios $\alpha_{ij} = \frac{r_{ij}}{x_{ij}}$. The bars illustrate the bounds in (4.23).

bus and 57 bus benchmark topologies [55]. We take the values for the reactances x_{ij} for each $e_{ij} \in \mathcal{E}$ from the benchmark system data. We then define a random series of heterogeneous line ratios by setting $r_{ij} = \alpha_{ij} x_{ij}$, where the α_{ij} are each drawn once from uniform distributions on the following range of intervals: $0.4, \; 0.4\pm 0.025, \; 0.4 \pm 0.05, ..., 0.4 \pm 0.2$.

Figure 4.3 shows the resistive losses computed from the result in Theorem 4.4 for a number of these systems. The horizontal axis indicates the standard deviation of the line ratios and the bars represent the upper and lower bounds of the inequality (4.23).

This example shows that increasing the standard deviation of the line ratios leads to a looser bound in (4.23). However, the actual resistive losses show only small variations as long as the average line ratio remains constant. We can also note that the transient losses depend strongly on the network size (here 14, 30 or 57 nodes), which is consistent with the relationship in (4.22).

Example 4.2 (Performance scaling and bounds for topology extremes) We now demonstrate the fact that the price of synchrony is only weakly dependent on network topology, but instead scales with the total number of network nodes. We compare the $\mathcal{H}_2$ norm in (4.19) and the bounds discussed in Section 4.5 for two systems where the underlying topology is (a) a path graph, and (b) a complete graph (see Figure 4.4) and let their respective system size increase. These two topologies are chosen because they represent the two extremes with respect to connectivity. Therefore, they demonstrate our, perhaps counterintuitive, result that the price of synchrony does not depend on network connectivity. In Chapters 5 – 6, where we change the control dynamics, we will return to these two types of networks and there find that they sometimes differ in terms of this performance objective.

We simplify the problem by assuming uniform dampings $d = 1$ for all generators
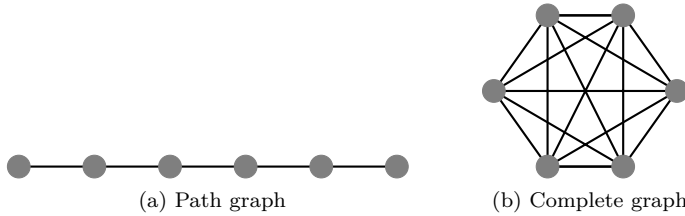
(a) Path graph   (b) Complete graph

Figure 4.4: The path graph and complete graph topologies over 6 nodes.

in the network and then assign random line parameters to each line in the following manner. We draw both the line reactance x_{ij} and line ratio α_{ij} from a normal distribution with mean 0.2 and standard deviation 0.1 (and replace any negative values by the mean). By the previous example, one can then expect the norm for each network to lie close to the result of equation (4.22) based on the mean ratio $\bar{\alpha} = 0.2$, and we should expect a linear relationship in N. This is also the main trend in Figure 4.5.

Figure 4.5 shows the $\mathcal{H}_2$ norms for the path and complete graph topologies as the network size increases from a 5 node to a 50 node system. We also indicate the bounds (4.23) and (4.25) on both panels. Due to space constraints we show the bounds in (4.26) only in Figure 4.5b as this bound is very loose in the case of path graphs. For both types of networks, the eigenvalue ratio bound in (4.25) provides the tightest bound. We also note that the network-parameter dependent bounds (4.26) are more accurate than the line ratio bounds (4.23) for the complete graph.

Example 4.3 (Placement of generators with non-uniform damping) Our final example further relaxes Assumption 4.1 of equal generator parameters. We consider again our 7 bus example network from Figure 4.1, and let the lines have equal line impedances $z_{ij} = 0.1 + \mathbf{j}0.6 = z_o$. The nodes in this network have the following degrees in terms of the impedance z_o:
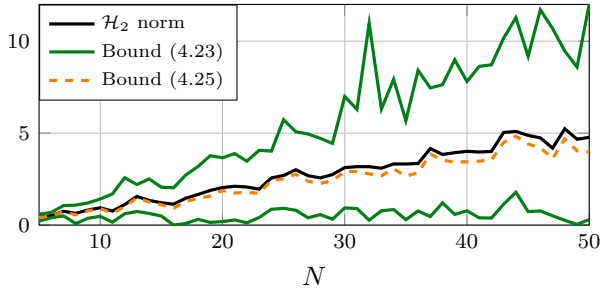
$$\delta_1 = \delta_7 = z_o, \quad \delta_2 = \delta_6 = 3z_o, \quad \delta_3 = \delta_5 = 2z_o, \quad \delta_4 = 4z_o.$$

The nodes thus have four different degrees, and we will now place four different generators $A - D$ at them. These generators all have inertia $m = \frac{20}{2\pi f}$, but we let the dampings be
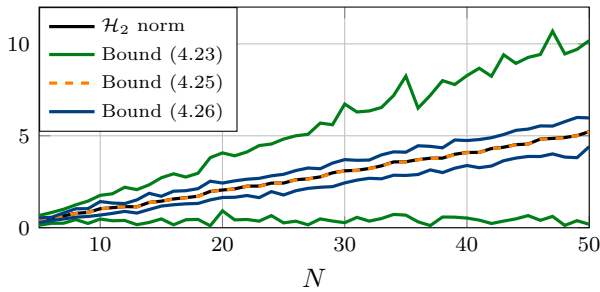
$$d_A = \frac{2}{2\pi f}, \ d_B = \frac{8}{2\pi f}, \ d_C = \frac{14}{2\pi f}, \ d_D = \frac{20}{2\pi f}.$$

The situation is depicted in Figure 4.6.

We study this system under two conditions:

(a) Path graph

(b) Complete graph

Figure 4.5: $\mathcal{H}_2$ norms from Example 4.2 for a (a) path graph and a (b) complete graph network of N nodes, with some of the bounds from in Section 4.5. Despite some variation due to the randomness in the line parameters, the $\mathcal{H}_2$ norm scales directly with the network size and is roughly the same for the path as for the complete graph. The bound related to the Laplacian eigenvalue ratios (4.25) is the most accurate bound, and for the complete graph, the inequality (4.26) linked to the algebraic connectivity λ_2, also provides accurate bounds (for the radial graph, the latter have been left out since they are off by orders of magnitude due to small connectivity).

(a) The strongly damped generators placed at the *most* interconnected nodes:

$$
\begin{aligned}
d_A &\rightarrow \text{ nodes 1 and 7} \\
d_B &\rightarrow \text{ nodes 3 and 5} \\
d_C &\rightarrow \text{ nodes 2 and 6} \\
d_D &\rightarrow \text{ node 4}
\end{aligned}
$$

Here, dampings and node degrees are *matched*, and we call the resulting system (with node 1 grounded) $\tilde{H}_{\mathrm{match}}$.
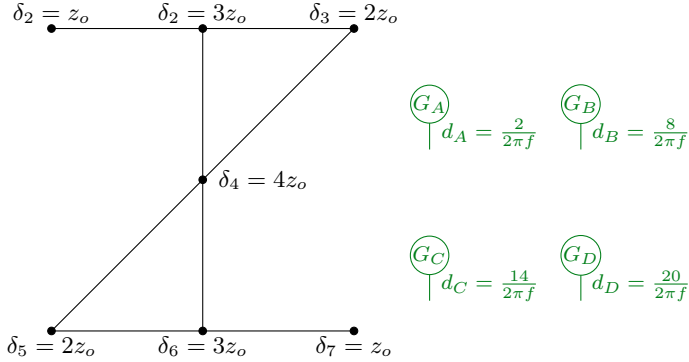
Figure 4.6: Illustration of the situation in Example 4.3. We place 4 generators with different dampings in the 7-node example network by considering the node degrees δ_i.

(b) The strongly damped generators placed at the *least* interconnected nodes:

$$\begin{aligned}
d_A &\rightarrow \text{ node 4} \\
d_B &\rightarrow \text{ nodes 2 and 6} \\
d_C &\rightarrow \text{ nodes 3 and 5} \\
d_D &\rightarrow \text{ nodes 1 and 7}
\end{aligned}$$

Here, dampings and node degrees are *mismatched*, and we call the resulting system (with node 1 grounded) $\tilde{H}_{\text{mismatch}}$.

We simulate the systems when they are subjected to a random initial angular velocity disturbance according to the $\mathcal{H}_2$ norm interpretation (ii) in Section 4.3.1. The $\mathcal{H}_2$ norms that give the expected transient power losses can be evaluated numerically to:

$$||\tilde{H}_{\text{match}}||_2^2 = 18.9, \text{ while } ||\tilde{H}_{\text{mismatch}}||_2^2 = 20.7.$$

This shows that losses are lower for the system corresponding to case (a) where the dampings are matched to the node degrees.

Figure 4.7 shows the state trajectories of the two systems for a particular input sequence. The figure shows that the transient behaviour of the system $\tilde{H}_{\text{mismatch}}$ (b) is less "coherent" than that of $\tilde{H}_{\text{match}}$ (a). Since the underlying graph, and therefore the matrix L_G in the performance output, is the same, it is clear in this case that the additional oscillations in the mismatched case (b) lead to increased transient losses. For the particular trajectories shown, the random input is such that the "mismatched" network is particularly excited compared to the "matched" network and, therefore, when we compute the respective losses for the particular trajectories shown, these are for the matched case (a) 13.2, and in the mismatched case (b) 27.9.

(a) Damping size matched to node degrees   (b) Damping size mismatched to node degrees
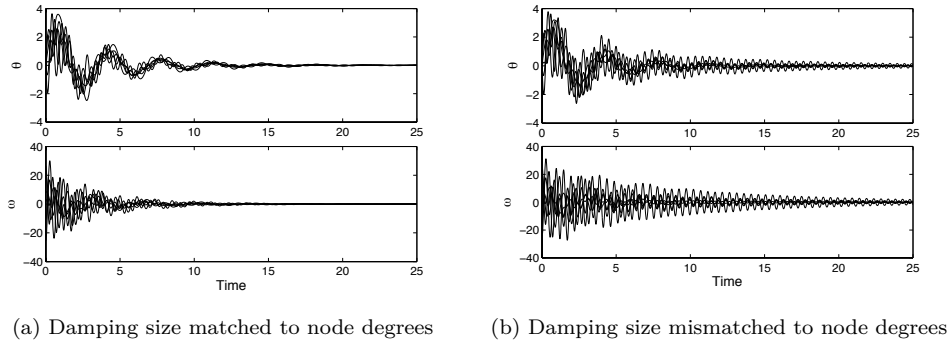
Figure 4.7: Simulation from Example 4.3 with network in Figure 4.6. In (a) the strongly damped generators are placed at the most highly interconnected nodes, and in (b) the strongly damped generators placed are at the most weakly interconnected nodes. The system in (b) is less coherent and experiences larger resistive losses during the transient response: 27.9 compared to 13.2 in system (a) for these particular trajectories.

These results and similar case studies have led us to conclude that for systems with non-uniform generator parameters, judicious network design that places well-damped generators at highly interconnected nodes can reduce transient power losses. An intuitive explanation to this is that a well-damped generator is able to exert a larger effect on the entire network if it is well-connected than if it is remotely located. However, note that although we are considering an extreme case where the best damped generator has as much as a 10 times larger damping coefficient than the most poorly damped one, performance only differs by 10% between the most optimal and least optimal generator arrangement for the particular example topology.

4.7   Concluding summary of Chapter 4

We introduced a new performance measure associated with synchronization in electric power networks. This measure quantifies resistive losses that arise due to the power flows associated with maintaining synchrony in a power network in the presence of persistent disturbances or small transient responses. These losses are the cost of using power flow through transmission lines as the signaling mechanism for synchronization control, which motivates the term "price of synchrony". In the special case of identical generators, we derived a formula for the total transient losses expressed as a generalized ratio of the weighted graph Laplacians representing the conductance and susceptance matrices. We showed that this quantity scales unboundedly with the number of nodes (generators) in the system. For the special case

where all of the transmission lines have equal conductance to susceptance ratios, we showed that the total transient resistive losses are independent of network topology, and directly proportional to the number of nodes in the network. This topological independence implies that while highly interconnected networks may have better phase coherence and stability properties than a sparsely interconnected one, the two types are equivalent in terms of the power losses associated with maintaining synchrony. While this conclusion may at first seem surprising, some intuition can be gained by considering the following contrast between highly versus sparsely interconnected networks. A highly connected, and therefore highly phase-coherent network has smaller phase fluctuations than a sparsely interconnected one. Therefore, while the "per-link" resistive losses are smaller in the former, it has many more links than the latter, and thus the total losses summed over all links are the same for both networks.

The results we present have some interesting implications for the design of future power grids. In particular, our results show that transient losses grow unboundedly with network size. In addition, they indicate that that this growth is unlikely to be mitigated by increasing network coherence through additional transmission links, unless these links focus on an optimal matching of generator dampings to node degrees (although our results show that even such strategic network design is unlikely to have a significant impact on performance). These results point to a fundamental limitation to a system where power flow is the mechanism by which the system resynchronizes or maintains a synchronous state. This performance limitation may be particularly relevant to future power networks that are likely to have orders of magnitude more generators than today's networks due to a high integration of renewable distributed generation (DG) units. In the next chapter, we will explore some further aspects of such renewable energy integrated networks.

Appendix to Chapter 4

Proof of Lemma 4.2

Consider the following state transformation of the system (4.9).

$$\begin{bmatrix} \theta \\ \omega \end{bmatrix} =: \begin{bmatrix} U & 0 \\ 0 & U \end{bmatrix} \begin{bmatrix} \theta' \\ \omega' \end{bmatrix},$$

where U is the unitary matrix which diagonalizes L_B, that is, $U^* L_B U = \Lambda_B = $ diag$\{0,\ \lambda_2^B, ..., \lambda_N^B\}$, with $0 = \lambda_1^B \leq \lambda_2^B \leq ... \leq \lambda_N^B$ being the eigenvalues of L_B. We have assumed, without loss of generality, that $U = [\frac{1}{\sqrt{N}}\mathbf{1}\ \ u_2\ ...\ u_N]$, where u_i, $i = 2, ..., N$ are the eigenvectors corresponding to the aforementioned eigenvalues.

Since the $\mathcal{H}_2$ norm is unitarily invariant, see Section 2.1.2, we can also define $w' = U^* w$ and $y' = U^* y$ to obtain the system

$$\begin{aligned} \frac{\mathrm{d}}{\mathrm{d}t} \begin{bmatrix} \theta' \\ \omega' \end{bmatrix} &= \begin{bmatrix} 0 & I \\ -\frac{1}{m}\Lambda_B & -\frac{d}{m}I \end{bmatrix} \begin{bmatrix} \theta' \\ \omega' \end{bmatrix} + \begin{bmatrix} 0 \\ \frac{1}{m}I \end{bmatrix} w' \\ y' &= \begin{bmatrix} U^* L_G^{1/2} U & 0 \end{bmatrix} \begin{bmatrix} \theta' \\ \omega' \end{bmatrix} \end{aligned}. \tag{4.27}$$

Now, observe that

$$U^* L_G U = \begin{bmatrix} 0 & \cdots & 0 \\ \vdots & & \\ 0 & & \hat{L}_G \end{bmatrix}, \tag{4.28}$$

which implies that the first rows and columns of both $U^* L_G U$ and Λ_B are zero. We thus have that the states $\theta_1' = \frac{1}{\sqrt{N}} \sum_{i=1}^N \theta_i$ and $\omega_1' = \frac{1}{\sqrt{N}} \sum_{i=1}^N \omega_i$ satisfy the dynamics

$$\dot{\theta}_1' = \omega_1' \tag{4.29a}$$

$$\dot{\omega}_1' = -\frac{d}{m}\omega_1' + \frac{1}{m}w_1' \tag{4.29b}$$

$$y_1' = 0. \tag{4.29c}$$

Equation (4.29) reveals that the associated subsystem, which we denote H_1' and that corresponds to the single zero eigenvalue of L_B, is unobservable. The remaining eigenvalues of the system (4.27) lie strictly in the left half of the complex plane because L_B is positive semidefinite. It follows that the input-output transfer function from w' to y' is stable and has finite $\mathcal{H}_2$ norm.

By the equivalence of the system (4.27) and H, we have thus established the existence of the $\mathcal{H}_2$ norm for the system H.

We can now partition the system (4.27) into the respective subsystems H_1' in (4.29) and $\hat{H}$. We take $\hat{L}_G$ as the Hermitian positive definite submatrix in (4.28)

and define $\hat{\Lambda}_B = \mathrm{diag}\{\lambda_2^B,\ \lambda_3^B,...,\lambda_N^B\}$. We then write the input-output mapping $\hat{H}$ as:

$$\frac{\mathrm{d}}{\mathrm{d}t}\begin{bmatrix}\hat{\theta}\\\hat{\omega}\end{bmatrix} = \begin{bmatrix}0 & I\\-\frac{1}{m}\hat{\Lambda}_B & -\frac{d}{m}I\end{bmatrix}\begin{bmatrix}\hat{\theta}\\\hat{\omega}\end{bmatrix} + \begin{bmatrix}0\\\frac{1}{m}I\end{bmatrix}\hat{w}$$
$$\hat{y} = \begin{bmatrix}\hat{L}_G^{1/2} & 0\end{bmatrix}\begin{bmatrix}\hat{\theta}\\\hat{\omega}\end{bmatrix} \tag{4.30}$$

or $\Leftrightarrow \frac{d}{dt}\tilde{\phi} = \mathcal{A}\tilde{\phi} + \mathcal{B}\tilde{w};\ \ \tilde{y} = \mathcal{C}\tilde{\phi}$.

Note that the systems $\hat{H}_1$ and $\tilde{H}$ are completely decoupled and we therefore have that $||H||_2^2 = ||H_1'||_2^2 + ||\hat{H}||_2^2 = ||\hat{H}||_2^2$.

The $\mathcal{H}_2$ norm of $\hat{H}$ can then be calculated in perfect analogy to the derivations in Section 4.4.2 and we obtain that

$$\|H\|_2^2 = \frac{1}{2d}\mathrm{tr}(\hat{\Lambda}_B^{-1}\hat{L}_G). \tag{4.31}$$

Now, we show that the result of Lemma 4.1, that is in terms of the reduced graph Laplacians, can be written in terms of the state transformed matrices $\hat{\Lambda}_B$ and $\hat{L}_G$. Define the $N \times (N-1)$ and the $(N-1) \times N$ matrices R and P by:

$$R = \begin{bmatrix}0 & \cdots & 0\\ & I_{N-1} & \end{bmatrix}, \ \ P = \begin{bmatrix}I_{k-1} & & 0\\ & -\mathbf{1} & \\ 0 & & I_{N-k}\end{bmatrix},$$

where k is the index of the grounded node and $\mathbf{1}$ is the $(N-1) \times 1$ vector with all entries equal to 1. By this design, $\hat{\Lambda}_B = R^*\Lambda_B R$, $\hat{L}_G = R^*U^*L_GUR$ and $L_{B(G)} = P^*\tilde{L}_{B(G)}P$. Further, to simplify notation, we define the $(N-1) \times (N-1)$ non-singular matrix $V = PUR$. Then we can write

$$\mathrm{tr}(\tilde{L}_B^{-1}\tilde{L}_G) = \mathrm{tr}(VV^{-1}\tilde{L}_B^{-1}(V^*)^{-1}V^*\tilde{L}_G),$$

since $VV^{-1} = (V^*)^{-1}V^* = I$. By the cyclic properties of the trace:

$$\mathrm{tr}(VV^{-1}\tilde{L}_B^{-1}(V^*)^{-1}V^*\tilde{L}_G) = \mathrm{tr}(V^{-1}\tilde{L}_B^{-1}(V^*)^{-1}V^*\tilde{L}_GV)$$
$$= \mathrm{tr}((V^*\tilde{L}_BV)^{-1}V^*\tilde{L}_GV). \tag{4.32}$$

But $V^*\tilde{L}_BV = R^*U^*P^*\tilde{L}_BPUR = \hat{\Lambda}_B$ and $V^*\tilde{L}_GV = R^*U^*P^*\tilde{L}_GPUR = \hat{L}_G$. Hence,

$$\mathrm{tr}(\tilde{L}_B^{-1}\tilde{L}_G) = \mathrm{tr}(\hat{\Lambda}_B^{-1}\hat{L}_G).$$

In conclusion,

$$\|H\|_2^2 = \frac{1}{2\beta}\mathrm{tr}(\hat{\Lambda}_B^{-1}\hat{L}_G) = \frac{1}{2\beta}\mathrm{tr}(\tilde{L}_B^{-1}\tilde{L}_G) = \|\tilde{H}\|_{\mathcal{H}_2}^2,$$

which proves the Lemma.

■

Proof of Lemma 4.3

By the proof of Lemma 4.2, we have that $\operatorname{tr}(\tilde{L}_B^{-1}\tilde{L}_G) = \operatorname{tr}(\hat{\Lambda}_B^{-1}\hat{L}_G)$. Now,

$$\operatorname{tr}(\hat{\Lambda}_B^{-1}\hat{L}_G) = \operatorname{tr}\left(\begin{bmatrix} 0 & 0 \\ 0 & \hat{\Lambda}_B^{-1}\hat{L}_G \end{bmatrix}\right) = \operatorname{tr}\left(\begin{bmatrix} 0 & 0 \\ 0 & \hat{\Lambda}_B^{-1} \end{bmatrix} U^* L_G U\right).$$

By definition, see e.g. [38], $U^* L_B^\dagger U = \operatorname{diag}\{0, \frac{1}{\lambda_2^B}, ..., \frac{1}{\lambda_N^B}\} = \begin{bmatrix} 0 & 0 \\ 0 & \hat{\Lambda}_B^{-1} \end{bmatrix}$, which makes the above equivalent to: $\operatorname{tr}(U^* L_B^\dagger U U^* L_G U) = \operatorname{tr}(U^* L_B^\dagger L_G U)$. But since the trace is unitarily invariant, it follows that

$$\operatorname{tr}(\hat{\Lambda}_B^{-1}\hat{L}_G) = \operatorname{tr}(L_B^\dagger L_G),$$

which concludes the proof.

■

Proof of Lemma 4.6

Without loss of generality, choose the node to which the new generator is connected as the grounded node, and let it be numbered N. Let $\tilde{M} := \operatorname{diag}\{m_1, ..., m_N\}$, $\tilde{D} = \operatorname{diag}\{d_1, ..., d_N\}$ and denote the new $(N+1)^{\text{th}}$ node as NI for notational compactness. The reduced new system $\tilde{H}_1$ can then be written as

$$\frac{\mathrm{d}}{\mathrm{d}t}\begin{bmatrix} \tilde{\theta} \\ \theta_{NI} \\ \tilde{\omega} \\ \omega_{NI} \end{bmatrix} = \begin{bmatrix} 0 & 0 & I_{N-1} & 0 \\ 0 & 0 & 0 & 1 \\ -\tilde{M}^{-1}\tilde{L}_B & 0 & -\tilde{M}^{-1}\tilde{D} & 0 \\ 0 & -\frac{b_{N,NI}}{m_{NI}} & 0 & -\frac{d_{NI}}{m_{NI}} \end{bmatrix} + \begin{bmatrix} 0 & 0 \\ 0 & 0 \\ \tilde{M}^{-1} & 0 \\ 0 & \frac{1}{m_{NI}} \end{bmatrix}\begin{bmatrix} \tilde{w} \\ w_{NI} \end{bmatrix}$$

$$(4.33)$$

$$\begin{bmatrix} \tilde{y} \\ y_{NI} \end{bmatrix} = \begin{bmatrix} \tilde{L}_G^{1/2} & 0 & 0 & 0 \\ 0 & \sqrt{g_{N,NI}} & 0 & 0 \end{bmatrix}\begin{bmatrix} \tilde{\theta} \\ \theta_{NI} \\ \tilde{\omega} \\ \omega_{NI} \end{bmatrix},$$

where $b_{N,NI}$, $g_{N,NI}$ are, respectively, the susceptance and conductance of the line $e_{N,NI}$. Let the input-output mapping H_{NI} be the SISO subsystem of (4.33) given by:

$$\frac{\mathrm{d}}{\mathrm{d}t}\begin{bmatrix} \theta_{NI} \\ \omega_{NI} \end{bmatrix} = \begin{bmatrix} 0 & 1 \\ -\frac{b_{N,NI}}{m_{NI}} & -\frac{d_{NI}}{m_{NI}} \end{bmatrix}\begin{bmatrix} \theta_{NI} \\ \omega_{NI} \end{bmatrix} + \begin{bmatrix} 0 \\ \frac{1}{m_{NI}} \end{bmatrix} w_{NI}$$

$$y_{NI} = \begin{bmatrix} \sqrt{g_{N,NI}} & 0 \end{bmatrix}\begin{bmatrix} \theta_{NI} \\ \omega_{NI} \end{bmatrix}.$$

From (4.33), it is clear that the systems $\tilde{H}_0$ and H_{NI} are entirely decoupled. We can therefore write $\tilde{H}_1 = \text{diag}\{\tilde{H}_0, \ \tilde{H}_1\}$, and have that

$$||\tilde{H}_1||_2^2 = ||H_0||_2^2 + ||H_{NI}||_2^2.$$

Now, the $\mathcal{H}_2$ norm of H_{NI} can be calculated in scalar analogy to the derivation in Section 4.4.2 to yield

$$||H_{NI}||_2^2 = \frac{1}{2d_{NI}} \frac{g_{N,NI}}{b_{N,NI}} = \frac{\alpha_{N,NI}}{2d_{NI}},$$

and since, by Lemma 4.2 $||\tilde{H}_1||_2^2 = ||H_1||_2^2$, this concludes the proof.

∎

Chapter 5

Renewable energy integrated power systems: heterogeneous networks and microgrids

Our study of power system dynamics in this thesis is to large extents motivated by ongoing changes in the electric power system. We summarized some of these changes in Examples 1.3 – 1.4 of the introduction. The overall trend is that electric power generation is becoming increasingly heterogeneous as numerous smaller, local generation resources replace large centralized power plants. In traditional power transmission systems, synchronization has typically been studied using a Kron reduced network of synchronous generators, under standard linear power flow assumptions that assume a flat voltage profile, as in Chapter 4. However, most renewable energy based power generation does not use synchronous generators, so a system of coupled swing equations cannot immediately be used to analyze systems with substantial renewable energy penetration. Furthermore, since much of this generation is connected at low to medium voltage grids where a tight voltage control is required, the assumption of flat voltage profiles is no longer valid. In this chapter, we address each of these issues separately.

We begin this chapter by a short survey of the models that we use to represent renewable energy generation. We present two such models: (a) a first-order model used to represent asynchronous generation such as induction generators in wind farms (as well as dynamic loads), and (b) models for frequency and voltage control of power electric inverters. We will then use the model (a) together with the synchronous generator model from Chapter 4 to derive a topology-preserving model of a heterogeneous power transmission system in Section 5.2. We then address the question of variable voltage dynamics by studying an inverter-based microgrid using the models (b) in Section 5.3. In both cases, we show how the model extension affects the price of synchrony performance measure introduced in Chapter 4.

5.1   Modeling renewable energy integration

Renewable energy generation units are typically interfaced with the AC network through asynchronous induction generators, or through DC/AC or AC/AC power electronic converters, or *inverters*. In some cases, such as with doubly-fed induction generators that are used to enable variable speed wind power, induction generators and power electronic converters are combined [26]. We now introduce models for the frequency dynamics for these respective systems, as well as for dynamic loads.

5.1.1   Asynchronous machine model

Based on the framework proposed by Bergen and Hill [10], we choose to model dynamic loads, as well as asynchronous induction generators, through frequency-dependent power withdrawals and injections. In the original framework, this model was proposed for dynamic loads, and we will shortly provide a justification for extending it to represent asynchronous generation.

Let $\mathcal{L}$ be a set of dynamic load buses. We model the (negative) power injection $P_{e,i}$ from each bus $i \in \mathcal{L}$ as

$$P_{e,i} = -P_{\text{load},i}^0 - k_i \omega_i, \quad i \in \mathcal{L} \tag{5.1}$$

where $P_{\text{load},i}^0$ is the constant steady-state power withdrawn at node i, $\omega_i = \dot{\theta}_i$ is the frequency and $k_i > 0$ is the frequency coefficient for each load i. Since the model (5.1) was proposed in [10] in the 80's, it has been used to represent induction motors drawing power from the grid [45]. It captures the relationship between the active power and frequency in induction machines by modeling it as a linear function of the *slip*, which is the difference between the rotational speed of the machine and the grid. Induction generators such as, for example, fixed-speed wind turbines with cage-type generators, work in precisely the same way as induction motors. Equation (5.1) is therefore also a suitable model for asynchronous induction generators. We thus model the asynchronous generators in the set $\mathcal{W}$ as frequency-dependent power injections $P_{e,i}$ of the form

$$P_{e,i} = P_{\text{wind},i}^0 - k_i \omega_i, \quad i \in \mathcal{W} \tag{5.2}$$

where $P_{\text{wind},i}^0$ is the constant steady-state input, $k_i > 0$ is the frequency coefficient for each generator and the we use the index "wind" to refer to renewable power generation in general. These power injections differ from the loads in that they enter the bus power balance with a positive sign to signify that they are injecting power to the system. The magnitude of the parameters k_i also tend to be different for loads versus renewable generation systems.

The frequency-dependent power injection model (5.2) is also applicable to the increasingly common variable speed wind farm generators and other renewable power sources such as photovoltaics that are grid-interfaced through inverters. As was already mentioned in Example 1.4, a widely proposed control scheme for power

inverters is so-called droop control. As we will see in the next section, the first-order version of this droop control law is equivalent to (5.2). We conclude, therefore, that (5.2) is well-suited to capture the physics of several types of renewable generation in power systems, that is relevant to studying frequency synchronization.

Remark 5.1 The literature offers a number of more detailed descriptions of asynchronous machines, particularly wind turbine generators [66, 25, 27], but it unclear how such models would be adapted to studies of synchronous stability [45]. A canonical modeling paradigm that captures the dynamics of interest has yet to be established [32, 75, 80].

5.1.2 Inverter and droop control model

We now introduce models for the power inverters, adopting the framwork from [67]. We assume that these inverters are AC voltage sources, where both voltage amplitude and frequency outputs can be regulated. We first consider frequency control, and introduce the frequency droop controller, which is by now a standard approach for frequency control in inverter-based networks [61, 89, 71, 72]. The focus on analyzing droop control also for voltage and reactive power stabilization in microgrids is more recent, see for example [33, 48, 67, 68]. We introduce the voltage droop controller at the end of this section.

Frequency droop control

Let the frequency output at the ith inverter be regulated according to:

$$\dot{\theta}_i = u_i^\theta, \tag{5.3}$$

where u_i is the control signal. The droop controller balances the active power demand through simple proportional control

$$u_i^\theta = \omega^{\text{ref}} - k_{P,i}(\hat{P}_i - P_i^{\text{ref}}), \tag{5.4}$$

where the controller gain $k_{P,i} > 0$ is called the *frequency droop coefficient*, ω^{ref} and P_i^{ref} are the frequency and active power setpoints, and $\hat{P}_i$ is the measured active power by the power electronics at the inverter. Following [67], we assume measurement delay dynamics where the active power is measured and processed through a low-pass filter as

$$\tau_{P,i}\dot{\hat{P}}_i = -\hat{P}_i + P_{e,i}, \tag{5.5}$$

where $\tau_{P,i} > 0$ is the time constant of the filter and $P_{e,i}$ is the actual power injection to the network at node i, given by (4.2).

Now, we substitute (5.4) into (5.3) and introduce the inverter frequency $\omega_i = \dot{\theta}_i$ to obtain

$$\omega_i = \omega^{\text{ref}} - k_{P,i}(\hat{P}_i - P_i^{\text{ref}}). \tag{5.6}$$

Taking the time derivative of (5.6) gives $\dot{\omega}_i = -k_{P,i}\dot{\hat{P}}_i$ and by (5.5) we have that $\dot{\omega}_i = \frac{k_{P,i}}{\tau_{P,i}}(\hat{P}_i - P_{e,i})$. Now, we can substitute $\hat{P}_i$ using (5.6) and obtain the frequency control dynamics as

$$\dot{\theta}_i = \omega_i$$
$$\tau_{P,i}\dot{\omega}_i = -\omega_i + \omega^{\text{ref}} - k_{P,i}(P_{e,i} - P_i^{\text{ref}}). \tag{5.7}$$

Note that the control dynamics (5.7) reduce to a first-order model if $\tau_{P,i} = 0$. In this case, we have $\dot{\theta}_i = -\omega_i + \omega^{\text{ref}} - k_{P,i}(P_{e,i} - P_i^{\text{ref}})$ and by rearranging, one retrieves the dynamics in (5.2). When $\tau_{P,i} > 0$, this coefficient emulates inertia and the droop control law emulates the swing equation (4.1) for synchronous generators.

Voltage droop control

Voltage regulation in power inverters is, unlike the frequency regulation in (5.3), typically not immediate. We model the lag through a filter with time constant $\tau_{V,i} \geq 0$, and the control law becomes:

$$\tau_{V_i}\dot{V}_i = -V_i + u_i^V. \tag{5.8}$$

The voltage droop controller is implemented as simple proportional control based on reactive power deviations:

$$u_i^V = V_i^{\text{ref}} - k_{Q_i}(\hat{Q}_i - Q_i^{\text{ref}}), \tag{5.9}$$

where V_i^{ref} and Q_i^{ref} are the respective setpoints for the voltage magnitude and reactive power, and $k_{Q_i} > 0$ is the *voltage droop coefficient*. $\hat{Q}_i$ is, just as in the case of active power above, the filtered reactive power, which is obtained by

$$\tau_{Q_i}\dot{\hat{Q}}_i = -\hat{Q}_i + Q_i, \tag{5.10}$$

where $\tau_{Q_i} > 0$ is a filter constant and Q_i are the actual reactive power injection to the network at node i. We can assume that the time constant for the voltage control, τ_{V_i} is small compared to τ_{Q_i}, so that it can be neglected [67]. We therefore set $\tau_{V_i} = 0$ in (5.8), and then by substituting (5.9) into (5.8), we obtain:

$$V_i = V_i^{\text{ref}} - k_{Q_i}(\hat{Q}_i - Q_i^{\text{ref}}). \tag{5.11}$$

Taking the derivative (5.11) with respect to time gives $\dot{V}_i = -k_{Q_i}\dot{\hat{Q}}_i$, in which we can insert the filter equation (5.10). We then substitute $\hat{Q}_i$ using (5.11) and obtain the control dynamics for voltages as:

$$\tau_{Q_i}\dot{V}_i = -V_i + V_i^{\text{ref}} - k_{Q_i}(Q_i - Q_i^{\text{ref}}). \tag{5.12}$$

Note that we will assume voltages to be fixed throughout the first part of this chapter, and only consider variable voltages in Section 5.3.

5.2 Performance of mixed-oscillator systems

Based on the model introduced in Section 5.1.1, we now derive a dynamical system model for a network consisting of both synchronous and asynchronous generators as well as dynamic loads. This model is preserving of network topology, in the sense that load buses are accounted for and are not absorbed into the network lines as in the Kron reduced network model used in Chapter 4. We will refer to this model as a mixed-oscillator system, since the synchronous generators are second-order oscillators and the frequency-dependent elements (dynamic loads and asynchronous generators) are, by some abuse of terminology, often referred to as *first-order oscillators.*

We formulate a linear dynamical system subject to distributed disturbances, and evaluate this system's performance through an input-output $\mathcal{H}_2$ norm as in Chapter 4. We show that, under certain assumptions, the performance of this mixed-oscillator system is equivalent to that of a system of second-order oscillators. We discuss implications of this result for renewable energy integrated power networks at the end of this chapter.

5.2.1 Representation of mixed-oscillator systems

In the mixed-oscillator model, we consider a power network with the underlying graph $\mathcal{G}_0 = (\mathcal{V}_0, \mathcal{E}_0)$, where $\mathcal{V}_0 := \{1, \ldots N_0\}$ is the set of nodes (buses) and $\mathcal{E}_0$ is a set of edges (lines). Let L_B^0 and L_G^0 be the corresponding susceptance and conductance matrices, as described in Section 2.3.2. Assume that each node $i \in \mathcal{V}_0$ contains a frequency dependent element (either a frequency-dependent load according to (5.1) or asynchronous power source according to (5.2)). Assume further that a subset $\mathcal{S}_0 \in \mathcal{V}_0$ of the buses also have synchronous generation, and let $|\mathcal{S}_0| = N_{\mathcal{S}} \leq N_0$.

Network augmentation

The network preserving model based on [10] is derived by augmenting the network as follows. Divide each generator bus $j \in \mathcal{S}_0$ into two separate buses; one containing the synchronous generator and one with the frequency dependent element, which we will for simplicity assume to be a load. Then connect the resulting two buses through a purely reactive line. This line represents the internal transient reactance of the synchronous generator. The entire system is now described by an augmented network with a total of $N = N_0 + N_{\mathcal{S}}$ nodes. We refer to the $N_{\mathcal{S}}$ synchronous generators nodes in this augmented network as "fictitious generator buses". Figure 5.1 illustrates this procedure for a sample network and gives an example of the respective node sets described next.

Without loss of generality the buses can be renumbered as follows. The buses in the set $\mathcal{V}_0 \backslash \mathcal{S}_0 := \mathcal{W}$, which are those *without* synchronous generation in the original network, are indexed as $\mathcal{W} = \{1, ..., N_0 - N_{\mathcal{S}}\}$. The (fictitious) synchronous generator buses are the nodes $\{N_0 + 1, ..., N_0 + N_{\mathcal{S}} = N\} =: \mathcal{S}$ and the new buses

with the frequency-dependent load elements that were in the set $\mathcal{S}_0$, are now in the set $\{N_0 - N_\mathcal{S} + 1, ..., N_0\} =: \mathcal{L}$. The nodes $i \in \mathcal{L}$ are numbered in increasing order with respect to the set $\mathcal{S}$. Furthermore, we denote the set of the $N_\mathcal{S}$ lossless lines used to augment the system as $\mathcal{E}_{\text{aug}}$. The graph that describes the augmented network can now be written as $\mathcal{G}_1 = (\mathcal{V}_1, \mathcal{E}_1)$, where $\mathcal{V}_1 := \mathcal{W} \cup \mathcal{S} \cup \mathcal{L}$ is the full set of nodes and $\mathcal{E}_1 := \mathcal{E}_0 \cup \mathcal{E}_{\text{aug}}$. We denote the susceptance and conductance matrices of the augmented network by L_B and L_G respectively. Each node in the augmented N-bus network has an associated voltage magnitude V_i and voltage phase angle θ_i. We next state the dynamics in θ_i for the nodes in these various node sets.

Remark 5.2 The system augmentation method outlined above assumes that each node $j \in \mathcal{S}_0$ has a frequency dependent load element as well as a synchronous generator. In other words, a non-zero dynamic load is co-located with every synchronous generator in the pre-augmented system. The load element could trivially be exchanged for a frequency-dependent power injection. The augmentation method can also easily be adapted to include isolated synchronous generators (possibly co-located with static loads). These nodes would then remain single synchronous generator buses as the system is augmented.

Mixed-oscillator system dynamics

The synchronous generators are, as in Chapter 4, governed by the swing equation (4.1), which we restate here as:

$$m_i \ddot{\theta} + d_i \dot{\theta} = P_{m,i}^0 - P_{e,i}, \quad i \in \mathcal{S}, \tag{5.13}$$

where m_i and d_i are the inertia and damping coefficients of the ith generator and $P_{m,i}^0$ is the constant mechanical power input from the generator turbine. $P_{e,i}$ is here, as well as for remaining nodes $i \in \mathcal{V}_1$, the real electrical power injection to the grid that was introduced in Section 4.2.2.

Recall that the dynamics at nodes $i \in \mathcal{L}$ are given by (5.1) and those at $i \in \mathcal{W}$ are given by (5.2). We can combine these with the swing equation (5.13), that holds for $i \in \mathcal{S}$, to compactly represent the dynamics at all nodes $i \in \mathcal{V}_1 = \mathcal{W} \cup \mathcal{S} \cup \mathcal{L}$ as follows:

$$m_i \ddot{\theta}_i + d_i \dot{\theta}_i + k_i \dot{\theta}_i = P_{m,i}^0 + P_{\text{wind},i}^0 - P_{\text{load},i}^0 - \sum_{j \in \mathcal{N}} b_{ij} \left[\theta_i - \theta_j \right], \quad i \in \mathcal{V}_1 \tag{5.14}$$

where we have also substituted the linearized power flow equation (4.3). For $i \in \mathcal{S}$ it holds $D_i = 0$, $M_i > 0$, $d_i > 0$, and $P_{m,i}^0 > 0$; for $i \in \mathcal{W}$ it holds $m_i = d_i = 0$, $k_i > 0$, and $P_{\text{wind},i}^0 > 0$; for $i \in \mathcal{L}$ it holds $m_i = d_i = 0$, $k_i > 0$ and $P_{\text{load},i}^0 > 0$.

We will carry out the entire analysis of the mixed oscillator system using a grounded network, as described in Section 4.4.1. Throughout, we will take N as the grounded node, which means that we set $\theta_N \equiv 0$ and measure all other
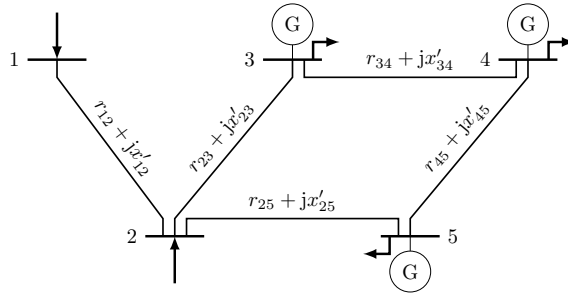
(a) Original network
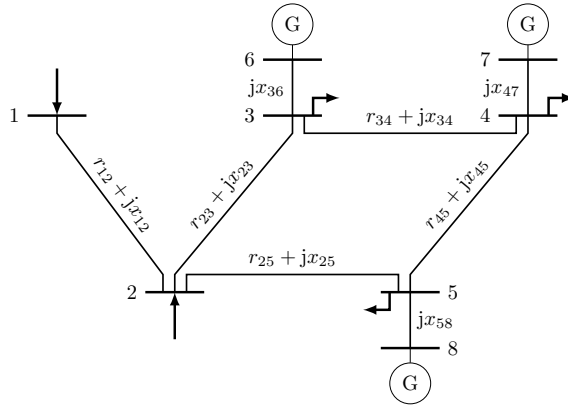
(b) Augmented network

Figure 5.1: An example of (a) a 5 bus network with 3 synchronous generators and (b) the corresponding augmented network, in which every joint generator and load bus is replaced by a separate load bus and a fictitious generator bus. Here, the respective sets of nodes are $\mathcal{W} = \{1, 2\}$, $\mathcal{S} = \{6, 7, 8\}$ and $\mathcal{L} = \{3, 4, 5\}$. The lines in $\mathcal{E}_{\mathrm{aug}} = \{e_{36}, \ e_{47}, \ e_{58}\}$ model the transient reactances of the generators. The arrows at buses 1 and 2 symbolize a power injection by an asynchronous generation source.

phase angles and frequency deviations in the system with respect to this reference. Physically, this corresponds to allowing node N to behave as an infinite bus.

In order to rewrite the dynamics on matrix form we first define $K = \text{diag}\{k_j\}$ for buses $j \in \mathcal{W} \cup \mathcal{L}$, and $M = \text{diag}\{m_i\}$, $D = \text{diag}\{d_i\}$ for buses $i \in \mathcal{S}$. Let L_B be the susceptance matrix of the augmented network $\mathcal{G}_1$, and $\tilde{L}_B$ be the corresponding grounded version (again, see Section 4.4.1). We then write the dynamics from (5.14) on matrix form as

$$K\omega_K \quad = \quad - \begin{bmatrix} I_{N_0} & 0 \end{bmatrix} (\tilde{L}_B\theta - P^0) \tag{5.15}$$

$$M\dot{\omega}_G + D\omega_G \quad = \quad - \begin{bmatrix} 0 & I_{(N_S-1)} \end{bmatrix} (\tilde{L}_B\theta - P^0), \tag{5.16}$$

where $P^0 = \text{diag}\{P_i^0\}$, letting $P_i^0 = P_{m,i}^0 + P_{\text{wind},i}^0 - P_{\text{load},i}^0$. The state vectors are defined so that $\theta = \begin{bmatrix} \theta_1 & \cdots & \theta_{N-1} \end{bmatrix}^T$ and

$$\dot{\theta} = \begin{bmatrix} I_{N_0} \\ 0 \end{bmatrix} \omega_K + \begin{bmatrix} 0 \\ I_{(N_S-1)} \end{bmatrix} \omega_G = T_1\omega_K + T_2\omega_G. \tag{5.17}$$

Filling (5.15) into (5.17) allows the state ω_K to be eliminated using

$$T_1\omega_K = -T_1 K^{-1} T_1^T (\tilde{L}_B\theta - P^0).$$

To simplify the notation, we define $T_K := T_1 K^{-1} T_1^T$ and write the state equations for the combined system as

$$\frac{\mathrm{d}}{\mathrm{d}t} \begin{bmatrix} \theta \\ \omega_G \end{bmatrix} = \begin{bmatrix} -T_K\tilde{L}_B & T_2 \\ -M^{-1}T_2^T\tilde{L}_B & -M^{-1}D \end{bmatrix} \begin{bmatrix} \theta \\ \omega_G \end{bmatrix} + \begin{bmatrix} T_K \\ M^{-1}T_2^T \end{bmatrix} w, \tag{5.18}$$

where w is the disturbance input. By some abuse of notation, we have used the same approach as in Chapter 4 and let the system (5.18) represent deviations from a steady-state operating point as given by the constant P^0.

Performance output

As before, we study system performance by investigating the resistive losses that arise due to the power flows required to return to a synchronous state after a disturbance. We therefore use the performance metric from Definition 4.1. Here, we have already assumed that node N is grounded and can therefore use the following $(N-1)$-dimensional performance output for the system (5.18):

$$y = \begin{bmatrix} \tilde{L}_G^{1/2} & 0 \end{bmatrix} \begin{bmatrix} \theta \\ \omega_G \end{bmatrix}. \tag{5.19}$$

This allows the squared output norm $y * y$ to represent the total instantaneous losses over all lines $e_{ij} \in \mathcal{E}_1$. Since $\tilde{L}_G$ is a positive semidefinite grounded graph Laplacian, we have taken $\tilde{L}_G^{1/2}$ as the unique positive semidefinite matrix square root.

Recall that the lines $e_{ij} \in \mathcal{E}_{\mathrm{aug}}$ connecting the buses in $\mathcal{L}$ with those of $\mathcal{S}$ in the augmented network are purely reactive. This means that $g_{ij} = 0$ for $e_{ij} \in \mathcal{E}_{\mathrm{aug}}$, meaning that no real power flows over those lines and they induce no losses that are accounted for by the performance output (5.19).

We can now define the system (5.18) and (5.19) as the input-output mapping H from w to y as

$$\frac{\mathrm{d}}{\mathrm{d}t} \begin{bmatrix} \theta \\ \omega_G \end{bmatrix} = \begin{bmatrix} -T_K \tilde{L}_B & T_2 \\ -M^{-1} T_2^T \tilde{L}_B & -M^{-1} D \end{bmatrix} \begin{bmatrix} \theta \\ \omega_G \end{bmatrix} + \begin{bmatrix} T_K \\ M^{-1} T_2^T \end{bmatrix} w =: \mathcal{A}\psi + \mathcal{B}w \quad (5.20a)$$

$$y = \begin{bmatrix} \tilde{L}_G^{1/2} & 0 \end{bmatrix} \begin{bmatrix} \theta \\ \omega_G \end{bmatrix} =: \mathcal{C}\psi, \quad (5.20b)$$

where $\psi = [\theta, \omega_G]^T$.

5.2.2   Input-output analysis

In this section, we first show that the linear system (5.20) is asymptotically stable in order to ensure that its $\mathcal{H}_2$ norm is finite. We then derive an expression for this norm and discuss bounds on its value. Following that, we relate this norm to the results in Chapter 4.

Stability

We show that the system 5.20 is asymptotically stable using the following lemma, whose proof follows the arguments in [10].

Lemma 5.1 *The system* (5.20) *is asymptotically stable and the following is a Lyapunov function for* (5.20a)

$$V(\theta, \omega_G) = \tfrac{1}{2}\theta^T \tilde{L}_B \theta + \tfrac{1}{2}\omega_G^T M \omega_G.$$

Proof: Clearly, $V(0,0) = 0$. It holds that $M > 0$ by definition. $\tilde{L}_B$ is positive definite, since it is a reduced Laplacian of a connected graph [52]. Therefore, $V(\theta, \omega_G) > 0, \quad \forall \theta, \omega_G \neq (0,0)$. The derivative of V evaluated along the state trajectories can, after some algebraic operations, be given as

$$\dot{V}(\theta, \omega_G) = -\omega_G^T D \omega_G - \theta^T \tilde{L}_B T_K^T \tilde{L}_B \theta,$$

which is non-positive for all θ, ω_G, since $D > 0$ and $\tilde{L}_B T_K^T \tilde{L}_B \geq 0$. For asymptotic stability, we also require $\dot{V}(\theta, \omega_G) = 0 \iff (\theta, \omega_G) = (0,0)$ by LaSalle's invariance principle. Clearly, $\dot{V} = 0$ requires $\omega_G = 0$ and $T_K^T \tilde{L}_B \theta = 0$. The latter is equivalent to $T_1^T \tilde{L}_B \theta = 0$. By (5.18), however, $\omega_G = 0$ implies $-M^{-1} T_2^T \tilde{L}_B \theta = 0$. Now, if we

let $T = \begin{bmatrix} T_1 & T_2 \end{bmatrix} = I_{(N_0 + N_S - 1)}$, the two give $T\tilde{L}_B\theta = 0$. Since T is the identity matrix and $\tilde{L}_B$ is positive definite, it must hold $\theta = 0$. We therefore conclude that the last criterion holds and all Lyapunov's conditions for global asymptotic stability are fulfilled.

$\blacksquare$

$\mathcal{H}_2$ norm calculations

As in the previous chapter, the $\mathcal{H}_2$ norm of the system H in (5.20) is computed using the equations (2.7) – (2.8). Here, we partition $X \in \mathbb{C}^{(N+N_S-2)\times(N+N_S-2)}$ into four submatrices as

$$X = \begin{bmatrix} X_1 & X_0 \\ X_0^* & X_2 \end{bmatrix}$$

where $X_1 \in \mathbb{C}^{(N-1)\times(N-1)}$, $X_0 \in \mathbb{C}^{(N-1)\times(N_S-1)}$ and $X_2 \in \mathbb{C}^{(N_S-1)\times(N_S-1)}$. The Lyapunov equation reduces to the following three linearly independent equations

$$\tilde{L}_B T_K X_1 + \tilde{L}_B T_2 M^{-1} X_0^* + X_1 T_K \tilde{L}_B + X_0 M^{-1} T_2^T \tilde{L}_B = \tilde{L}_G \tag{5.21a}$$

$$\tilde{L}_B T_K X^0 - \tilde{L}_B T_2 M^{-1} X_2 + X_1 T_2 - X_0 M^{-1} D = 0 \tag{5.21b}$$

$$T_2^T X_0 - M^{-1} D X_2 + X_0^* T_2 - X_2 M^{-1} D = 0. \tag{5.21c}$$

Using these equations, the norm from (2.7) becomes

$$||H||_2^2 = \text{tr}(\mathcal{B}^* X \mathcal{B}) = \text{tr}(T_K^2 X_1) + \text{tr}(M^{-2} X_2). \tag{5.22}$$

For tractability purposes, we now impose Assumption 4.1 of uniform synchronous generators, as well as the following assumption:

Assumption 5.1 (Identical asynchronous machines) All frequency dependent elements given by (5.1) and (5.2) have identical coefficients k_i, that is, $k_i = k$ for all $i \in \mathcal{L} \cup \mathcal{S}$. This gives $K = kI$, where I is the $N_0 \times N_0$ identity matrix.

Under these assumptions, (5.22) can be simplified to:

$$||H||_2^2 = \frac{1}{2k}\text{tr}(\tilde{L}_B^{-1}\tilde{L}_G) + \left(1 - \frac{d}{k}\right)\frac{1}{m^2}\text{tr}(X_2), \tag{5.23}$$

where X_2 can be evaluated using equations (5.21a) – (5.21c). According to the discussion in Section 4.3.1, this expression represents the expected power losses due to certain disturbance inputs w.

Generalized Laplacian ratios in the augmented network

In order to understand the losses described in the expression (5.23), it is useful to first examine the properties of the generalized graph Laplacian ratio $\text{tr}(\tilde{L}_B^{-1}\tilde{L}_G)$ in the case where the underlying graph is that of an augmented network. To facilitate

this discussion, recall Lemma 4.3, which says that $\mathrm{tr}(\tilde{L}_B^{-1}\tilde{L}_G) = \mathrm{tr}(L_B^\dagger L_G)$ for any two graph Laplacians L_B and L_G. This result extends to the augmented system, since L_B and L_G are both weighted graph Laplacians for the augmented system, even though the graph underlying L_G is no longer connected. We will use Lemma 4.3 to prove the theorem stated in this section.

We already discussed that the expression $\mathrm{tr}(\tilde{L}_B^{-1}\tilde{L}_G)$ can be thought of as a generalized ratio of susceptance to conductance in a general graph. This notion is further strengthened by the following result, which shows that for our augmented network, the purely reactive edges in $\mathcal{E}_{\mathrm{aug}}$ do not contribute to the generalized Laplacian ratio. In other words, only the main network, whose underlying graph is $\mathcal{G}_0$ (with vertex set $\mathcal{L} \cup \mathcal{W}$) will influence the generalized graph Laplacian ratio and the augmented, fictitious nodes will be irrelevant. This idea is formalized through the following theorem.

Theorem 5.2 *Let the graph $\mathcal{G}_0$ describe a power network, and let $\mathcal{G}_1$ denote the corresponding augmented network, using the method described in Section 5.2.1. Let the susceptance and conductance matrices associated with $\mathcal{G}_0$ be, respectively, L_B^0 and L_G^0 and those associated with the augmented network $\mathcal{G}$ be L_B and L_G. Furthermore, let $\tilde{L}_B$ and $\tilde{L}_G$ be the grounded versions of L_B and L_G. It then holds that*

$$\mathrm{tr}(\tilde{L}_B^{-1}\tilde{L}_G) = \mathrm{tr}(L_B^\dagger L_G) = \mathrm{tr}(L_B^{0\dagger}L_G^0).$$

Proof: See Appendix.

∎

The fact that only the main, unaugmented, network affects the generalized Laplacian ratio can be seen more clearly in the special case when the conductance to susceptance ratios α_{ij} of all lines (edges) are equal:

Corollary 5.3 *Consider the network described in Theorem 5.2. Let all edges $e_{ij} \in \mathcal{E}_0$ have equal resistance-to-reactance ratios, that is $\alpha_{ij} = \frac{r_{ij}}{x_{ij}} = \frac{g_{ij}}{b_{ij}} = \alpha$ Then*

$$\mathrm{tr}(\tilde{L}_B^{-1}\tilde{L}_G) = \alpha(N_0 - 1). \tag{5.24}$$

Proof: In this case, $L_G^0 = \alpha L_B^0$. By Theorem 5.2 and Lemma 4.3: $\mathrm{tr}(\tilde{L}_B^{-1}\tilde{L}_G) = \mathrm{tr}(L_B^{0\dagger}L_G^0) = \mathrm{tr}((\tilde{L}_B^0)^{-1}\tilde{L}_G^0) = \mathrm{tr}((\tilde{L}_B^0)^{-1}\alpha\tilde{L}_B^0) = \mathrm{tr}(\alpha I_{(N_0-1)}) = \alpha(N_0 - 1)$.

∎

Remark 5.3 Note that Theorem 5.2 and Corollary 5.3 allow for the synchronous generators' transient reactances x_{ij} for $e_{ij} \in \mathcal{E}_{\mathrm{aug}}$ to take any value.

5.2.3   Performance analysis for mixed-oscillator system

We now relate the $\mathcal{H}_2$ norm of the mixed-oscillator system (5.20) to our earlier results for synchronous generator systems from Chapter 4, as well as to the special case where the system consists of only first-order dynamics. As we will show, all of these systems have the same associated $\mathcal{H}_2$ norm, provided that their dampings are equal. We also discuss some interesting implications of this result.

$\mathcal{H}_2$ norm bound

From (5.23), it is clear that when $d = k$, the $\mathcal{H}_2$ norm of the system (5.20) reduces to $||H||_2^2 = \frac{1}{2k}\mathrm{tr}(\tilde{L}_B^{-1}\tilde{L}_G)$, which by Theorem 5.2 gives:

$$||H||_2^2 = \frac{1}{2k}\mathrm{tr}(L_B^{0\dagger}L_G^0). \tag{5.25}$$

The frequency dependence coefficient k in (5.1) and (5.2) can be seen as a type of damping, analogous to the dampings d of the synchronous generators. However, wind power plants and loads generally have much lighter rotors than synchronous generators. It is thus reasonable to assume that $d \geq k$ which leads to the following upper bound on (5.23):

$$||H||_2^2 \leq \frac{1}{2k}\mathrm{tr}(L_B^{0\dagger}L_G^0). \tag{5.26}$$

Even in the general case of non-uniform asynchronous dampings, a choice of $k = \min_{i\in\mathcal{W}\cup\mathcal{L}} k_i = k_{\min}$ makes this bound conservative.

Special case: first-order dynamics

An interesting special case is when $\mathcal{S}_0 = \emptyset$, which corresponds to a system without synchronous generation, or equivalently, a network of only first-order oscillators in our modeling framework. Such a model arises for example when studying inverter-based microgrids in the limit where there are no time-delays in the dynamics (see Section 5.1.2) and it is therefore highly relevant to ongoing related research, see for example [72, 73].

Under Assumption 5.1, the reduced input-output system, denoted $\tilde{H}_{1^{st}}$, for this special case becomes:

$$\begin{aligned} \frac{\mathrm{d}}{\mathrm{d}t}\tilde{\theta} &= -\frac{1}{k}\tilde{L}_B^0\tilde{\theta} + \frac{1}{k}I\tilde{w} \\ \tilde{y} &= (\tilde{L}_G^0)^{1/2}\tilde{\theta}, \end{aligned} \tag{5.27}$$

where we have taken node $N = N_0$ as the grounded node and $\tilde{\theta}$ is the corresponding reduced state vector. It is now easy to show that

$$||\tilde{H}_{1^{st}}||_2^2 = \frac{1}{2k}\mathrm{tr}((\tilde{L}_B^0)^{-1}\tilde{L}_G^0) = \frac{1}{2k}\mathrm{tr}(L_B^{0\dagger}L_G^0),$$

which is precisely the result in (5.25). We remark that this result holds regardless of whether one considers a grounded system or not.

Comparison of oscillator models

Not only the first-order model is equivalent to the mixed-order oscillator model in terms of the input-output $\mathcal{H}_2$ norm. By considering the parameter k as a surrogate for the damping coefficient d, the norm in (5.25) is also the norm of a system with N_0 synchronous generators, as we showed by Theorem 4.4. In the current modeling framework, the system (5.20) becomes such a system of N_0 synchronous generators if $\mathcal{S}_0 = \mathcal{V}_0$, but the nodes are not augmented, see Remark 5.2.

More interestingly, the main result of this section shows that the same $\mathcal{H}_2$ norm holds for a network where all nodes $i \in \mathcal{V}_0$ have a first-order oscillator with damping k and where the $N_\mathcal{S}$ nodes in the set $\mathcal{S}_0 \subset \mathcal{V}_0$ *in addition* have a synchronous generator with damping $d = k$. This means that the $N_\mathcal{S}$ nodes that have now been added, compared to the first-order system in (5.27), do not change the input output norm, even though they do change the dynamics.

We can conclude that if damping parameters $k = d$ are uniform, the $\mathcal{H}_2$ norm and therefore the resistive losses are the same, regardless of whether the first-order (5.27) model, a second-order model (4.9) or a combined model (5.20) is used. Any differences in performance between these models can therefore be attributed to the parameters that characterize the different types of generators. Therefore, from the perspective of the "price of synchrony" performance measure, the order of the dynamics used to characterize the power network is irrelevant.

We should point out that these results do not claim the models to be equivalent, and do not address any transient stability properties of the power system. The transient responses of the respective systems are substantially different and when studying synchronous stability of power systems in general, the model order and parameters should be chosen with care. The losses incurred in a synchronizing network and the network's ability to synchronize are two different issues, and it is only in terms of the $\mathcal{H}_2$ norm with respect to the selected performance output, that we claim the different order models to be equivalent.

5.3 Microgrids with variable voltage dynamics

We now shift focus to a different type of renewable energy integrated power network and consider a model of an inverter-based microgrid. The dynamics in such microgrids is assumed to be governed by controllable power electronics, for which we will impose the control laws introduced in Section 5.1.2. Unlike our previous analyses, we now account for variable voltages and non-zero resistances in the system dynamics. This means that we also need to account for the full complex power flow, and that the performance measure from Definition 4.1 needs to be extended to include the power losses that arise due to voltage fluctuations.

This section's main result shows that under the assumption of uniform inverter parameters and resistance-to-reactance ratios in the network, the power losses can be decomposed into two parts; one associated with frequency control which is identical to the result in Chapter 4, and an additional part associated with voltage

control. In addition to these two parts of the norm, there are cross-terms associated with the cross-couplings of frequency and voltage dynamics. We demonstrate, however, that these terms are typically small with respect to the overall power losses.

Interestingly, we also find that the power losses associated with voltage control depends strongly on network topology, unlike the losses associated with frequency control that we have derived previously. In fact, these losses will be larger in a highly interconnected network than in a sparsely interconnected one. We discuss interpretations of this result as well as expressions and bounds for performance in various network topologies.

5.3.1   Dynamic model of inverter-based microgrid

As before, we consider a network $\mathcal{G} = \{\mathcal{V}, \mathcal{E}\}$ with the set of nodes $\mathcal{V} = \{1, \ldots, N\}$ and a set of edges, or network lines, $\mathcal{E} = \{e_{ik}\}$. We assume that all constant impedance loads have been absorbed into the network lines and that, consequently, every node $i \in \mathcal{V}$ represents a generation unit with a power inverter as its grid interface. That is, we again consider a Kron reduced network as in Chapter 4[1]. Each node has an associated phase angle θ_i and voltage magnitude V_i.

We introduced the inverter model and droop control laws in Section 5.1.2. In summary, the control dynamics for phase angles θ_i and voltage magnitudes V_i are:

$$
\begin{aligned}
\dot{\theta}_i &= \omega_i \\
\tau_{P_i} \dot{\omega}_i &= -\omega_i + \omega^{\mathrm{ref}} - k_{P_i}(P_{e,i} - P_i^{\mathrm{ref}}) \\
\tau_{Q_i} \dot{V}_i &= -V_i + V_i^{\mathrm{ref}} - k_{Q_i}(Q_i - Q_i^{\mathrm{ref}}).
\end{aligned}
\tag{5.28}
$$

We now derive the linearized equations for the power injections $P_{e,i}$ and Q_i. The equation for $P_{e,i}$ will differ from the one derived in Section 4.2.2, since we no longer assume a uniform voltage profile.

Linearized complex power flows

Introducing $\theta_{ik} = (\theta_i - \theta_k)$ as the phase angle difference between neighboring nodes, the active and reactive powers injected to the grid at node $i \in \mathcal{V}$ are given by

$$
P_{e,i} = -g_{ii}V_i^2 + \sum_{k \in \mathcal{N}_i} V_i V_k (g_{ik}\cos\theta_{ik} + b_{ik}\sin\theta_{ik})
\tag{5.29}
$$

$$
Q_i = b_{ii}V_i^2 + \sum_{k \in \mathcal{N}_i} V_i V_k (g_{ik}\sin\theta_{ik} - b_{ik}\cos\theta_{ik}).
\tag{5.30}
$$

---

[1]In line with the previous section, dynamic loads could be accounted for using an network-preserving model. In order to make the analysis as tractable as possible and to isolate the effect of variable voltages for performance, we limit the analysis here to a Kron reduced inverter-based network.

Where $\mathcal{N}_i$ denotes the neighbor set of node i, and, as before g_{ik} is the conductance and b_{ik} the susceptance of the line e_{ik}. At each node i, $g_{ii} = \bar{g}_i + \sum_{k \in \mathcal{N}_i} g_{ik}$ and $b_{ii} = \bar{b}_i + \sum_{k \in \mathcal{N}_i} b_{ik}$ represent the respective self-conductance and self-susceptance, which include the shunts $\bar{b}_i$ and $\bar{g}_i$. We will in the following make the common assumption [35, 68] that the shunt elements are purely inductive, so that in our notation $\bar{g}_i = 0$ and $\bar{b} \geq 0$ for all $i \in \mathcal{V}$.

We will be considering systems under the assumption of small deviations from an operating point. We can therefore approximate the power flows by a linearization around the points $P_i^0(\theta_{ik}^0, V_i^0, V_k^0)$ and $Q_i^0(\theta_{ik}^0, V_i^0, V_k^0)$, where $V_i^0 = V_k^0 = V^0 = 1$ and $\theta_{ik} = 0$ for all $i, k \in \mathcal{N}$. This procedure gives the linearized power injections at node i as:

$$\Delta P_{e,i} = \sum_{k \sim i} \left(-g_{ik}(\Delta V_i - \Delta V_k) + b_{ik}\Delta\theta_{ik} \right) \tag{5.31}$$

$$\Delta Q_i = 2\bar{b}_i \Delta V_i + \sum_{k \sim i} \left(b_{ik}(\Delta V_i - \Delta V_k) + g_{ik}\Delta\theta_{ik} \right). \tag{5.32}$$

Note that, under the assumption of a uniform voltage profile, (5.31) reduces to (4.3).

Formulation of closed loop system

We now formulate the inverter dynamics as a closed loop linear system subject to distributed disturbances that represent fluctuations in generation and loads. For this purpose, we let the operating point around which the power flow equations are linearized be given by the setpoints from the droop control laws in (5.28), so that $\Delta P_{e,i} = P_{e,i} - P_i^{\text{ref}}$ and $\Delta Q_i = Q_i - Q_i^{\text{ref}}$ for all $i \in \mathcal{V}$. In an effort to avoid cumbersome notation, we then omit the difference operator Δ and let the state variables $(\theta_{ik}, \omega_i, V_i)$ represent deviations from the operating point. As before, we assume additive process noise through the disturbance input w.

We can then use the power flow equations (5.31) – (5.32) to express the dynamics (5.28) of the ith inverter as:

$$\dot{\theta}_i = \omega_i$$
$$\tau_{P_i}\dot{\omega}_i = -\omega_i - k_{P_i}\left(-\sum_{k \sim i} g_{ik}(V_i - V_k) + \sum_{k \sim i} b_{ik}\theta_{ik} \right) + w_i^\omega$$
$$\tau_{Q_i}\dot{V}_i = -V_i - k_{Q_i}\left(2\bar{b}_i V_i + \sum_{k \sim i} b_{ik}(V_i - V_k) + \sum_{k \sim i} g_{ik}\theta_{ik} \right) + w_i^V.$$

Now, by defining θ, ω, V as column vectors containing the states θ_i, ω_i, V_i, $i \in \mathcal{V}$ and using the susceptance and conductance matrices L_B and L_G defined in (2.19),

we can summarize the above dynamics as follows:

$$
\begin{bmatrix} \dot{\theta} \\ \dot{\omega} \\ \dot{V} \end{bmatrix} = \begin{bmatrix} 0 & I & 0 \\ -K_P T_P^{-1} L_B & -T_P^{-1} & K_P T_P^{-1} L_G \\ -K_Q T_Q^{-1} L_G & 0 & -C_Q T_Q^{-1} - K_Q T_Q^{-1} L_B \end{bmatrix} \begin{bmatrix} \theta \\ \omega \\ V \end{bmatrix}
$$
$$
+ \begin{bmatrix} 0 & 0 \\ T_P^{-1} & 0 \\ 0 & T_Q^{-1} \end{bmatrix} w, \quad (5.33)
$$

where $w = [w_i^\omega, \ w_i^V]^T$ represents the disturbance input. We have also introduced $C_Q = \operatorname{diag}\{c_{Q_i}\}$ with $c_{Q_i} = 1 + 2k_{Q_i}\bar{b}_i$. The remaining system parameters are given by $K_{P(Q)} = \operatorname{diag}\{k_{P(Q)_i}\}$, $T_{P(Q)} = \operatorname{diag}\{\tau_{P(Q)_i}\}$.

5.3.2   Performance measure with variable voltages

We now extend the "price of synchrony" performance measure introduced in Section 4.3 to also account for losses associated with fluctuating voltages. For this purpose, consider again the real power loss over an edge e_{ik}, which is given by Ohm's law as

$$
P_{ik}^{\text{loss}} = g_{ik}|v_i - v_k|^2, \tag{5.34}
$$

where v_i, v_k are the complex voltages at nodes i and k. We can now enforce the common linearized system assumption of small phase angle differences. Standard trigonometric methods then give that $|v_i - v_k|^2 \approx (V_i - V_k)^2 + (V_i(\theta_i - \theta_k))^2$. Since we also assume $V_i \approx 1$ p.u. around the linearization point for all $i \in \mathcal{V}$, an approximation of the power loss over the edge e_{ik} is $P_{ik}^{\text{loss}} = g_{ik}\left[(V_i - V_k)^2 + (\theta_i - \theta_k)^2\right]$. The total instantaneous power losses over the network are then approximately

$$
\mathbf{P}_{\text{loss}} \approx \sum_{i \sim k} g_{ik} \left[(V_i - V_k)^2 + (\theta_i - \theta_k)^2\right]. \tag{5.35}
$$

Making use of the conductance matrix L_G, we can write (5.35) as the quadratic form

$$
\mathbf{P}_{\text{loss}} = V^T L_G V + \theta^T L_G \theta, \tag{5.36}
$$

which allows us to make the following definition:

Definition 5.1 (Price of synchrony performance output with variable voltages)
The instantaneous resistive power losses in a power network with variable voltages are measured as $\mathbf{P}_{loss} = y^* y$, where the performance output y is

$$
y := L_G^{1/2}\theta + L_G^{1/2}V. \tag{5.37}
$$

Here V and θ are the state vectors that were defined in the previous section.

5.3.3 Performance analysis of decoupled microgrid dynamics

In this section, we analyze the dominant performance of (5.33) with respect to the output (5.37), by assuming that the network's resistances are small compared to its reactances. Under this common assumption (see for example [33, 67, 73]), the active power flow is a function only of the phase angles and the reactive power flow is a function only of the voltage magnitudes, that is,

$$P(\theta, V) \approx P(\theta), \quad Q(\theta, V) \approx Q(V).$$

This leads to a decoupling of the frequency and voltage dynamics and we obtain $L_G = 0$ in the system matrix of (5.33). The output (5.37) then measures the power losses associated with the trajectories arising from these decoupled dynamics by retaining the non-zero resistances through L_G.

In Section 5.3.4, we relax this assumption of decoupled power flows, and show that the results derived here are robust towards that relaxation, provided resistances remain sufficiently small. In particular, the errors made by evaluating the performance under decoupled (lossless) dynamics will be small in relation to the overall performance of the network.

Remark 5.4 The assumption of small resistances compared to reactances is not, in general, applicable to low to medium voltage grids [42]. However, it is not unreasonable for an inverter-based network, given that inverter output impedances are typically highly inductive [68]. When these impedances are absorbed into the network through the Kron reduction they may therefore dominate the line resistances.

In the subsequent derivations we make the following further assumptions:

Assumption 5.2 (Identical inverters) All inverters have identical droop control settings and low-pass filters for power measurement, i.e., $K_P = \text{diag}\{k_P\}$, $K_Q = \text{diag}\{k_Q\}$, $T_P = \text{diag}\{\tau_P\}$, $T_Q = \text{diag}\{\tau_Q\}$.

Assumption 5.3 (Uniform shunt conductances) All nodes have identical shunt conductances, i.e., $\bar{b}_i = \bar{b} \geq 0$ and $C_Q = \text{diag}\{c_Q\}$.

Assumption 5.4 (Uniform resistance-to-reactance ratios) The ratio of resistances to reactances, equivalently conductances to susceptances, of all lines are uniform and constant, i.e.,

$$\alpha := \frac{g_{ik}}{b_{ik}},$$

for all $e_{ik} \in \mathcal{E}$. This implies $L_G = \alpha L_B$.

Assumption 5.4, which is also applied in e.g. [48], [23], can be motivated first by uniformity in the physical line properties in a microgrid (i.e., materials and dimensions). Second, Kron reduction of a network increases its uniformity in node degrees [53]. This makes the line properties more uniform than in actual power networks. See also Section 4.4.3.

For ease of reference, we now re-state the system (5.33) with the output (5.37) under Assumptions 5.2 – 5.4 as the multiple-input multiple-output (MIMO) LTI system H:

$$
\begin{bmatrix} \dot{\theta} \\ \dot{\omega} \\ \dot{V} \end{bmatrix} = \begin{bmatrix} 0 & I & 0 \\ -\frac{k_P}{\tau_P} L_B & -\frac{1}{\tau_P} I & 0 \\ 0 & 0 & -\frac{c_Q}{\tau_Q} I - \frac{k_Q}{\tau_Q} L_B \end{bmatrix} \begin{bmatrix} \theta \\ \omega \\ V \end{bmatrix} + \begin{bmatrix} 0 & 0 \\ \frac{1}{\tau_P} I & 0 \\ 0 & \frac{1}{\tau_Q} I \end{bmatrix} w =: \mathcal{A}\psi + \mathcal{B}w,
$$

(5.38a)

$$
y = \begin{bmatrix} \sqrt{\alpha} L_B^{1/2} & 0 & 0 \\ 0 & 0 & \sqrt{\alpha} L_B^{1/2} \end{bmatrix} \begin{bmatrix} \theta \\ \omega \\ V \end{bmatrix} =: \mathcal{C}\psi.
$$

(5.38b)

Now, we will first show that the system (5.38) is input-output stable in order to ensure that its $\mathcal{H}_2$ norm is finite. We then proceed to derive an expression for this norm and to state its value for specific network topologies.

Eigenvalues and stability

Like the systems we have studies so far, the system (5.38) inherits the zero eigenvalue from the graph Laplacian L_B. The associated mode, which corresponds to the drift of the mean phase angle, is however unobservable also in this system, as we will show by a simple state transformation in the following section. Remaining eigenvalues of (5.38) are however strictly in the left half of the complex plane. Denote by λ_n^B the nth eigenvalue of L_B and without loss of generality number the eigenvalues so that $\lambda_1^B = 0$ and consider the following lemma:

Lemma 5.4   *If the graph underlying the network $\mathcal{G}$ is connected, then the eigenvalues of the system* (5.38a) *are:*

$$
\sigma(\mathcal{A}) = \left\{ 0, -\frac{1}{2\tau_P} \left(1 \pm \sqrt{1 - k_P \tau_P \lambda_n^B} \right), -\frac{1}{\tau_P}, -\frac{c_Q}{\tau_Q}, -\frac{c_Q}{\tau_Q} - \frac{k_Q}{\tau_Q} \lambda_n^B \right\},
$$

for $n = \{2, \ldots, N\}$. If the parameters $k_P, \tau_P, k_Q, \tau_Q > 0$ and the shunt susceptance satisfies $\bar{b} > \frac{-1}{2k_Q} \Leftrightarrow c_Q > 0$, all eigenvalues apart from $\lambda_1 = 0$ lie strictly in the left half of the complex plane and $\mathcal{A}$ is a stable matrix.

Proof: The eigenvalues are given by $\mathcal{A}$'s characteristic polynomial. Since the graph underlying L_B is connected, L_B is Hermitian positive semi-definite and $0 = \lambda_1^B < \lambda_2^B \leq \ldots \leq \lambda_N^B$. It is then easy to see that if $k_P, \tau_P, k_Q, \tau_Q, c_Q > 0$, all eigenvalues have negative real parts.

∎

Using this result we conclude that the system (5.38) is input-output stable and that its $\mathcal{H}_2$ norm is finite.

$\mathcal{H}_2$ norm calculation

To derive the $\mathcal{H}_2$ norm of (5.38), we follow the approach introduced in Section 2.1.2 and use the following unitary state transformation:

$$\begin{bmatrix} \theta \\ \omega \\ V \end{bmatrix} =: \begin{bmatrix} U & 0 & 0 \\ 0 & U & 0 \\ 0 & 0 & U \end{bmatrix} \begin{bmatrix} \hat{\theta} \\ \hat{\omega} \\ \hat{V} \end{bmatrix}, \qquad (5.39)$$

where U is the unitary matrix which diagonalizes L_B, i.e., $L_B = U^* \Lambda_B U$ with $\Lambda_B = \text{diag}\{\lambda_1^B, \lambda_2^B, \ldots, \lambda_N^B\}$. Given that the $\mathcal{H}_2$ norm is unitarily invariant, we can also apply transformations to the input and the output, so that

$$\hat{y} = \begin{bmatrix} U^* & 0 \\ 0 & U^* \end{bmatrix} y, \quad \text{and} \quad \hat{w} = \begin{bmatrix} U^* & 0 \\ 0 & U^* \end{bmatrix} w.$$

Through these transformations, we obtain a system $\hat{H}$ in which all blocks of the system (5.38) have been diagonalized. This system thus represents N decoupled subsystems, each of which we denote $\hat{H}_n$:

$$\begin{bmatrix} \dot{\hat{\theta}}_n \\ \dot{\hat{\omega}}_n \\ \dot{\hat{V}}_n \end{bmatrix} = \begin{bmatrix} 0 & 1 & 0 \\ -\frac{k_P}{\tau_P}\lambda_n^B & -\frac{1}{\tau_P} & 0 \\ 0 & 0 & -\frac{c_Q}{\tau_Q} - \frac{k_Q}{\tau_Q}\lambda_n^B \end{bmatrix} \begin{bmatrix} \hat{\theta}_n \\ \hat{\omega}_n \\ \hat{V}_n \end{bmatrix} + \begin{bmatrix} 0 & 0 \\ \frac{1}{\tau_P} & 0 \\ 0 & \frac{1}{\tau_Q} \end{bmatrix} \hat{w}_n =: \mathcal{A}_n \hat{\Psi}_n + \mathcal{B}_n \hat{w}_n,$$

$$\hat{y}_n = \sqrt{\alpha \lambda_n^B} \begin{bmatrix} 1 & 0 & 0 \\ 0 & 0 & 1 \end{bmatrix} \begin{bmatrix} \hat{\theta}_n \\ \hat{\omega}_n \\ \hat{V}_n \end{bmatrix} =: \mathcal{C}_n \hat{\Psi}_n,$$

and the $\mathcal{H}_2$ norm of the system $\hat{H}$ will be given as

$$||\hat{H}||_2^2 = \sum_{n=1}^N ||\hat{H}_n||_2^2 = ||H||_2^2.$$

Notice that the subsystem $\hat{H}_1$ corresponding to $\lambda_1 = 0$ has the the output $\hat{y}_1 = 0\hat{\psi}$. It is therefore unobservable and has $||\hat{H}_1||_2^2 = 0$.

The remaining subsystems' $\mathcal{H}_2$ norms are obtained by calculating their observability Gramians $X_n \in \mathbb{C}^{3 \times 3}$ from the Lyapunov equation

$$\mathcal{A}^* X_n + X_n \mathcal{A}_n = -\mathcal{C}_n^* \mathcal{C}_n. \qquad (5.40)$$

We then have that $||\hat{H}_n||_2^2 = \text{tr}\{\mathcal{B}_n^* X_n \mathcal{B}_n\} = \frac{1}{\tau_P^2} X_{n22} + \frac{1}{\tau_Q^2} X_{n33}$. Since the expansion of (5.40) is not very insightful, we omit it here, but note its solution for X_{n22} and X_{n33} as:

$$X_{n22} = \frac{\alpha \tau_P^2}{2k_P}, \quad X_{n33} = \frac{\alpha \tau_Q}{2} \cdot \frac{1}{\frac{c_Q}{\lambda_n^B} + k_Q}.$$

Finally, summing up the $N-1$ non-zero subsystem norms leads to our main result:

Theorem 5.5 *The squared $\mathcal{H}_2$ norm of the input-output mapping* (5.38) *is given by:*

$$\boxed{||H||_2^2 = \frac{\alpha}{2k_P}(N-1) + \frac{\alpha}{2\tau_Q}\sum_{n=2}^{N}\frac{1}{\frac{c_Q}{\lambda_n^B}+k_Q}.}$$
(5.41)

According to the discussion in Section 4.3.1, this expression represents the expected power losses due to the disturbance input w.

Currently, we are evaluating the system under the assumption that the inverter's frequency and voltage control dynamics are decoupled. Due to the decoupled output measurement, the $\mathcal{H}_2$ norm in (5.41) can be shown to be the sum of the respective norms of two decoupled subsystems: $||H||_2^2 = ||H^\theta||_2^2 + ||H^V||_2^2$.

The power losses associated with phase angle synchronization are

$$||H^\theta||_2^2 = \frac{\alpha}{2k_P}(N-1).$$
(5.42)

This is the same result as obtained for systems of synchronous generators in Chapter 4, where the droop coefficient k_P is analogous to the generator damping d. Earlier in this chapter, we also showed that this result holds for mixed-oscillator systems, provided that the dampings k and d were matched. Again, we point out that this expression scales linearly in network size N, but that it is independent of network topology. That is, under Assumption 5.4, a loosely connected network will incur the same transient losses during phase synchronization as a highly connected one.

The losses associated with voltage control are given by

$$||H^V||_2^2 = \frac{\alpha}{2\tau_Q}\sum_{n=2}^{N}\frac{1}{\frac{c_Q}{\lambda_n^B}+k_Q},$$
(5.43)

and depend on the topology of the network through the eigenvalues λ_n^B of L_B. The losses increase when the eigenvalues λ_n^B are larger, which implies that they increase with increasing line susceptances and network connectivity. The losses can be said to be inversely related to what we may call the network's *total effective reactance* as studied in [37], but we defer further discussion of this notion to future work. Instead, we will proceed to study the total power losses (5.41) for two extreme underlying network toplogies; the complete graph and the path graph, both shown in Figure 4.4.

Performance for specific network topologies

The result of Theorem 5.5 indicates that the transient losses increase with increasing network connectivity. While microgrid network structures may vary, in terms of

connectivity they all fall somewhere between the two extremes given by the complete graph and the path graph depicted in Figure 4.4. We next present results for these two special cases.

Theorem 5.6 *If the graph underlying the network $\mathcal{G}$ is* complete, *i.e., there is a line e_{ik} connecting each node pair $i, k \in \mathcal{N}$, then the expected power losses are bounded from above by:*

$$||H||_2^2 \leq \frac{\alpha}{2}(N-1)\left(\frac{1}{k_P} + \frac{1}{\tau_Q\left(\frac{c_Q}{N\underline{b}} + k_Q\right)}\right), \tag{5.44}$$

where $\underline{b}$ is the arithmetic mean of the susceptances b_{ik} for all network lines $e_{ik} \in \mathcal{E}$. The losses are bounded from below by:

$$||H||_2^2 \geq \frac{\alpha}{2}(N-1)\left(\frac{1}{k_P} + \frac{1}{\tau_Q\left(\frac{c_Q}{Nb_{\min}} + k_Q\right)}\right), \tag{5.45}$$

where $b_{\min} = \min_{\mathcal{E}} b_{ik}$. If $b_{ik} = \underline{b} = b_{\min}$ for all $e_{ik} \in \mathcal{E}$, then (5.44) – (5.45) turn into equalities.

Proof: See Appendix.

∎

Corollary 5.7 *If the graph underlying the network $\mathcal{G}$ is complete, then for large N*

$$||H||_2^2 \approx \frac{\alpha}{2}(N-1)\left(\frac{1}{k_P} + \frac{1}{\tau_Q k_Q}\right). \tag{5.46}$$

Proof: For large N, $\frac{c_Q}{N\underline{b}} \to 0$ and $\frac{c_Q}{Nb_{\min}} \to 0$ and the result follows.

∎

By Corollary 5.7, the losses in a large fully connected network will depend on the droop settings for active and reactive power respectively, where higher droop gains give smaller losses. We also notice that the losses associated with the voltage control decrease with increasing τ_Q. In the limit where $\tau_Q \to \infty$, the voltages are constant, and we retrieve the result in (4.22), in which a constant voltage profile was an underlying modeling assumption. In any case, the losses will grow unboundedly with the network size N (in the notation of Chapter 3, we can write (5.46) as $||H||_2^2 \sim \frac{1}{\beta}N$).
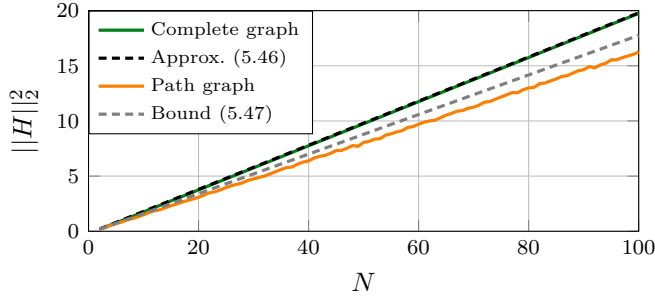
Figure 5.2: Values of the $\mathcal{H}_2$ norm in (5.41) for sample networks with path graph and complete graph topology, along with the approximation (5.46), for complete graphs and the bound (5.47) for path graphs. Here, $k_P = k_Q = c_Q = 1$, $\alpha = 0.2$ and the line susceptances are uniformly distributed on the interval $(0.5, 3.25)$.

When modeling the inverter-based microgrid, we consider a Kron reduced network model. Such reductions of power networks in general result in fully interconnected effective networks [53], and the expressions (5.44) – (5.46) hold. However, future microgrids may arise through the addition of generation units at some or all nodes in distribution grids. Distribution grids typically have a radial network structure, that is, they have a path graph as their underlying topology. They would also maintain path graph structure in the Kron-reduced case. The following theorem describes the performance in this case:

Theorem 5.8 *If the graph underlying the network $\mathcal{G}$ is a* path graph*, that is, $\mathcal{E} = \{e_{i,i-1}, e_{i,i+1}\}$ for $i = 2, \ldots, N-1$, and $\underline{b}$ is the arithmetic mean of the associated line susceptances, then the power losses are bounded by:*

$$||H||_2^2 \leq \frac{\alpha}{2}(N-1)\left(\frac{1}{k_P} + \frac{1}{\tau_Q(\frac{c_Q}{2\underline{b}} + k_Q)}\right). \tag{5.47}$$

Proof: See Appendix.

∎

This bound also has an underlying scaling that is linear in the network size N. However, the value of the losses will, for all N, have a dependence on the value of the average line susceptance $\underline{b}$, in contrast to the result for complete graphs in Corollary 5.7 where susceptances became irrelevant for large N. In Figure 5.2 the values of the $\mathcal{H}_2$ norm as a function of network size N are displayed for the two network topologies discussed in this section.

The fact that a highly interconnected network incurs *larger* power losses in recovering or maintaining synchrony than a sparsely interconnected network stands
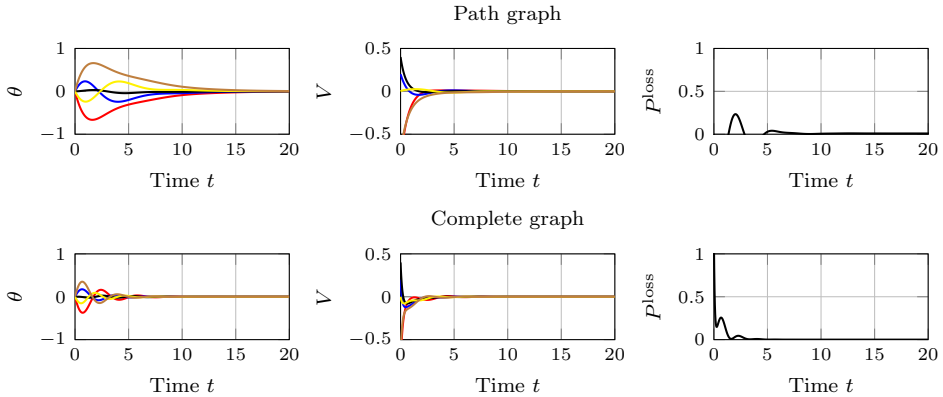
Figure 5.3: Simulations of the system (5.38) with $N = 5$ inverters. Here, the complete graph incurs, despite its higher rate of convergence, greater power losses.

in sharp contrast to our earlier result as well as to typical notions of power system stability, which we already discussed in Section 4.4.3. Figure 6.3 shows the transient behaviors obtained from simulations of a 5 node network with respective complete and path graph topologies. The plot clearly shows a faster convergence in the complete graph case. This faster convergence, however, comes at a greater cost in terms of power losses.

Some intuition behind this result may be obtained in terms of self-damping, or absolute feedback, which was a central topic in Chapter 3. Note that the voltage dynamics in (5.28), which are of first order, include an absolute feedback term (or self-damping) $-V_i$. This means that a disturbance could theoretically be attenuated even if node i were isolated, since the system $\dot{V}_i = -V_i$ is in itself asymptotically stable. However, we require the network to be connected, and the dynamics at node i must therefore also depend on neighboring nodes. The neighbors can support in the voltage control, but the control occurs through power flows, which also give rise to losses. Any additional line connected to node i increases the number of flows and losses (recall, node i could attenuate disturbances on its own without causing losses), and therefore, a more highly interconnected network leads to larger losses than a more loosely interconnected one.

5.3.4 Generalization to cross-coupled voltage and frequency dynamics

We will now relax the assumption of decoupled microgrid dynamics and again study the system (5.33). Under Assumptions 5.2 – 5.4 we can formulate the MIMO
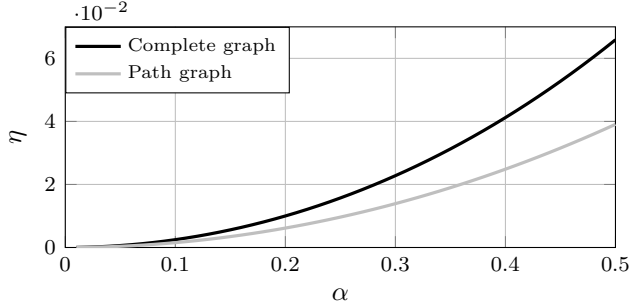
Figure 5.4: Norm error η in (5.49) as a function of α for networks of size $N = 50$ with complete graph and path graph structure, along with the approximation (5.59). Here, $x_{ij} = 0.2$, $k_P = 1$, $k_Q = 2$, $\tau_P = \tau_Q = 0.5$ and $c_Q = 1$. Note that the errors are small and decrease quadratically as $\alpha \to 0$, as predicted by Proposition 5.9.

system H^α as:

$$\begin{bmatrix} \dot{\theta} \\ \dot{\omega} \\ \dot{V} \end{bmatrix} = \begin{bmatrix} 0 & I & 0 \\ -\frac{k_P}{\tau_P}L_B & -\frac{1}{\tau_P}I & \frac{k_P}{\tau_P}\alpha L_B \\ -\frac{k_Q}{\tau_Q}\alpha L_B & 0 & -\frac{c_Q}{\tau_Q}I - \frac{k_Q}{\tau_Q}L_B \end{bmatrix} \begin{bmatrix} \theta \\ \omega \\ V \end{bmatrix} + \begin{bmatrix} 0 & 0 \\ \frac{1}{\tau_P}I & 0 \\ 0 & \frac{1}{\tau_Q}I \end{bmatrix} w \quad (5.48a)$$

$$y = \begin{bmatrix} \sqrt{\alpha}L_B^{1/2} & 0 & 0 \\ 0 & 0 & \sqrt{\alpha}L_B^{1/2} \end{bmatrix} \begin{bmatrix} \theta \\ \omega \\ V \end{bmatrix}. \quad (5.48b)$$

Compared to the lossless dynamics in (5.38a), the system matrix in (5.48a) has *cross-couplings* between the voltage and frequency dynamics which are proportional to the resistance-to-reactance ratio α. We will examine the effect of these cross-couplings on the system's performance in terms of the cross-coupling strength α. In particular, we are interested in characterizing the error obtained through the assumption of lossless microgrid dynamics from Section 5.3.3.

Consider for this purpose the relative error in the squared $\mathcal{H}_2$ norm between the system H^α in (5.48) and the decoupled system H in (5.38):

$$\eta = \frac{||H^\alpha||_2^2 - ||H||_2^2}{||H||_2^2}. \quad (5.49)$$

This quantity can be evaluated numerically and is shown in Figure 5.4 for $\alpha \in (0.01, 0.5)$ for two sample networks of size $N = 50$. We observe that the error is small and decreases faster than linearly as $\alpha \to 0$. These observations are accounted for by the following proposition:

Proposition 5.9 *The squared $\mathcal{H}_2$ norm of the system H^α in (5.48) is, for sufficiently small α, given by:*

$$||H^\alpha||_2^2 = c_1(\Lambda_B)\alpha + c_2(\Lambda_B)\alpha^3 + c_3(\Lambda_B)(\alpha^5) + \dots, \qquad (5.50)$$

where $c_k(\Lambda_B)$, $k = 1, 2, \dots$, are scalar functions of the eigenvalues of L_B. The first term corresponds to the $\mathcal{H}_2$ norm of (5.38):

$$c_1(\Lambda_B)\alpha = ||H||_2^2,$$

where $||H||_2^2$ was given in Theorem 5.5. It holds that

$$||H^\alpha||_2^2 \geq ||H||_2^2, \qquad (5.51)$$

and the relative error η is given by

$$\eta = \frac{c_2(\Lambda_B)}{c_1(\Lambda_B)}\alpha^2 + \frac{c_3(\Lambda_B)}{c_1(\Lambda_B)}\alpha^4 + \dots.$$

A proof outline is provided in this chapter's appendix, where we also provide analytic expressions for the coefficients $c_k(\Lambda_B)$ and the error η in the special case of a complete graph.

Proposition 5.9 shows that the results obtained by assuming a lossless microgrid with decoupled dynamics are robust in the sense that the error η is proportional to higher order powers of the coupling strength α, provided α is small enough to guarantee the finiteness of $||H^\alpha||_2^2$. Even in cases where the coupling strength α is such that the higher order terms are non-negligible, the inequality (5.51) shows that a lower bound on the losses is obtained under the decoupling assumption. Therefore, any limitations to system performance that are deduced from Theorem 5.5, such as the fact that losses grow linearly in network size, will hold also for the system (5.48) with the cross-coupled dynamics.

A weaker, yet insightful, result is given by the following corollary to Theorem 5.5 and Proposition 5.9:

Corollary 5.10 *The $\mathcal{H}_2$ norm of the system (5.48) satisfies*

$$||H^\alpha||_2^2 > ||H^\theta||_2^2,$$

where $||H^\theta||_2^2 = \frac{\alpha}{2k_P}(N-1)$ represents the transient resistive losses associated with frequency control in the microgrid (see (5.42)).

Proof: Follows immediately from (5.51) and (5.41).

∎

Now, recall that $||H^\theta||_2^2$ is (under Assumptions 5.2 – 5.4) precisely equivalent to our previous results from Sections 4.4 and 5.2.2, where we analyzed frequency synchronization in various settings. The bound in Corollary 5.10 therefore implies that our previous results give a lower bound on performance, and that transient resistive losses will be strictly larger if voltages are allowed to fluctuate.

5.4   Discussion

The results derived in this chapter have some interesting implications for future renewable energy integrated power grids. Firstly, the results in Section 5.2 showed that the order of the dynamics will not *per se* affect the performance measure we consider, as the two models result in equal losses if damping coefficients are equal. This means that asynchronous generation, to the extent that it can be respresented by the simple model (5.2), has the same performance as synchronous generation. Therefore, a replacement of a traditional generator through, for example, a wind farm, will not necessarily deteriorate the performance of the network.

However, large-scale integration of renewable energy will, as we already discussed, increase the number of network nodes, and thereby increase losses. This limitation to performance remains valid in mixed-oscillator systems, a result that is most easily seen through (5.24), as well as in microgrids, as seen from Theorem 5.5. Furthermore, when vaiable voltages are included in the model, this leads to strictly larger losses than when only considering frequency synchronization.

However, Theorem 5.2 implies that co-located asynchronous and synchronous generation at a common bus only "count once" with respect to the performance measure. This means that, given a fixed network size, adding new loads and asynchronous generators at existing nodes does not affect transient power losses, provided damping coefficients are uniform. Therefore, if asynchronous generator dampings (or droop control gains) can be adjusted to match the synchronous generators, they will not lead to increased losses in cases where they can be co-located with synchronous generators (or replace them at the same nodes). This result is striking, given that both generators would affect the system dynamics, and they are each subject to uncorrelated disturbance inputs that cause phase fluctuations. Overall, we can argue based on these results, that renewable energy integration need not necessarily deteriorate performance in power networks. But, since performance scales badly with network size, such integration should preferrably occur at as few nodes as possible.

5.5   Concluding summary of Chapter 5

In this chapter, we extended the model from Chapter 4 to account for certain aspects of renewable energy integrated power networks. We introduced models for phase, frequency and voltage dynamics for asynchronous generators, dynamic loads, and controllable power electronic inverters. We then studied the performance of

a mixed-oscillator system, capturing the frequency dynamics of a heterogeneously composed transmission network. We showed that if the dampings of synchronous and asynchronous machines in such a network can be matched, then they are equivalent in terms of the performance measure we consider. After that, we modeled an inverter-based microgrid, and accounted for variable voltage dynamics. Here, we showed that the previous results related to frequency synchronization provide a lower bound on performance and that losses are strictly larger if voltages are allowed to fluctuate. We also showed that the cross-couplings between the frequency and voltage dynamics, that are proportional to the resistance-to-reactance ratio in the power network, can be neglected without causing large errors with respect to the performance measure in question. Against that background, we will continue to focus on frequency control dynamics in Chapter 6, without further consideration of voltage control.

Appendix to Chapter 5

Proof of Theorem 5.2

By Lemma 4.3, $\operatorname{tr}(\tilde{L}_B^{-1}\tilde{L}_G) = \operatorname{tr}(L_B^\dagger L_G)$. We now apply Lemma 4.3 once again, but instead of grounding the Laplacians at node N, we now ground them at node N_0. We call these new grounded Laplacians $\tilde{L}_{B,N_0}$ and $\tilde{L}_{G,N_0}$. It holds:

$$\operatorname{tr}(L_B^\dagger L_G) = \operatorname{tr}(\tilde{L}_{B,N_0}^{-1}\tilde{L}_{G,N_0}).$$

Recall that we had, without loss of generality, assumed that the numbering of the nodes is such that the nodes $N_0 - N_\mathcal{S} + 1, ..., N_0$ are each connected in rising order to one of the nodes $N_0 + 1, ..., N_0 + N_\mathcal{S} = N$, like in the example in Figure 5.1. We can then consider the transformation matrix

$$V = \begin{bmatrix} I_{(N_0-N_\mathcal{S})} & 0 & 0 \\ 0 & I_{N_\mathcal{S}} & 0 \\ 0 & I_{N_\mathcal{S}} & I_{N_\mathcal{S}} \end{bmatrix},$$

for which it holds that

$$V^* L_B V = \begin{bmatrix} L_B^0 & 0 \\ 0 & B \end{bmatrix},$$

where L_B^0 is the susceptance matrix of the main (pre-augmented) network and $B = \operatorname{diag}\{b_{N_0-N_\mathcal{S}+1,N_0+1}, ..., b_{N_0,N}\}$. We also observe that

$$V^* L_G V = \begin{bmatrix} L_G^0 & 0 \\ 0 & 0 \end{bmatrix} = L_G.$$

Continue to define the deleted transformation matrix $\tilde{V}$ by the matrix that arises when deleting row and column N_0 from V. Then

$$\tilde{V}^* \tilde{L}_{B,n_0} \tilde{V} = \begin{bmatrix} \tilde{L}_B^0 & 0 \\ 0 & B \end{bmatrix}, \quad \tilde{V}^* \tilde{L}_{G,n_0} \tilde{V} = \begin{bmatrix} \tilde{L}_G^0 & 0 \\ 0 & 0 \end{bmatrix},$$

where $\tilde{L}_B^0$ and $\tilde{L}_G^0$ are the reduced versions of the Laplacians L_B^0 and L_G^0, with node N_0 grounded.

It is evident from its structure that V is non-singular and that its deleted version, $\tilde{V}$, has the same property. We can therefore write:

$$\operatorname{tr}(\tilde{L}_{B,N_0}^{-1}\tilde{L}_{G,N_0}) = \operatorname{tr}(\tilde{V}\tilde{V}^{-1}\tilde{L}_{B,N_0}^{-1}(\tilde{V}^*)^{-1}\tilde{V}^*\tilde{L}_{G,N_0}),$$

since $\tilde{V}\tilde{V}^{-1} = (\tilde{V}^*)^{-1}\tilde{V}^* = I_{(N_0+N_\mathcal{S}-1)}$. By the cyclic properties of the trace,

$$\begin{aligned} \operatorname{tr}(\tilde{V}\tilde{V}^{-1}\tilde{L}_{B,N_0}^{-1}(\tilde{V}^*)^{-1}\tilde{V}^*\tilde{L}_{G,N_0}) &= \operatorname{tr}(\tilde{V}^{-1}\tilde{L}_{B,N_0}^{-1}(\tilde{V}^*)^{-1}\tilde{V}^*\tilde{L}_{G,N_0}\tilde{V}) \\ &= \operatorname{tr}((\tilde{V}^*\tilde{L}_{B,N_0}\tilde{V})^{-1}\tilde{V}^*\tilde{L}_{G,N_0}\tilde{V}). \end{aligned}$$

It holds that[2]

$$(\tilde{V}^* \tilde{L}_{B,N_0} \tilde{V})^{-1} = \begin{bmatrix} \tilde{L}_B^0 {}^{-1} & 0 \\ 0 & B^{-1} \end{bmatrix}.$$

Then

$$\operatorname{tr}\left(\tilde{L}_{B,N_0}^{-1} \tilde{L}_{G,N_0}\right) = \operatorname{tr}\left(\begin{bmatrix} (\tilde{L}_B^0)^{-1} & 0 \\ 0 & B^{-1} \end{bmatrix}\begin{bmatrix} \tilde{L}_G^0 & 0 \\ 0 & 0 \end{bmatrix}\right) = \operatorname{tr}\left((\tilde{L}_B^0)^{-1}\tilde{L}_G^0\right) + \operatorname{tr}\left(B^{-1}0\right)$$

$$= \operatorname{tr}\left((\tilde{L}_B^0)^{-1}\tilde{L}_G^0\right).$$

Now, again by Lemma 4.3:

$$\operatorname{tr}\left((\tilde{L}_B^0)^{-1}\tilde{L}_G^0\right) = \operatorname{tr}\left(L_B^{0\dagger} L_G^0\right),$$

which concludes the proof.

∎

Proof of Theorem 5.6

Consider the function

$$\phi(x) = \frac{1}{\frac{1}{x} + k},$$

which is concave in $x > 0$ if $k \geq 0$ (note, $\phi''(x) = \frac{-2k}{(1+kx)^3} < 0$). We have that $\lambda_n^B/c_Q > 0$ for $n = 2, \ldots, N$ and can therefore apply Jensen's inequality of the form

$$\sum_{i=1}^n \phi(x_i) \leq n\phi\left(\frac{1}{n}\sum_{i=1}^n x_i\right) \tag{5.52}$$

to (5.41), where the function $\phi(\lambda_n^B/c_Q)$ appears in the denominator, to obtain:

$$||H||_2^2 \leq \frac{\alpha}{2k_P}(N-1) + \frac{\alpha}{2\tau_Q}(N-1)\frac{1}{\frac{c_Q}{\frac{1}{N-1}\sum_{n=2}^N \lambda_n^B} + k_Q}. \tag{5.53}$$

Using the definition of L_B in (2.19), we derive the average of the $N-1$ non-zero eigenvalues of L_B as

$$\frac{1}{N-1}\sum_{n=2}^N \lambda_n^B = \frac{\operatorname{tr}\{L_B\}}{N-1} = \frac{2\sum_{\mathcal{E}} b_{ik}}{N-1} = N\underline{b},$$

---

[2] This can be shown as follows: $\begin{bmatrix} \tilde{L}_B^0 {}^{-1} & 0 \\ 0 & B^{-1} \end{bmatrix}\begin{bmatrix} \tilde{L}_B^0 & 0 \\ 0 & B \end{bmatrix} = \begin{bmatrix} I_{N_0-1} & 0 \\ 0 & I_{N_S} \end{bmatrix} = I_{(N_0+N_S-1)}.$

where $\underline{b}$ is the arithmetic mean of the susceptances of the $N(N-1)/2$ edges in the complete graph. Substituting the above into (5.53) yields the result (5.44).

Given that $\phi(x)$ is monotonically increasing in x, the inequality (5.45) is derived by setting $L_B = b_{\min}L + \Delta L_B$. Here, L is an unweighted complete graph Laplacian, and ΔL_B is a complete graph Laplacian with edge weights $b_{ik} - b_{\min} \geq 0$. Since L and ΔL_B are simultaneously diagonalizable [74, Lemma A.1], $\lambda_n^B = b_{\min}N + \lambda_n^{\Delta B} \geq b_{\min}N$. If $L_B = b_{\min}L$, $\Delta L_B = 0$ and (5.45) holds with equality.

∎

Proof of Theorem 5.8

The argument follows the proof of Theorem 5.6. Here, the average of the $N - 1$ non-zero eigenvalues in (5.53) is

$$\frac{1}{N-1}\sum_{n=2}^{N}\lambda_n^B = \frac{\text{tr}\{L_B\}}{N-1} = \frac{2\sum_{\mathcal{E}} b_{ij}}{N-1} = 2\underline{b},$$

where $\underline{b}$ is the mean of the $(N-1)$ edge susceptances in the line graph.

∎

Proof outline of Proposition 5.9

To derive the $\mathcal{H}_2$ norm of the full system (5.48), we begin by performing the same unitary state transformation as in (5.39). As before, this gives us N decoupled subsystems H_n^α (of which we can disregard H_1^α, since it is unobservable):

$$\begin{bmatrix} \dot{\delta}_n \\ \dot{\omega}_n \\ \dot{V}_n \end{bmatrix} = \begin{bmatrix} 0 & 1 & 0 \\ -\frac{k_P}{\tau_P}\lambda_n^B & -\frac{1}{\tau_P} & \frac{k_P}{\tau_P}\alpha\lambda_n^B \\ -\frac{k_Q}{\tau_Q}\alpha\lambda_n^B & 0 & -\frac{c_Q}{\tau_Q} - \frac{k_Q}{\tau_Q}\lambda_n^B \end{bmatrix} \begin{bmatrix} \delta_n \\ \omega_n \\ V_n \end{bmatrix} + \begin{bmatrix} 0 & 0 \\ \frac{1}{\tau_P} & 0 \\ 0 & \frac{1}{\tau_Q} \end{bmatrix} \text{w} := \mathcal{A}_n^\alpha \psi_n + \mathcal{B}_n \text{w}_n$$

$$y_n = \begin{bmatrix} \sqrt{\alpha}(\lambda_n^B)^{1/2} & 0 & 0 \\ 0 & 0 & \sqrt{\alpha}(\lambda_n^B)^{1/2} \end{bmatrix} \begin{bmatrix} \delta_n \\ \omega_n \\ V_n \end{bmatrix} := \mathcal{C}_n \psi_n.$$

$$(5.54)$$

Each of these subsystems is exponentially stable for all α such that

$$\alpha^2 < \frac{k_Q^2 \tau_P (\lambda_n^B)^2 + (k_P \tau_Q^2 + k_Q \tau_Q + 2c_Q k_Q \tau_P)\lambda_n^B + \tau_P c_Q^2 + \tau_Q c_Q}{k_P k_Q \tau_P \tau_Q (\lambda_n^B)^2}, \qquad (5.55)$$

for all $n \in \{2, \ldots, N\}$, a result that can be derived using standard Routh-Hurwitz stability criteria. Henceforth, we will assume that this criterion is fulfilled.

The $\mathcal{H}_2$ norm of (5.54) is then given by $||H_n^\alpha||_2^2 = \text{tr}\{\mathcal{B}^* X_n^\alpha \mathcal{B}\}$, where X_n^α is the observability Gramian of the nth subsystem (5.54). Now, let

$$X_n^\alpha = X_n + X_n^1,$$

where X_n was the observability Gramian of the system without cross-couplings, given by (5.40). Then

$$||H_n^\alpha||_2^2 = \text{tr}\{\mathcal{B}_n^* X_n \mathcal{B}_n\} + \text{tr}\{\mathcal{B}_n^* X_n^1 \mathcal{B}_n\} = ||H_n||_2^2 + \text{tr}\{\mathcal{B}_n^* X_n^1 \mathcal{B}_n\}.$$

We can therefore regard $\text{tr}\{\mathcal{B}_n^* X_n^1 \mathcal{B}_n\}$ as a correction term to the previously derived $\mathcal{H}_2$ norm. We will show that this correction term can be written as $\text{tr}\{\mathcal{B}_n^* X_n^1 \mathcal{B}_n\} = c_2(\Lambda_B)\alpha^3 + c_3(\Lambda_B)(\alpha^5) + \ldots$.

Naturally, the new observability Gramian X_n^α satisfies the Lyapunov equation $\mathcal{A}_n^{\alpha*} X_n^\alpha + X_n^\alpha \mathcal{A}_n^\alpha + \mathcal{C}_n^* \mathcal{C}_n = 0$, which we can also write as

$$\mathcal{A}_n^{\alpha*} X_n^1 + X_n^1 \mathcal{A}_n^\alpha + \mathcal{A}_n^{\alpha*} X_n + X_n \mathcal{A}_n^\alpha + \mathcal{C}_n^* \mathcal{C}_n = 0 \tag{5.56}$$

We now substitute our previous Gramian X_n into this Lyapunov equation and get that $\mathcal{A}_n^{\alpha*} X_n + X_n \mathcal{A}_n^\alpha + \mathcal{C}_n^* \mathcal{C}_n = \alpha^2 Z_n$, where

$$Z_n = \frac{\lambda_n^B}{2} \begin{bmatrix} 0 & 0 & 1 - \frac{k_Q}{\frac{c_Q}{\lambda_n^B} + k_Q} \\ 0 & 0 & \tau_P \\ 1 - \frac{k_Q}{\frac{c_Q}{\lambda_n^B} + k_Q} & \tau_P & 0 \end{bmatrix}.$$

By substituting this into (5.56), we obtain the following equation for X_n^1:

$$\mathcal{A}_n^{\alpha*} X_n^1 + X_n^1 \mathcal{A}_n^\alpha + \alpha^2 Z_n = 0, \tag{5.57}$$

which has the form of a Lyapunov equation. Solving (5.57) for X_n^1 provides us with the correction term that gives us $||H_n^\alpha||_2^2$.

In order to make the subsequent derivations somewhat more tractable, we write the matrices $\mathcal{A}_n$, X^1 and Z as:

$$\mathcal{A}_n = \begin{bmatrix} 0 & 1 & 0 \\ -A_{12} & -A_{22} & \alpha a_2 \\ -\alpha a_1 & 0 & -A_{33} \end{bmatrix}, \quad X^1 = \begin{bmatrix} X_1 & X_{12} & X_{13} \\ X_{12} & X_2 & X_{23} \\ X_{13} & X_{23} & X_3 \end{bmatrix}, \quad Z = \begin{bmatrix} 0 & 0 & z_1 \\ 0 & 0 & z_2 \\ z_1 & z_2 & 0 \end{bmatrix}$$

Substituting this into (5.57), straightforward calculations give that:

$$\text{tr}\{\mathcal{B}_n^* X_n^1 \mathcal{B}_n\} = \frac{1}{\tau_P^2} X_2 + \frac{1}{\tau_Q^2} X_3 = \alpha^3 \frac{\tilde{c}_1 \alpha^2 + \tilde{c}_2}{\tilde{c}_3 \alpha^4 + \tilde{c}_4 \alpha^2 + \tilde{c}_5} \tag{5.58}$$

where the coefficients $\tilde{c}$ are somewhat involved functions of the eigenvalues λ_n^B and the inverter coefficients, but not of α:

$\tilde{c}_1 = a_1^2 a_2 \tau_Q^2 z_2 - a_1 a_2^2 \tau_P^2 z_1 + A_{22} a_1 a_2^2 \tau_P^2 z_2$

$\tilde{c}_2 = A_{12} A_{22} a_2 \tau_P^2 z_1 - A_{33}^2 a_1 \tau_Q^2 z_1 + A_{12} A_{33} a_1 \tau_Q^2 z_2 - A_{22} A_{33} a_1 \tau_Q^2 z_1 + A_{12} A_{22} A_{33} a_2 \tau_P^2 z_2$

$\tilde{c}_3 = -a_1^2 a_2^2 \tau_P^2 \tau_Q^2$

$\tilde{c}_4 = a_1 a_2 A_{22}^2 A_{33} \tau_P^2 \tau_Q^2 + a_1 a_2 A_{22} A_{33}^2 \tau_P^2 \tau_Q^2 + A_{12} a_1 a_2 A_{22} \tau_P^2 \tau_Q^2 - A_{12} a_1 a_2 A_{33} \tau_P^2 \tau_Q^2$

$\tilde{c}_5 = A_{12} a_1 a_2 A_{33} \tau_P^2 \tau_Q^2)\alpha^2 + A_{12}^2 A_{22} A_{33} \tau_P^2 \tau_Q^2 + A_{12} A_{22}^2 A_{33}^2 \tau_P^2 \tau_Q^2 + A_{12} A_{22} A_{33}$

The expression (5.58) can be shown to be positive, provided the stability criterion (5.55) is fulfilled, which leads to the statement (5.51) in the proposition. For such sufficently small α (we state a tractable condition in the case of a complete graph below), we can perform a Maclaurin series expansion of (5.58) which gives us that:

$$\text{tr}\{\mathcal{B}_n^* X_n^1 \mathcal{B}_n\} = \alpha^3 \frac{\tilde{c}_3}{\tilde{c}_5} + \frac{\tilde{c}_1 \tilde{c}_5 - \tilde{c}_2 \tilde{c}_4}{c_5^2} \alpha^5 + \cdots =: \alpha^3 \tilde{c}_n'(\lambda_n^B) + \alpha^5 \tilde{c}_n''(\lambda_n^B) + \cdots$$

Now, the full norm $||H^\alpha||_2^2$ is the sum of the $N-1$ subsystem norms, each associated with one eigenvalue λ_n^B. This can be written as $||H^\alpha||_2^2 = \sum_{n=2}^{N} ||H_n||_2^2 + \alpha^3 \sum_{n=2}^{N} \tilde{c}_n'(\lambda_n^B) + \alpha^5 \sum_{n=2}^{N} \tilde{c}_n''(\lambda_n^B)$ which is equivalent to the main statement of the proposition.

∎

Expression for full $\mathcal{H}_2$ norm in Proposition 5.9 for complete graphs

Consider the special case where the network graph $\mathcal{G}$ is complete. In this case, we can provide a tractable analytic expression for (5.50). If the number of nodes N is large, the coefficients in (5.50) are given as

$$c_k(\Lambda_B) = (N-1) \frac{k_P + k_Q \tau_Q}{2 k_Q^2} \left(\frac{k_P \tau_Q}{k_Q} \right)^{k-2},$$

for $k = 2, 3, \ldots$, and for all α such that $\frac{k_P \tau_Q}{k_Q} \alpha^2 < 1$. The coefficient $c_1(\Lambda_B)$ is in this case given by Corollary 5.7.

The relative error η for the complete graph then satisfies

$$\eta = \frac{k_P \tau_Q}{k_Q} \alpha^2 + \left(\frac{k_P \tau_Q}{k_Q} \right)^2 \alpha^4 + \ldots. \tag{5.59}$$

Numerical results indicate that (5.59) also provides an upper bound for the relative error (5.49) for general network topologies.

The result (5.59) shows that faster voltage control (large k_Q, small τ_Q) will decrease the effect of the cross-couplings on the transient power losses.

Chapter 6

Improving microgrid performance through distributed dynamic feedback

So far, we have studied performance in synchronizing power networks by considering static feedback control laws. In Chapter 4, we modeled frequency control using the swing equation for synchronous generators in the classical machine model. Similar physical relationships between phase angles and power outputs where exploited when modeling the static feedback control exerted by asynchronous machines in Chapter 5. Power electronic inverters in microgrids, however, are modeled as controllable voltage sources, and we therefore have a greater degree of freedom when designing control laws. In Section 5.1.2, we introduced the static droop control law for these inverters, which is designed to emulate synchronous machines. In this chapter, we will append a secondary controller layer to the droop controller, and consider dynamic feedback laws for frequency control of inverter-based microgrids.

Our results for the static feedback laws showed that there is a fundamental limitation to performance in power networks, in that losses associated with frequency synchronization scale unboundedly with network size. Furthermore, performance could not be improved by increasing network connectivity. We now return to the main question of Chapter 3 and address the question of whether dynamic feedback has the potential improve performance. For this purpose, we compare the static droop controller to two dynamic controllers with different architectures; the *distributed* averaging proportional-integral (DAPI) controller from Example 1.4, and a *centralized* averaging proportional-integral (CAPI) controller.

This chapter's main result shows that although the unfavorable scaling of losses with network size remains a limitation, they can be reduced by a constant factor by applying distributed dynamic feedback through the DAPI controller. Interestingly, the same conclusion does not hold for the centralized strategy, which achieves the same performance as static droop control. Moreover, we find that the performance improvement achieved through distributed dynamic feedback is larger in a sparsely interconnected network than in a highly interconnected one. We discuss implica-

tions of these results as well as optimal tuning of the controller for loss reduction.

The remainder of this Chapter is organized as follows. We introduce the control laws in Section 6.1 and derive analytic expressions for their performance in Section 6.2, where we also discuss the performance differences between the different control laws and for different network topologies. In Section 6.3, we discuss optimal tuning of the DAPI controller for loss reduction and in Section 6.4, we discuss the findings and relate to previous results. We summarize and conclude this chapter in Section 6.5.

6.1   Static and dynamic control laws for frequency control

We now introduce the control laws used to regulate frequency in the inverter-based microgrid. As usual, we consider a network $\mathcal{G} = \{\mathcal{V}, \mathcal{E}\}$, where $\mathcal{V} = \{1, \ldots, N\}$ is the set of nodes and $\mathcal{E} = \{e_{ij}\}$ represents the set of edges, or network lines. To make the analysis more tractable, we again assume a Kron-reduced network model, so that every node $i \in \mathcal{V}$ represents a generation unit with a power inverter as its grid interface. Each node has an associated phase angle θ_i and voltage magnitude V_i.

In this chapter, we focus on the performance of frequency control laws in the microgrid setting, and refer to Chapter 5 for an analysis of voltage control. There, we also provided a justification for analyzing these problems decoupled from each other. The first control law that we consider is therefore the standard frequency droop controller, which we derived in Section 5.1.2 as:

$$\dot{\theta}_i = \omega_i \tag{6.1a}$$

$$\tau_i \dot{\omega}_i = -\omega_i + \omega^{\text{ref}} - k_i(P_{e,i} - P_i^{\text{ref}}), \tag{6.1b}$$

where $k_i > 0$ is the droop coefficient, $\tau_i > 0$ is a filter time constant (see Section 5.1.2) and ω^{ref} and P_i^{ref} are the respective setpoints for frequency and active power.

The droop controller (6.1) is completely decentralized, requiring only local measurements of active power for implementation. Under reasonable conditions, (6.1) guarantees the desired power sharing, and synchronizes the inverter network to a common steady-state frequency ω^{ss}; see [72] for an analysis. However, as droop control is effectively proportional control, it typically leads to static deviations of the steady-state frequency ω^{ss} from the nominal frequency ω^{ref}. This deficiency motivates so-called secondary integral control (dynamic feedback), the goal of which is to eliminate the static error.

6.1.1   Distributed averaging proportional-integral (DAPI) control

Following [72, 5], we first consider a distributed dynamic control strategy which we refer to as *distributed averaging proportional-integral (DAPI)* control. For this purpose, assume that the inverters in the physical network, as described by $\mathcal{G}$, have access to a communication network represented by the weighted graph $\mathcal{G}^C =$

$\{\mathcal{V}, \mathcal{E}^C\}$, with weights $c_{ij} = c_{ji} > 0$ for all edges $e_{ij} \in \mathcal{E}^C$. Let $\mathcal{N}_i^C$ denote the neighbor set of node i in $\mathcal{G}^C$ and let L_C denote the graph Laplacian (defined as in (2.16)) of $\mathcal{G}^C$. The controller takes the form

$$\dot{\theta}_i = \omega_i \tag{6.2a}$$

$$\tau_i \dot{\omega}_i = -\omega_i + \omega^{\mathrm{ref}} - k_i(P_{e,i} - P_i^{\mathrm{ref}}) + \Omega_i \tag{6.2b}$$

$$q_i \dot{\Omega}_i = -\omega_i + \omega^{\mathrm{ref}} - \sum_{j \in \mathcal{N}_i^C} c_{ij}(\Omega_i - \Omega_j), \tag{6.2c}$$

where Ω_i is the secondary control variable that is internal to the controller and $q_i > 0$ is a controller parameter reflecting the integral gain. Notice that equations (6.2a) – (6.2b) are the droop controller dynamics (6.1), but with the additional secondary control input Ω_i. Hence, (6.2c) can be thought of as a distributed integral controller appended to (6.2a) – (6.2b).

As shown in [72], if the communication network $\mathcal{G}^C$ among the inverters is connected, the distributed controller (6.2) restores the network frequency to ω^{ref} while maintaining an optimal steady-state distribution of power injections among the inverters established by droop control. When all gains c_{ij} are zero, (6.2c) degenerates into a decentralized integral controller. In this case (6.2) possesses a large subspace of undesirable equilibria [23, Lemma 4.1] and the slightest measurement error causes phase angles to drift, in the way we discussed in Section 3.4.4 for vehicular formations. In practice, such a control design destabilizes the network unless the controllers have access to accurate phasor measurements units (PMUs). We refer to [4] for an elaboration.

6.1.2 Centralized averaging proportional-integral (CAPI) control

The steady state frequency deviation that arises through static droop control can also be eliminated through dynamic feedback with a centralized controller architecture. We consider one such dynamic feedback law, based on [4], which we refer to as *centralized averaging proportional-integral (CAPI)* control. In this case, the secondary control layer uses proportional control with respect to the average frequency over the entire network, in order to adjust the setpoint for the droop control at each inverter. The controller takes the form:

$$\dot{\theta}_i = \omega_i \tag{6.3a}$$

$$\tau_i \dot{\omega}_i = -\omega_i + \omega^{\mathrm{ref}} - k_i(P_{e,i} - P_i^{\mathrm{ref}}) + \Omega \tag{6.3b}$$

$$q\dot{\Omega} = \omega^{\mathrm{ref}} - \frac{1}{N} \sum_{i \in \mathcal{V}} \omega_i, \tag{6.3c}$$

where $q > 0$ is a positive constant. Note here that the centralized averaging in (6.3c) is assumed to be instantaneous and that the same secondary control variable Ω is shared among all interters as in (6.3b). This centralized control architecture thus

requires that each inverter in the network has a communication link to the node where the average is computed. This type of communication infrastructure is often less scalable and more vulnerable than the communication structure required for the DAPI algorithm, where it is only required that the network $\mathcal{G}^C$ is connected.

Remark 6.1 The models (6.1) – (6.2) reduce to the first-order inverter models considered in [73] if $\tau_i = 0$ for all $i \in \mathcal{V}$.

Remark 6.2 The second-order frequency droop control model (6.1) for inverter-based networks is analogous to the classical machine model for synchronous generators from Chapter 4. Even though we limit the analysis here to inverter-based networks, secondary control for frequency regulation makes sense also in synchronous generator networks. We refer to [5] for the corresponding problem formulation.

Remark 6.3 Any distributed control law can also be implemented using a centralized controller architecture, see, for example [2]. Therefore, if the communication structure for the CAPI controller is in place, it can also be used to implement the DAPI control law in (6.2). In this chapter, we will, however, limit the analysis of centralized control laws to the CAPI controller (6.3).

6.1.3   Power flows and closed loop dynamics

As before, we will consider the control dynamics for the inverter-based microgrids under the assumption of small deviations from a stable operating point. We therefore approximate the power injections $P_{e,i}$ at all nodes $i \in \mathcal{V}$ using the standard linear power flow assumption from Section 4.2.2:

$$P_{e,i} \approx \sum_{j \in \mathcal{N}_i} b_{ij}(\theta_i - \theta_j). \tag{6.4}$$

Substituting the linear power flow equation (6.4) into, respectively, the dynamics (6.1), (6.2), and (6.3), we notice that an equilibrium is given by $\omega = \omega^{\text{ref}}$, $\theta = L_B^{\dagger} P^{\text{ref}}$ and $\Omega = 0$ (L_B is the susceptance matrix associated with the network $\mathcal{G}$ and $\dagger$ denotes the Moore-Penrose pseudo inverse). Without loss of generality, we translate this operating point to the origin through a change of variables.

Using our standard model, where the system is subject to small disturbances or persistent small almplitude noise w acting on the inverters, we can summarize the the system dynamics as follows:

Standard droop control:

$$\begin{bmatrix} \dot{\theta} \\ \dot{\omega} \end{bmatrix} = \begin{bmatrix} 0 & I \\ -KT^{-1}L_B & -T^{-1} \end{bmatrix} \begin{bmatrix} \theta \\ \omega \end{bmatrix} + \begin{bmatrix} 0 \\ T^{-1} \end{bmatrix} w \tag{6.5}$$
$$=: \mathcal{A}_{\text{std}} \psi_{\text{std}} + \mathcal{B}_{\text{std}} w,$$

DAPI control:

$$\begin{bmatrix} \dot{\theta} \\ \dot{\omega} \\ \dot{\Omega} \end{bmatrix} = \begin{bmatrix} 0 & I & 0 \\ -KT^{-1}L_B & -T^{-1} & T^{-1} \\ 0 & Q^{-1} & -Q^{-1}L_C \end{bmatrix} \begin{bmatrix} \theta \\ \omega \\ \Omega \end{bmatrix} + \begin{bmatrix} 0 \\ T^{-1} \\ 0 \end{bmatrix} w \qquad (6.6)$$

$$=: \mathcal{A}_{\mathrm{DAPI}}\psi_{\mathrm{DAPI}} + \mathcal{B}_{\mathrm{DAPI}}w.$$

CAPI control:

$$\begin{bmatrix} \dot{\theta} \\ \dot{\omega} \\ \dot{\Omega} \end{bmatrix} = \begin{bmatrix} 0 & I & 0 \\ -MT^{-1}L_B & -T^{-1} & T^{-1}\mathbf{1} \\ 0 & -\frac{1}{qN}\mathbf{1}^T & 0 \end{bmatrix} \begin{bmatrix} \theta \\ \omega \\ \Omega \end{bmatrix} + \begin{bmatrix} 0 \\ T^{-1} \\ 0 \end{bmatrix} w \qquad (6.7)$$

$$=: \mathcal{A}_{\mathrm{CAPI}}\psi_{\mathrm{CAPI}} + \mathcal{B}_{\mathrm{CAPI}}w.$$

Here, we have introduced the column vectors θ, ω, Ω containing the translated system states, with total state vectors $\psi_{\mathrm{std}} = (\theta, \omega)^T \in \mathbb{R}^{2N}$, $\psi_{\mathrm{DAPI}} = (\theta, \omega, \Omega)^T \in \mathbb{R}^{3N}$, and $\psi_{\mathrm{CAPI}} = (\theta, \omega, \Omega)^T \in \mathbb{R}^{2N+1}$. The system parameters are given by $K = \mathrm{diag}\{k_i\}$, $T = \mathrm{diag}\{\tau_i\}$, and $Q = \mathrm{diag}\{q_i\}$, and we have used $\mathbf{1} = (1, 1, \ldots, 1)^T$.

6.2   Performance analysis

We are interested in evaluating performance of the distributed DAPI control law (6.6) and the centralized CAPI control law (6.7), with respect to the transient resistive power losses incurred in regulating frequency in the presence of the disturbance w. We will compare the performance of these control laws to the standard droop control law.

We use the performance measure from Definition 4.1 to define outputs of the systems (6.5) – (6.7) respectively as

$$y = \begin{bmatrix} L_G^{1/2} & 0 \end{bmatrix} \psi_{\mathrm{std}} =: \mathcal{C}_{\mathrm{std}}\psi_{std} \qquad (6.8)$$

$$y = \begin{bmatrix} L_G^{1/2} & 0 & 0 \end{bmatrix} \psi_{\mathrm{DAPI}} =: \mathcal{C}_{\mathrm{DAPI}}\psi_{DAPI} \qquad (6.9)$$

$$y = \begin{bmatrix} L_G^{1/2} & 0 & 0 \end{bmatrix} \psi_{\mathrm{DAPI}} =: \mathcal{C}_{\mathrm{CAPI}}\psi_{CAPI}, \qquad (6.10)$$

where L_G is the conductance matrix associated with the network $\mathcal{G}$. We now have three input-output mappings from w to y:

- H_{std} given by (6.5) and (6.8) ,

- H_{DAPI} given by (6.6) and (6.9) ,

- H_{CAPI} given by (6.7) and (6.10),

which are all linear-quadratic approximations of the full nonlinear problems. According to the discussion in Section 4.3.1, the output definitions (6.8) – (6.10) allow us to evalute transient power losses over the entire network using the systems' input-output $\mathcal{H}_2$ norms. In this section, we will derive closed-form expressions for those norms under the following assumptions:

Assumption 6.1 (Identical inverters) All inverters have identical parameter settings and low-pass filters, i.e., $K = \mathrm{diag}\{k\}$, $T = \mathrm{diag}\{\tau\}$, and $Q = \mathrm{diag}\{q\}$.

Assumption 6.2 (Uniform resistance-to-reactance ratios) The ratio of resistance to reactance, equivalently conductance to susceptance, of all lines are uniform and constant, i.e.,

$$\alpha := \frac{g_{ij}}{b_{ij}}, \tag{6.11}$$

for all $e_{ij} \in \mathcal{E}$. This implies $L_G = \alpha L_B$.

Assumption 6.3 (Topology for $\mathcal{G}^C$) The topology of the communication network $\mathcal{G}^C$ used in the DAPI control law (6.2) is identical to that of the physical network $\mathcal{G}$. We also assume

$$L_C = \gamma L_B, \tag{6.12}$$

i.e., $\gamma = \frac{c_{ij}}{b_{ij}}$, with $\gamma \geq 0$, for all $e_{ij} \in \mathcal{E} = \mathcal{E}^C$.

Assumption 6.3 implies that the secondary control layer for the DAPI control law is set up along the physical network lines, and is shown in [5] to constitute a sufficient criterion for load sharing with minimized generation costs. The assumption (6.12) says that the gain on the averaging term $\Omega_i - \Omega_j$ is set in proportion to the line susceptance b_{ij}, and will help us to obtain explicit analytic expressions for the $\mathcal{H}_2$ norm of (6.6). In Section 3.5, we discuss possible implications of a relaxation of that assumption.

6.2.1 $\mathcal{H}_2$ norm expressions

We lay out the details of the derivations of the $\mathcal{H}_2$ norms in the appendix and present the main result of this chapter here:

Theorem 6.1 *Under Assumptions 6.1 – 6.3, the squared $\mathcal{H}_2$ norm of the input-output mapping H_{std} as well as that of the input-output mapping H_{CAPI} is*

$$\boxed{||H_{\mathrm{std}}||_2^2 = ||H_{\mathrm{CAPI}}||_2^2 = \frac{\alpha}{2k}(N-1).} \tag{6.13}$$

The corresponding norm of the mapping H_{DAPI} is

$$\boxed{||H_{\mathrm{DAPI}}||_2^2 = \frac{\alpha}{2k} \sum_{n=2}^{N} \frac{1}{1 + \frac{\gamma\tau\lambda_n + q}{\gamma\lambda_n(\gamma\tau\lambda_n + q) + q^2 m \lambda_n}}.} \tag{6.14}$$

According to the discussion in Section 4.3.1, these expressions represent the expected power losses due to the disturbance input w.

Proof: See appendix.

■

By this theorem, the $\mathcal{H}_2$ norm of the CAPI control law is the same as that of the standard droop control law (and, in turn, the same as those derived for static frequency control in Chapters 4 and 5). This means that centralized dynamic feedback of the type (6.3) will not change performance compared to the static droop control law, independently of the the integral gain. Instead, losses still scale linearly with the total number of nodes N, and remain independent of network topology.

When the secondary control layer is instead distributed, as in the DAPI control law, the losses given by (6.14) still grow with the number of nodes, but they are smaller in absolute terms. Consider the following Corollary to Theorem 6.1:

Corollary 6.2 *For all $k, q, \tau, \gamma > 0$,*

$$||H_{\mathrm{DAPI}}||_2^2 < ||H_{\mathrm{std}}||_2^2,$$

that is, the expected power losses due to the disturbance w are smaller with the DAPI control strategy than with standard droop control or the CAPI control strategy.

Proof: Notice that $1 + \frac{\gamma \tau \lambda_n + q}{\gamma \lambda_n (\gamma \tau \lambda_n + q) + q^2 m \lambda_n} > 1$, since all terms are positive. Hence, $||H_{\mathrm{DAPI}}||_2^2 < \frac{\alpha}{2k} \sum_{n=2}^{N} 1 = \frac{\alpha}{2m}(N-1) = ||H_{\mathrm{std}}||_2^2 = ||H_{\mathrm{CAPI}}||_2^2.$

■

These results imply that dynamic feedback has the potential to improve system performance compared to static droop control, if it is implemented as in the DAPI control law. Perhaps surprisingly, the centralized approach in the CAPI control law does not achieve the same performance improvement in terms of power losses, even though centralized strategies are typically expected to be superior from a performance perspective (their downside being difficulty to implement and that they may have a single point of failure). For example, a centralized averaging PI controller for frequency control in power systems was shown in [3] to have a higher rate of convergence than a comparable distributed controller. A similar result was derived in [12] for wireless sensor networks in HVAC systems. We will demonstrate later in this chapter that the performance improvement achieved by the DAPI strategy can be attributed to a type of self damping, or absolute feedback, which does not arise with the centralized CAPI strategy.
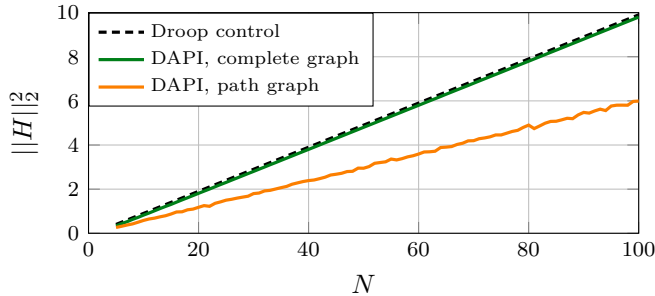
Figure 6.1: $\mathcal{H}_2$ norms in (6.13) - (6.14) for sample networks of size N with path graph and complete graph topologies. Note that $||H_{\text{std}}||_2^2$ in (6.13) is topology-independent. Here, $k = \gamma = m = 1$, line susceptances b_{ij} are uniformly distributed on $[0.5, 1.5]$.

We also note that the norms (6.13) and (6.14) both scale linearly with network's resistance-to-reactance ratio α, and hence that the ratio of the two norms is independent of α. This suggests that, to first-order, the relative performance improvement of distributed PI-control over the other control laws does not deteriorate as grid resistances increase. It can therefore not be attributed to the fact that we consider the frequency control problem decoupled from the voltage control problem (recall from Section 5.3.4 that the coupling strength is proportional to α).

In the next sections, we evaluate the room for performance improvement with the DAPI strategy over the static droop control law (we do not analyze the CAPI strategy further as it was shown to have the same performance as droop control). First, we evaluate how performance with the DAPI control law depends on the topology of the network.

6.2.2   Losses' dependence on network connectivity

It is interesting to note that while the losses under standard droop control (6.13) are entirely independent of network topology, the losses that are incurred under DAPI control (6.14) depend on network topology through the eigenvalues λ_n of L_B. In fact, the expression is monotonically increasing in λ_n, implying that losses grow with increasing network connectivity. This in particular implies that the relative performance improvement of DAPI control over droop control will be largest for sparse network topologies, such as those found in standard distribution networks and microgrids. The best performance can be expected to be achieved for a path graph topology, as this is the connected graph with the fewest number of edges. In Figure 6.1 we compare such a topology to a complete graph with respect to the results in Theorem 6.1. Although losses for both topologies grow with the network size, as discussed in the previous section, the comparison confirms the lower losses obtained in the path graph case.

The fact that a loosely interconnected network may outperform a highly interconnected network by incurring smaller power losses in maintaining synchrony is
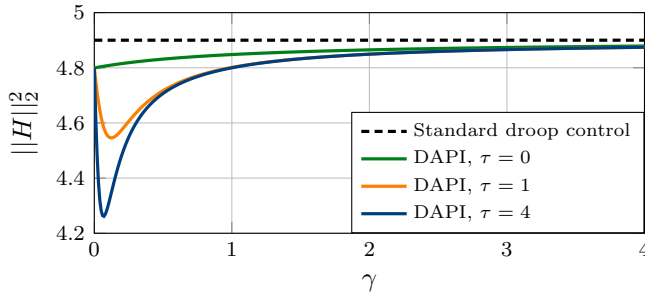
Figure 6.2: $\mathcal{H}_2$ norms in (6.14) as a function of γ for a complete graph with $N = 50$ nodes. Here, $k = m = 1$, and the filter time constant $\tau \in \{0, 1, 4\}$. For $\tau = 0$, the system (6.6) reduces to a first-order model, and the optimal $\gamma^\star = 0$.

surprising in light of typical notions of power system stability, although we also found it to hold for losses associated with voltage control in Section 5.3. As we have discussed before, the connectivity of a network is directly related to its ability to synchronize [18, 62, 67] as well as its damping and rate of convergence [49]. Our results show that, although additional network lines may improve phase coherence and stability, they also lead to additional power flows that incur losses. Hence, there is a trade-off between performance objectives.

6.3 Control design for loss reduction

In the previous section, we established that the DAPI control strategy improves performance in terms of transient power losses for droop-controlled microgrids. We now turn to the question of optimal tuning of this controller. That is, how should the integral action q in (6.2) and the communication gain parameter γ in (6.12) be chosen to minimize transient losses, with respect to a given droop-controlled network.

6.3.1 Communication gain

As discussed in Section 6.1, distributed PI control requires a communication network through which inverters can communicate their secondary control variables Ω_i. While any non-zero gains c_{ij} for the distributed averaging in (6.2c) will guarantee that the control objectives are reached [73], an important design question is how to choose these gains to optimize the transient performance considered herein. In our case, this choice is reflected through the parameter γ in (6.12).

Figure 6.2 displays the transient power losses associated with the DAPI control, as given by (6.14), as a function of γ for a sample network with a complete graph structure. As the figure indicates, it turns out that there exists a distinct optimal value for $\gamma \geq 0$:

Lemma 6.3 *For a given network with DAPI control* (6.6) *and under Assumptions 6.1 – 6.3, there is a unique communication gain ratio $\gamma^\star$ which minimizes the $\mathcal{H}_2$ norm* (6.14).

Proof: The optimum is given by the positive root of $\frac{d}{d\gamma}||H_{\text{DAPI}}||_2^2\big|_{\gamma=\gamma^\star} = 0$. By inspecting (6.14), we note that this corresponds to finding the root of a quadratic function in γ with positive coefficients, and therefore, the root characterizes a global minimum. If there is no positive root, then $||H_{\text{DAPI}}||_2^2$ is minimized by $\gamma^\star = 0$.

∎

For complete graphs, the potential for performance improvement is smaller than for more sparsely connected networks. An optimized controller tuning is therefore particularly relevant. For this case, we provide a closed-form expression for $\gamma^\star$:

Corollary 6.4 *If the graph underlying the network $\mathcal{G}$ is complete and the line susceptances $b_{ij} = b$ for all $e_{ij} \in \mathcal{E}$, then $\gamma^\star$ is given by*

$$\gamma^\star = \frac{q}{Nb\tau}\left(\sqrt{Nbk\tau} - 1\right) \tag{6.15}$$

if $Nbk\tau > 1$. Otherwise, $\gamma^\star = 0$.

Proof: When the edge weights b_{ij} are uniform, the $N-1$ non-zero eigenvalues of the complete graph Laplacian $L_B \in \mathbb{R}^{N \times N}$ are all given by Nb. It then suffices to evaluate $\frac{d}{d\gamma} \frac{1}{1 + \frac{\gamma\tau Nb + q}{\gamma Nb(\gamma\tau Nb + q) + q^2 kNb}} = 0$ and the result follows.

∎

The value of $\gamma^\star$ is strongly dependent on the network parameters, but once these are given, it is easy to find the optimal tuning. We note that the optimal $\gamma^\star$ is often very small, in particular if the time constant τ is small. In the limit where $\tau = 0$, we have $\gamma^\star = 0$. However, we cannot choose a design where $\gamma = 0$ without causing an undesirable drift in the system, which in practice causes instabilities (see Section 6.1.1). If γ, on the other hand, is set too large, the distributed averaging term of (6.2) converges too fast compared to the phase angles, and deteriorates the damping effect of the secondary control. A simulation of this case is shown in Figure 6.3. In the theoretical limit where $\gamma \to \infty$, the distributed averaging of the integral state Ω in the DAPI strategy in (6.2c) is instantaneous, and becomes equivalent to the centralized strategy in (6.3c). In this limit, there is therefore no performance improvement over static droop control.
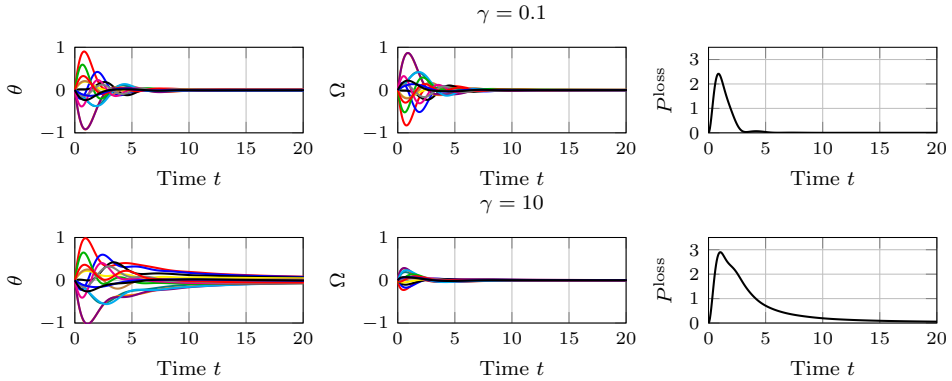
Figure 6.3: Simulation of the system (6.6) on a 20-node network with path topology, with associated power losses (4.6). Here, $k = q = \tau = 1$ and $\gamma = 0.1$ (upper panel) and $\gamma = 10$ (lower panel).

6.3.2   Integral action

Now, consider the parameter q in (6.2), which reflects the amount of integral action in the DAPI controller. First, notice that in the limit where $q \to \infty$ the integral action vanishes and the standard droop control dynamics (5.7) are retrieved, with the associated $\mathcal{H}_2$ norm (6.13). It is easy to show based on (6.14) that as q then decreases, losses are reduced monotonically and at an increasing rate. On the other hand, in the theoretical limit of an infinitely large integral gain ($q = 0$), the DAPI strategy allows the system to become arbitrarily well damped and losses minimized. Figure 6.4 displays the relative performance improvement achieved through the DAPI strategy as a function of q, for a hypothetical network based on the IEEE 57-bus benchmark system topology [55].

Our results also indicate that the importance of the distributed averaging term in (6.2) increases as the integral action decreases. That is, the optimal communication gain given by $\gamma^\star$ grows as q grows. For a complete graph with uniform edge weights, this relationship is linear, by Corollary 6.4. For the IEEE 57-bus benchmark system topology we display this relationship between q and $\gamma^\star$ in Figure 6.4. This relationship implies that the smaller the integral gain, the more important is the distrbuted averaging term in (6.2c).

6.4   Discussion

This chapter's main result shows that distributed dynamic feedback can improve performance of inverter-based micgrogrids, in that transient losses associated with frequency regulation are reduced, compared to static feedback and centralized dynamic feedback. However, the losses' unbounded scaling with the network size N
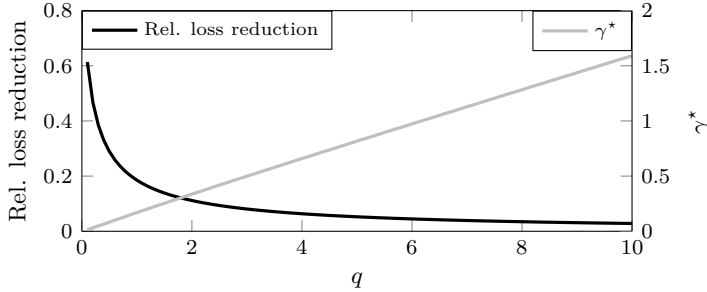
Figure 6.4: Relative loss reduction with DAPI control for a test network based on the IEEE 57 bus benchmark system topology, at $\gamma = \gamma^{\star}$, as function of q. Here, $k = \tau = 1$.

remains. We now discuss some interpretations and implications of our results.

6.4.1   Relation to distributed dynamic feedback for vehicular formations

One of the main results of Chapter 3 was that dynamic feedback of DAPI type improves performance in vehicular formations that have access to absolute velocity feedback, but where position measurements are relative. The apparent reason for this performance improvement was that the DAPI strategy serves as a distributed integral controller appended to the static controller, which integrates the absolute velocity measurements and thus yields a substitute for absolute position measurements. The relative position and absolute velocity feedback in vehicular formations is analogous to the type of feedback that is typically available in power systems, where one has access to absolute measurements of frequencies, but where phase feedback is relative. We would therefore expect the DAPI control law to improve performance also for a power system, which is indeed what this chapter's main result shows.

   In the vehicular formation case, the performance with DAPI feedback came close to that of static feedback where absolute measurements from positions were also available. In a power system, absolute feedback from phase angles can only be obtained with accurate phasor measurement units (PMUs). With such PMUs, the corresponding feedback law is a special case of the DAPI controller (6.2). Consider (6.2), and set all coefficients $c_{ij} = 0$ in (6.2c). This is equivalent to substituting the absolute feedback term $-\frac{1}{q}\theta_i$ for Ω_i in (6.2b), which is only feasible if PMUs are available (see Section 6.1.1). In this case, we thus have absolute feedback from phase angles. Note now, that this strategy also corresponds to setting the parameter $\gamma = 0$, which we found in Section 6.3 to be an optimal (though, infeasible) choice for γ, for example if the filter time constant τ is small.

   Based on these observations, we conclude that the reason for the improved performance with the DAPI controller is that the secondary control variable Ω_i

in (6.2) serves as a substitute for absolute feedback, or self-damping. With the centralized CAPI strategy on the other hand, all inverters share the same secondary control variable Ω regardless of their individual states θ_i and ω_i, and Ω in (6.3) can therefore not act as a substitute for self-damping. By assigning more weight to the distributed averaging term in the DAPI strategy, that is, by increasing the parameter γ, the DAPI strategy becomes more similar to the CAPI strategy and the beneficial self-damping effect vanishes.

6.4.2 Topology dependence and self-damping

The main result of this chapter showed that the relative performance improvement of the dynamic DAPI control law over the static droop control law is largest for sparse network topologies. Therefore, adding power lines to increase network connectivity will also increase the transient power losses. This is in sharp contrast to standard notions of power system stability, as we already discussed. The apparent reason for this result is also linked to the notion of DAPI control as a substitute for self-damping. With self-damping, disturbances can be attenuated independently of power flows. Increasing connectivity by introducing more lines generates more power flows, which do not affect the self damping, but increase losses.

Recall that a similar conclusion was found to hold for the performance of voltage control dynamics in Section 5.3.3, where the control dynamics included self-damping explicitly. Our results indicate that in the presence of explicit or emulated absolute self-damping, the price of synchrony performance measure will be smaller for a sparsely interconnected network than for a highly interconnected one.

6.4.3 Optimal distributed averaging

We also derived results on optimal tuning of the DAPI controller for loss reduction. In particular, the distributed averaging term in (6.2c) should be tuned so that $c_{ij} = \gamma^\star b_{ij}$, where b_{ij} is the line susceptance and $\gamma^\star$ is a unique positive optimizer. As we discussed, too large communication gains c_{ij} causes a too strong reliance on the distributed averaging in relation to the the self-damping. In the present work, we made the restrictive assumption that the graph topology for the distributed averaging follows that of the physical network, and found controller tunings that minimize losses. With more degrees of freedom, we conjecture that losses can be even further reduced by judicious control design. An important direction for future work is therefore to find an optimal topology configuration of the communication network.

6.5 Concluding summary of Chapter 6

In this chapter, we evaluated the performance of an inverter-based microgrid in terms of the power losses incurred in regulating the frequency to a synchronous

state after a disturbance. We compared the standard static frequency droop controller to two dynamic controllers; a distributed averaging PI (DAPI) controller, and a centralized averaging PI (CAPI) controller. We found that while the CAPI controller does not change performance compared to droop control, the DAPI controller has the potential to significantly reduce the transient power losses. This relative performance improvement compared to droop control is largest for sparse network topologies, such as those found in standard distribution networks and microgrids. We find that the reason for this performance improvement lies in the fact that the DAPI controller emulates self-damping, or absolute feedback from phase angles, which has a positive effect on performance.

It is important to note, however, that the losses' scaling with the size of the network remains unchanged with the DAPI strategy, and seems to remain a fundamental performance limitation in systems where active power flows are the mechanism by which the system regulates frequency. Therefore, they may become increasingly significant when power networks become increasingly distributed and the number of generators grows. Since DAPI control both eliminates stationary control errors *and* reduces transient losses and (unlike centralized CAPI control), our results provide additional arguments in favor of distributed algorithms for secondary frequency control in microgrids.

Appendix to Chapter 6

Proof of Theorem 6.1

The $\mathcal{H}_2$ norm for the system with frequency droop control (6.5) was derived in Section 5.3.3 under the same assumptions as 6.1 – 6.2. We do not repeat the derivations here, but note the result (6.13).

When deriving the norms of the DAPI system (6.6) and the CAPI system (6.7), we follow the approach in [6] (also used in Section 5.3.3) and transform the state vectors using a unitary transformation matrix U so that $\theta = U\hat{\theta}$, $\omega = U\hat{\omega}$. For the controller state Ω, we have $\Omega = U\hat{\Omega}$ in the DAPI case, where $\Omega \in \mathbb{R}^N$, but take $\Omega = \hat{\Omega}$ in the CAPI case, where $\Omega \in \mathbb{R}$.

We take U as the unitary matrix which diagonalizes L_B. That is, $L_B = U^*\Lambda_B U$ with $\Lambda_B = \text{diag}\{\lambda_1, \lambda_2, \ldots, \lambda_N\}$. Without loss of generality, we number the eigenvalues so that $0 = \lambda_1 < \lambda_2 \le \cdots \lambda_N$, and therefore get that

$$U = \begin{bmatrix} \frac{1}{\sqrt{N}}\mathbf{1} & \mathbf{v}_2 & \cdots & \mathbf{v}_N \end{bmatrix},$$

where $\mathbf{v}_2, \cdots, \mathbf{v}_n$ are the eigenvectors corresponding to eigenvalues $\lambda_2, \cdots, \lambda_N$. Note that by Assumptions 6.1 – 6.3, L_B, L_C and $L_G^{1/2}$ are simultaneously diagonalizable, so $U^*L_C U = \gamma\Lambda_B$ and $U^*L_G^{1/2}U = \sqrt{\alpha}\Lambda_B^{1/2}$. Given that the $\mathcal{H}_2$ norm is unitarily invariant, we can also define the transformed output $\hat{y} = U^*y$ and input $\hat{w} = U^*w$.

We now consider the DAPI and the CAPI systems separately.

DAPI

The transformations outlined above imply that $\hat{\psi}_{\text{DAPI}}$ is given by

$$\psi_{\text{DAPI}} = \mathbf{U}\hat{\psi}_{\text{DAPI}}, \text{ where } \mathbf{U} = \begin{bmatrix} U & 0 & 0 \\ 0 & U & 0 \\ 0 & 0 & U \end{bmatrix}.$$

It then holds that $\hat{\psi}_{\text{DAPI}} = \mathbf{U}^*\mathcal{A}_{\text{DAPI}}\mathbf{U}\hat{\psi}_{\text{DAPI}} + \mathbf{U}^*\mathcal{B}_{\text{DAPI}}\mathbf{U}\hat{w}$ and $\hat{y} = \mathbf{U}^*\mathcal{B}_{\text{DAPI}}\mathbf{U}\hat{\psi}_{\text{DAPI}}$. This system corresponds to one in which all blocks have been diagonalized. It can therefore be written as N decoupled subsystems $\hat{H}_{\text{DAPI},n}$:

$$\begin{bmatrix} \dot{\hat{\theta}}_n \\ \dot{\hat{\omega}}_n \\ \dot{\hat{\Omega}}_n \end{bmatrix} = \begin{bmatrix} 0 & 1 & 0 \\ -\frac{k}{\tau}\lambda_n & -\frac{1}{\tau} & \frac{1}{\tau} \\ 0 & -\frac{1}{q} & -\frac{1}{q}\gamma\lambda_n \end{bmatrix} \begin{bmatrix} \hat{\theta}_n \\ \hat{\omega}_n \\ \hat{\Omega}_n \end{bmatrix} + \begin{bmatrix} 0 \\ \frac{1}{\tau} \\ 0 \end{bmatrix} \hat{w}_n$$

$$=: \hat{\mathcal{A}}_{\text{DAPI},n}\hat{\psi}_{\text{DAPI},n} + \hat{\mathcal{B}}_{\text{DAPI},n}\hat{w}_n \qquad (6.16)$$

$$\hat{y}_n = \sqrt{\alpha\lambda_n} \begin{bmatrix} 1 & 0 & 0 \end{bmatrix} \begin{bmatrix} \hat{\theta}_n \\ \hat{\omega}_n \\ \hat{\Omega}_n \end{bmatrix} =: \hat{\mathcal{C}}_{\text{std},n}\hat{\psi}_{\text{std},n}.$$

The squared $\mathcal{H}_2$ norm of H_{DAPI} is the sum of the squares of the decoupled subsystems' norms, that is, $||H_{\text{DAPI}}||_2^2 = ||\hat{H}_{\text{DAPI}}||_2^2 = \sum_{n=1}^{N} ||\hat{H}_{\text{DAPI},n}||_2^2$.

Notice that the subsystem $\hat{H}_{\text{DAPI},1}$ corresponding to $\lambda_1 = 0$ has the output $\hat{y}_1 = 0$. This verifies that the zero mode is unobservable and $||\hat{H}_{\text{DAPI},1}||_2^2 = 0$. For $n \neq 0$, the subsystem norms are calculated by solving the Lyapunov equation (2.8) for the observability Gramians X_n. We omit the expansion of that equation here, but refer to Section 5.3.3 for a similar derivation.

CAPI

In this case, we have that the transformed state vector $\hat{\psi}_{\text{CAPI}}$ is given by

$$\psi_{\text{CAPI}} = \mathbf{U}\hat{\psi}_{\text{CAPI}}, \text{ where } \mathbf{U} = \begin{bmatrix} U & 0_{N \times N} & 0_{N \times 1} \\ 0_{N \times N} & U & 0_{N \times 1} \\ 0_{1 \times N} & 0_{1 \times N} & 1 \end{bmatrix}$$

and it holds that $\dot{\hat{\psi}}_{\text{CAPI}} = \mathbf{U}^* \mathcal{A}_{\text{CAPI}} \mathbf{U}\hat{\psi}_{\text{CAPI}} + \mathbf{U}^* \mathcal{B}_{\text{CAPI}} \mathbf{U}\hat{w}$ and $\hat{y} = \mathbf{U}^* \mathcal{B}_{\text{CAPI}} \mathbf{U}\hat{\psi}_{\text{CAPI}}$. This system, denoted $\hat{H}_{\text{CAPI}}$, can be written as

$$\begin{bmatrix} \dot{\hat{\theta}} \\ \dot{\hat{\omega}} \\ \dot{\hat{\Omega}} \end{bmatrix} = \begin{bmatrix} 0 & I & 0 \\ -\frac{k}{\tau}\Lambda_B & -\frac{1}{\tau}I & \frac{\sqrt{N}}{\tau}e_1 \\ 0 & -\frac{1}{q\sqrt{N}}e_1^T & 0 \end{bmatrix} \begin{bmatrix} \hat{\theta} \\ \hat{\omega} \\ \hat{\Omega} \end{bmatrix} + \begin{bmatrix} 0 \\ \frac{1}{\tau}I \\ 0 \end{bmatrix} \hat{w}$$

$$=: \hat{\mathcal{A}}_{\text{CAPI}}\hat{\psi}_{\text{CAPI}} + \hat{\mathcal{B}}_{\text{CAPI}}\hat{w} \tag{6.17}$$

$$\hat{y} = \begin{bmatrix} \sqrt{\alpha}\Lambda_B^{1/2} & 0 & 0 \end{bmatrix} \begin{bmatrix} \hat{\theta}_n \\ \hat{\omega} \\ \hat{\Omega} \end{bmatrix} =: \hat{\mathcal{C}}_{\text{CAPI}}\hat{\psi}_{\text{CAPI}},$$

where e_1 is the column vector $(1, 0, \ldots, 0)^T$. Here, we have used the fact that since U is unitary, its column vectors satisfy $\mathbf{v}_j \perp \mathbf{1}$ for all $j = 2, \ldots, N$. Therefore, the block (2,3) above reads $\frac{1}{\tau}U^*\mathbf{1} = \frac{1}{\tau}\frac{1}{\sqrt{N}}Ne_1$ and the block (3,2) reads $\frac{1}{Nq}\mathbf{1}^T U = \frac{1}{Nq}\frac{1}{\sqrt{N}}Ne_1^T$.

Now, we solve the Lyapunov equation

$$\hat{A}_{\text{CAPI}}^* X + X\hat{A}_{\text{CAPI}} = -\hat{C}_{\text{CAPI}}^* \hat{C}_{\text{CAPI}}, \tag{6.18}$$

directly, after partitioning the Gramian X as:

$$X = \begin{bmatrix} X_1 & X_{12} & X_{13} \\ X_{12}^* & X_2 & X_{23} \\ X_{13}^* & X_{23}* & X_3 \end{bmatrix},$$

where $X_1, X_2, X_{12} \in \mathbb{R}^{N \times N}$, $X_{13}, X_{23} \in \mathbb{R}^{N \times 1}$ and $X_3 \in \mathbb{R}$. Since

$$||H_{\text{CAPI}}||_2^2 = ||\hat{H}_{\text{CAPI}}||_2^2 = \text{tr}\{\mathcal{B}_{\text{CAPI}}^* X \mathcal{B}_{\text{CAPI}}\} = \frac{1}{\tau^2}\text{tr}\{X_2\}, \tag{6.19}$$

we need only solve (6.18) for $\operatorname{tr}\{X_2\}$. Expanding (6.18), we obtain six linearly independent equations, of which we only need four:

$$-\frac{k}{\tau}\Lambda_B X_{12}^* - X_{12}\frac{k}{\tau}\Lambda_B = -\alpha\Lambda_B \qquad (6.20)$$

$$-\frac{k}{\tau}\Lambda_B X_{23} + \frac{\sqrt{N}}{\tau}X_{12}e_1 = 0 \qquad (6.21)$$

$$X_{12} - \frac{1}{\tau}X_2 + \frac{1}{q\sqrt{N}}e_1 X_{23}^* + X_{12}^* - \frac{1}{\tau}X_2 + \frac{1}{q\sqrt{N}}X_{23}e_1^T = 0 \qquad (6.22)$$

$$\frac{\sqrt{N}}{\tau}e_1^T X_{23} + \frac{\sqrt{N}}{\tau}X_{23}^* e_1 = 0, \qquad (6.23)$$

where (6.20) corresponds to element (1,1) of the Lyapunov equation, (6.21) to element (1,3), (6.22) to element (2,2) and (6.23) to element (3,3).

First, note that by (6.23) it holds $X_{23} \perp e_1$, or, in order words, the first element in X_{23} must be zero. Therefore, the terms $\frac{1}{q\sqrt{N}}e_1 X_{23}^*$, $\frac{1}{q\sqrt{N}}X_{23}e_1^T$ from (6.22) vanish, and we obtain:

$$-\frac{2}{\tau}X_2 + X_{12} + X_{12}^* = 0 \quad \Rightarrow \quad \operatorname{tr}\{X_2\} = \tau\operatorname{tr}\{X_{12}\}, \qquad (6.24)$$

where the left hand side is the expression we are after. Now, in order to solve remaining equations for $\operatorname{tr}\{X_{12}\}$, consider (6.20), which says:

$$\Lambda_B X_{12}^* + X_{12}\Lambda_B = \frac{\alpha\tau}{k}\Lambda_B \quad \Leftrightarrow \quad \Lambda_B X_{12}^* \Lambda_B^\dagger + X_{12}\tilde{I} = \frac{\alpha\tau}{k}\tilde{I}, \qquad (6.25)$$

where $\Lambda_B^\dagger$ is the pseudo-inverse of Λ_B, given as $\Lambda_B^\dagger = \operatorname{diag}\{0, 1/\lambda_2, \ldots, 1/\lambda_N\}$ and we denote by $\tilde{I} = \Lambda_B\Lambda_B^\dagger = \begin{bmatrix} 0 & 0_{1\times N} \\ 0_{N\times 1} & I_{N-1} \end{bmatrix}$. Now, we take the trace of both sides of (6.25):

$$\operatorname{tr}\{\Lambda_B X_{12}^* \Lambda_B^\dagger\} + \operatorname{tr}\{X_{12}\tilde{I}\} = \frac{\alpha\tau}{k}\operatorname{tr}\{\tilde{I}\} = \frac{\alpha\tau}{k}(N-1),$$

which, due to the circulant properties of the trace is equivalent to

$$2\operatorname{tr}\{X_{12}\tilde{I}\} = \frac{\alpha\tau}{k}(N-1). \qquad (6.26)$$

Now, if it holds that $\operatorname{tr}\{X_{12}\} = \operatorname{tr}\{X_{12}\tilde{I}\}$, then we can substitute (6.26) into (6.24) and be done. This holds if element (1,1) of X_{12} is zero. Indeed, note that (6.21) implies that

$$\frac{\sqrt{N}}{\tau}X_{12}e_1 = \frac{k}{\tau}\Lambda_B,$$

and the first element of this $N \times 1$-vector equation reads $(\frac{\sqrt{N}}{\tau}X_{12})_1 = 0$, since the first row of Λ_B is zero. Therefore, $\operatorname{tr}\{X_{12}\tilde{I}\} = \operatorname{tr}\{X_{12}\} = \frac{1}{\tau}\operatorname{tr}\{X_2\}$, and substituting this into (6.26), we obtain that $\operatorname{tr}\{X_2\} = \frac{\alpha\tau^2}{2k}(N-1)$, and thus, by (6.19)

$$\|H_{\text{CAPI}}\|_2^2 = \frac{\alpha}{2k}(N-1).$$

Chapter 7

Conclusions and directions for future work

Networked control systems that rely on distributed feedback control generally have limitations to their overall performance, in particular as the networks grow large. This thesis has focused on characterizing such performance limitations for two types of networked systems: consensus and vehicular formation problems modeled over regular lattice structures; and electric power networks modeled as dynamical systems over general graphs. We now conclude the thesis by summarizing some of our main findings concerning these systems, and by laying out some directions for future work.

7.1   Main conclusions

There are several ways to characterize the performance of a networked control system. For example, through the time or control effort required to reach a particular system state, through stability margins, or through robustness towards disturbances. In this thesis, we have chosen to study performance measures that quantify nodal state fluctuations for systems that are subject to distributed stochastic disturbances. Motivated by the applications mentioned in the introduction, we first focused on measures of coherence, which characterize how well an approximate state of consensus can be maintained, or how closely a vehicular formation resembles a rigid body. We then studied a second performance measure, which characterizes lack of synchrony, and used it to measure resistive power losses associated with synchronization in power networks (the "price of synchrony").

   The two performance measures have in common that they typically scale badly with network size, and that absolute state feedback, or self-damping, is key in improving performance, both with static and dynamic feedback laws. However, while increasing network connectivity improves network coherence, it often has no effect on the price of synchrony. Similarly, the order of the system dynamics plays slightly different roles in the two problem settings. We elaborate on these topics below.

Performance scaling and fundamental limitations

In the consensus and vehicular formation problems, we evaluated performance in terms of the individual (per node) variance of nodal phase fluctuations with respect to a global mean, as in (1.10). We showed in Chapter 3 that this individual variance generally increases as the network grows, preventing networks from being coherent on a large scale. In power networks, we were instead interested in quantifying the total network's resistive power losses, and showed that this could be evaluated as a sum of local errors, as in (1.11), over all network nodes. Therefore, even though the losses remain bounded when counted per generator node (to the extent this is meaningful, given that losses arise over the network lines), the total losses will grow linearly with the size of the network. In both cases, the unfavorable scaling of performance with network size can be seen as a *fundamental limitation* to performance in the respective system.

When it comes to network coherence, this limitation can be alleviated by adding links to increase network connectivity. Such a strategy does, however, typically not affect the price of synchrony. Under certain assumptions, this means that a sparsely interconnected power network incurs the same power losses in resynchronizing after a disturbance as a highly interconnected network, even though the latter is more coherent in terms of phase fluctuations. Still, we demonstrated that certain performance improvement in terms of reduced losses can be achieved through a judicious placement of well-damped generators in the network, or a co-location of generators at a common node. In general, however, the unbounded growth of losses with network size remains a limitation that may become important in future power grids, which are expected to have highly distributed generation sources leading to larger networks.

As one of the main objectives of this thesis, we also evaluated whether dynamic feedback control could alleviate some of the performance limitations that had been shown to hold with standard, static control laws. In the context of the consensus and vehicular formation problems, we considered general dynamic feedback laws with a single internal controller state. We found that no such feedback law can improve performance scaling compared to static feedback, as long as it must rely on relative measurements between neighboring nodes. The scaling of performance also remains unchanged when the controller has access to absolute state measurements, unless those measurements are noiseless. In this case, a performance improvement by a constant factor can, however, be achieved using dynamic feedback, which may of course be important in practice. We examined such a case in Chapter 6, where it was shown that a particular distributed dynamic feedback law reduces the power losses associated with frequency control in a microgrid setting.

Order of system dynamics

Throughout this thesis, we have considered both first- and second-order systems. In physical systems, second-order dynamics are prevalent, but a first-order model

can serve as an idealization or approximation. For example, in the droop control laws that we derived for power inverters, the second-order model reduced to the first-order model if there were no measurement delay dynamics or inertia. Against that background, it has been relevant to determine in which way the choice of model order affects performance.

Remarkably, we showed in Chapter 5 that first-order, second-order and mixed first- and second-order systems are equivalent in terms of the price of synchrony. This indicates, for example, that a replacement of traditional generators by renewable generators with faster dynamics will not affect performance in terms of transient power losses, if their dampings can be matched. In terms of coherence, however, higher order models typically have a more severe performance scaling. For example, the second-order vehicular formation with relative feedback requires 5 spatial dimensions to be fully coherent, while the first-order consensus system only requires 3 dimensions. If, however, the vehicular formation has absolute feedback from velocity, performance scales as in the consensus problem. With dynamic feedback, performance may even be better.

Importance of absolute feedback

The most severe limitations to performance in the networked systems we have considered are for systems whose feedback relies entirely on relative measurements between neighboring nodes. In a vehicle platoon, this could mean that radars are used to measure the relative position error with respect to the vehicle ahead, and, in a power system, that feedback relies on power flows, which are (approximately) proportional to phase angle differences. In order to alleviate the performance limitations, we have demonstrated that absolute state feedback, or self-damping, is necessary. In these examples, one would thus have to broadcast position measurements with respect to a global reference frame across the platoon, or install phasor measurement units (PMUs) in the power network.

With a dynamic feedback law, there is however a possibility to emulate such absolute feedback. The feedback laws which were shown in this thesis to improve performance compared to static feedback laws were distributed proportional-integral (PI) controllers, which integrate absolute velocity or frequency measurements to yield a substitute for absolute position or phase feedback (or self-damping). Since such a strategy is sensitive to measurement errors or bias, it is important that the controllers at the different nodes align their internal controller states through a distributed averaging (consensus) protocol. In the power system setting, we showed that a too strong alignment of that type causes the feedback to rely too much on the neighbors, which in turn reduces the self-damping effect. Consequently, a centralized integral controller that simply integrates the network average and shares this with all network nodes cannot improve performance compared to static feedback. This result serves as an additional argument in favor of distributed strategies for frequency control in power networks.

7.2   Directions for future work

Many of the results presented in this thesis also provide interesting openings for further research, some of which we have already mentioned throughout the thesis. For example, we limited the study of dynamic feedback laws in Chapter 3 to controllers with a single memory state. It is an open research question whether our result changes if the number of memory states is arbitrary. Other types of controllers, for example controllers that are not strictly proper, or controllers with alternative architectures, are also worth examining in terms of their performance limitations.

In Chapter 6, we showed that a distributed averaging PI controller can improve performance in terms of the power losses associated with frequency regulation, compared to both static droop control and a centralized averaging PI controller. We showed that while the distributed averaging of the internal controller states is necessary for the stability of the system, the gain should be kept small in order to maintain a desired self-damping effect. Since this distributed averaging requires an additional communication infrastructure, an interesting question for future work is the optimal configuration of this network for loss reduction. It is also worth investigating whether there are other control architectures, ranging from centralized to decentralized, that perform better than the distributed averaging PI controller while still fulfilling the control objectives related to frequency regulation in power grids.

Throughout this thesis, we have evaluated performance in terms of output variances, which has amounted to $\mathcal{H}_2$ norm based performance metrics. In Chapter 3, this meant that we evaluated sums over inverted eigenvalues (see Example 3.1). Such sums do not necessarily scale as individual inverted eigenvalues, such as the smallest non-zero eigenvalue, which is instead related to the $\mathcal{H}_\infty$ norm. An intriguing direction for future work is therefore to relate the present results to $\mathcal{H}_\infty$ norm based performance metrics and their interpretations in terms of, for example, robustness.

List of Figures

Bibliography

[1] A. Alam, B. Besselink, V. Turri, J. Martensson, and K. H. Johansson. Heavy-duty vehicle platooning for sustainable freight transportation: A cooperative method to enhance safety and efficiency. *IEEE Control Systems*, 35(6):34–56, Dec 2015.

[2] M. Andreasson. Control of multi-agent systems with applications to distributed frequency control of power systems. Licentiate thesis, KTH, Automatic Control Lab, Stockholm, Sweden, Mar 2013. URL `http://urn.kb.se/resolve?urn=urn:nbn:se:kth:diva-118638`.

[3] M. Andreasson, D. V. Dimarogonas, K. H. Johansson, and H. Sandberg. Distributed vs. centralized power systems frequency control. In *2013 European Control Conference (ECC)*, pages 3524–3529, Jul 2013.

[4] M. Andreasson, D.V. Dimarogonas, H. Sandberg, and K.H. Johansson. Distributed control of networked dynamical systems: Static feedback, integral action and consensus. *IEEE Trans. on Automatic Control*, 59(7):1750–1764, Jul 2014.

[5] M. Andreasson, D.V. Dimarogonas, H. Sandberg, and K.H. Johansson. Distributed PI-control with applications to power systems frequency control. In *Proc. of the American Control Conf.*, pages 3183–3188, Jun 2014.

[6] B. Bamieh and D.F. Gayme. The price of synchrony: Resistive losses due to phase synchronization in power networks. In *Proc. of the American Control Conf.*, pages 5815 – 5820, Jun 2013.

[7] B. Bamieh, M. R. Jovanović, P. Mitra, and S. Patterson. Coherence in large-scale networks: Dimension-dependent limitations of local feedback. *IEEE Trans. on Automatic Control*, 57(9):2235 –2249, Sep. 2012.

[8] B. Bamieh, F. Paganini, and M.A. Dahleh. Distributed control of spatially invariant systems. *IEEE Trans. on Automatic Control*, 47(7):1091–1107, Jul 2002.

[9] P. Barooah, P.G. Mehta, and J.P. Hespanha. Mistuning-based control design to improve closed-loop stability margin of vehicular platoons. *IEEE Trans. on Automatic Control*, 54(9):2100–2113, Sep 2009.

[10] A.R. Bergen and D.J. Hill. A structure preserving model for power system stability analysis. *IEEE Trans. on Power Apparatus and Systems*, PAS-100 (1):25–35, 1981.

[11] B. Besselink, V. Turri, S. H. van de Hoef, K. Liang, A. Alam, J. Martensson, and K. H. Johansson. Cyber-physical control of road freight transport. *Proceedings of the IEEE*, 2016. To appear.

[12] X. Cao, J. Chen, Y. Xiao, and Y. Sun. Building-environment control with wireless sensor and actuator networks: Centralized versus distributed. *IEEE Transactions on Industrial Electronics*, 57(11):3596–3605, Nov 2010.

[13] H.-D. Chiang. *Direct Methods for Stability Analysis of Electric Power Systems: Theoretical Foundation, BCU Methodologies, and Applications*. Wiley, 2011.

[14] H.-D. Chiang, F.F. Wu, and P.P. Varaiya. Foundations of the potential energy boundary surface method for power system transient stability analysis. *IEEE Trans. on Circuits and Systems*, 35(6):712 –728, Jun 1988.

[15] F. R. K. Chung. *Spectral Graph Theory*. American Mathematical Society, 1994.

[16] G. Cybenko. Dynamic load balancing for distributed memory multiprocessors. *Journal of parallel and distributed computing*, 7(2):279 – 301, 1989.

[17] F. Dörfler and F. Bullo. Spectral analysis of synchronization in a lossless structure-preserving power network model. In *Proc. of the 1st IEEE Int'l Conf. on Smart Grid Communications*, pages 179–184, Gaithersburg, MD, 2010.

[18] F. Dörfler and F. Bullo. Synchronization and transient stability in power networks and non-uniform Kuramoto oscillators. In *Proc. of the American Control Conf.*, pages 930 –937, Baltimore, MD, 2010.

[19] F. Dörfler and F. Bullo. Topological equivalence of a structure-preserving power network model and a non-uniform Kuramoto model of coupled oscillators. In *Proc. of the 50th IEEE Conf. on Decision and Control*, pages 7099 –7104, Orlando, FL, 2011.

[20] F. Dörfler and F. Bullo. Synchronization and transient stability in power networks and non-uniform Kuramoto oscillators. *SIAM Journal on Control and Optimization*, 50(3):1616–1642, 2012.

[21] F. Dörfler and F. Bullo. Kron reduction of graphs with applications to electrical networks. *IEEE Trans. on Circuits and Systems I*, 60(1):150–163, Jan 2013.

[22] F. Dörfler, M. Chertkov, and F. Bullo. Synchronization in complex oscillator networks and smart grids. *Proc. of the National Academy of Sciences*, 110(6): 2005–2010, 2013.

[23] F. Dörfler, M. R. Jovanovićand M. Chertkov, and F. Bullo. Sparsity-promoting optimal wide-area control of power networks. *IEEE Transactions on Power Systems*, 29(5):2281–2291, Sept 2014.

[24] P. G. Doyle and J. L. Snell. *Random Walks and Electric Networks.* The Mathematical Association of America, 1984.

[25] J.B. Ekanayake, Lee Holdsworth, Xue Guang Wu, and N. Jenkins. Dynamic modeling of doubly fed induction generator wind turbines. *IEEE Trans. on Power Sys.*, 18(2):803–809, 2003.

[26] K. Elkington. Analysis of the dynamic impact of large wind parks in power systems. Technical Report Rapport 12:06, 2004. URL `http://elforsk.se/Rapporter/?rid=12_06_`.

[27] K. Elkington, J. G. Slootweg, M. Ghandhari, and W. L. Kling. *Reduced-Order Modelling of Wind Turbines*, pages 821–847. John Wiley and Sons, Ltd, 2012.

[28] W. Ellens, F.M. Spieksma, P. Van Mieghem, A. Jamakovic, and R.E. Kooij. Effective graph resistance. *Linear Algebra Appl.*, 435(10):2491–2506, 2011.

[29] M. Fardad, F. Lin, and M. R. Jovanović. Design of optimal sparse interconnection graphs for synchronization of oscillator networks. *IEEE Trans. on Automatic Control*, 2014. doi:10.1109/TAC.2014.2301577; also arXiv:1302.0449.

[30] H. Farhangi. The path of the smart grid. *IEEE Power and Energy Magazine*, 8(1):18–28, Jan 2010.

[31] U.S.-Canada Power System Outage Task Force. Final report on the august 14, 2003 blackout in the United States and Canada: Causes and recommendations. Technical report, 2012. URL `https://reports.energy.gov/BlackoutFinal-Web.pdf`.

[32] L. Freris and D. Infield. *Renewable energy in power systems.* John Wiley & Sons, Chichester, U.K., 2008.

[33] B. Gentile, J.W. Simpson-Porco, F. Dörfler, S. Zampieri, and F. Bullo. On reactive power flow and voltage stability in microgrids. In *Proc. of the American Control Conf.*, pages 759–764, Jun 2014.

[34] A. Ghosh, S. Boyd, and A. Saberi. Minimizing effective resistance of a graph. *SIAM Rev.*, 50(1):37–66, Feb 1988.

[35] J. D. Glover, M. S. Sarma, and T. Overbye. *Power System Analysis and Design.* Cengage, Stamford, 5 edition, 2011.

[36] T. W. Grunberg and D. F. Gayme. Minimizing interactions in mixed oscillator networks. In *Proc. of the IEEE Conf. on Decision and Control*, pages 3209 – 3215, Los Angeles, CA, Dec. 2014.

[37] T. W. Grunberg and D. F. Gayme. Effective resistance based performance measures for networked oscillators. *Preprint*, 2015.

[38] I. Gutman and W. Xiao. Generalized inverse of the Laplacian matrix and some applications. *Bulletin. Classe des Sciences Mathématiques et Naturelles. Sciences Mathématiques*, 129(29):15–23, 2004. URL http://eudml.org/doc/125464.

[39] H. Hao and P. Barooah. On achieving size-independent stability margin of vehicular lattice formations with distributed control. *IEEE Transactions on Automatic Control*, 57(10):2688–2694, Oct 2012.

[40] H. Hao and P. Barooah. Stability and robustness of large platoons of vehicles with double-integrator models and nearest neighbor interaction. *International Journal of Robust and Nonlinear Control*, 23(18):2097–2122, 2013.

[41] R. Hororitz and P. Varaiya. Control design of an automated highway system. *Proc. of the IEEE*, 88(7):913–925, 2000.

[42] K. Purchala et al. Usefulness of DC power flow for active power flow analysis. In *Proc. of IEEE PES General Meeting*, pages 2457–2462. IEEE, 2005.

[43] R. Kearsley. Restoration in Sweden and experience gained from the blackout of 1983. *IEEE Trans. on Power Sys.*, 2(2):422–428, 1987.

[44] R.H. Lasseter. Microgrids. In *Power Eng. Society Winter Meeting, 2002. IEEE*, volume 1, pages 305–308 vol.1, 2002.

[45] B.C. Lesieutre, P.W. Sauer, and M. A. Pai. Development and comparative study of induction machine based dynamic P, Q load models. *IEEE Trans. on Power Sys.*, 10(1):182–191, 1995.

[46] W. S. Levine and Athans M. On the optimal error regulation of a string of moving vehicles. *IEEE Trans. on Automatic Control*, AC-11(3):355–361, Jul. 1966.

[47] F. Lin, M. Fardad, and M.R. Jovanovic. Optimal control of vehicular formations with nearest neighbor interactions. *IEEE Trans. on Automatic Control*, 57(9):2203–2218, Sep 2012.

[48] L.-Y. Lu and C.-C. Chu. Consensus-based droop control synthesis for multiple power converters in lossy micro-grids. In *2013 IEEE PES Asia-Pacific Power and Energy Eng. Conf.*, Dec 2013.

[49] E. Mallada and A. Tang. Improving damping of power networks: Power scheduling and impedance adaptation. In *Proc. of the 50th IEEE Conf. on Decision and Control*, pages 7729 – 7734, Orlando, FL, 2011.

[50] T. Markvart. Microgrids: Power systems for the 21st century? *Refocus*, 7(4): 44 – 48, 2006.

[51] S. M. Metzer and B. C. Kuo. Optimal regulation of systems described by a countably infinite number of objects. *Automatica*, 7(3):359–366, 1971.

[52] Ulla Miekkala. Graph properties for splitting with grounded Laplacian matrices. *BIT*, 33(3):485–495, 1993. ISSN 0006-3835.

[53] Adilson E. Motter, Seth A. Myers, Marian Anghel, and Takashi Nishikawa. Spontaneous synchrony in power-grid networks. *Nat Phys*, 9(3):191–197, Feb. 2013.

[54] T. Nishikawa and A. E. Motter. Comparative analysis of existing models for power-grid synchronization. *New Journal of Physics*, 17(1):015012, 2015.

[55] University of Washington. Power systems test case archive, 1993. URL `http://www.ee.washington.edu/research/pstca`.

[56] P. Kundur et al. Definition and classification of power system stability IEEE/CIGRE joint task force on stability terms and definitions. *IEEE Trans. on Power Sys.*, 19(3):1387 – 1401, Aug. 2004.

[57] M. A. Pai. *Power System Stability by Lyapunov's Method*. N.Holland Publishing Co., New York, NY, 1981.

[58] M. A. Pai. *Energy Function Analysis for Power System Stability*. Kluwer Academic Publishers, Norwell, MA, 1989.

[59] S. Patterson and B. Bamieh. Consensus and coherence in fractal networks. *IEEE Trans. on Control of Network Systems*, 1(4):338–348, Dec 2014.

[60] S. Patterson, B. Bamieh, and A. El Abbadi. Convergence rates of distributed average consensus with stochastic link failures. *IEEE Transactions on Automatic Control*, 55(4):880–892, Apr 2010.

[61] J.A. Peas Lopes, C.L. Moreira, and A.G. Madureira. Defining control strategies for microgrids islanded operation. *IEEE Trans. on Power Sys.*, 21(2):916–924, May 2006.

[62] L.M. Pecora and T. Carroll. Master stability functions for synchronized coupled systems. *Phys. Rev. Letters*, 80(10):2109–2112, 1998.

[63] B. K. Poolla, S. Bolognani, and F. Dörfler. Placing rotational inertia in power grids. *American Control Conference*, 2016. To appear.

[64] W. Ren, R. W. Beard, and E. M. Atkins. Information consensus in multivehicle cooperative control. *IEEE Control Systems Magazine*, 27(2):71–82, Apr 2007.

[65] B.P. Roberts and C. Sandberg. The role of energy storage in development of smart grids. *Proc. of the IEEE*, 99(6):1139–1144, 2011.

[66] R.D. Robinett and D.G. Wilson. Transient stability and control of renewable generators based on Hamiltonian surface shaping and power flow control: Part i-theory. In *Proc. of the IEEE Int'l Conf. on Control Applications*, pages 2196–2202, 2010.

[67] J. Schiffer, R. Ortega, A. Astolfi, J. Raisch, and T. Sezi. Conditions for stability of droop-controlled inverter-based microgrids. *Automatica*, 50(10):2457 – 2469, 2014. ISSN 0005-1098.

[68] J. Schiffer, T. Seel, J. Raisch, and T. Sezi. Voltage stability and reactive power sharing in inverter-based microgrids with consensus-based distributed voltage control. *IEEE Trans. on Control Systems Technology*, 24(1):96–109, Jan 2016.

[69] M. Siami and N. Motee. Fundamental limits on robustness measures in networks of interconnected systems. In *Proc. of the 52nd IEEE Conf. on Decision and Control*, Florence, Italy, 2013.

[70] M. Siami and N. Motee. Fundamental limits and tradeoffs on disturbance propagation in large-scale dynamical networks. *IEEE Trans. on Automatic Control*, 2016. To appear.

[71] J. W. Simpson-Porco, F. Dörfler, and F. Bullo. Droop-controlled inverters are Kuramoto oscillators. In *Proc. of the 3rd IFAC Workshop on Distributed Estimation and Control in Networked Sys.*, pages 264–269, Santa Barbara, CA, 2012.

[72] J. W. Simpson-Porco, F. Dörfler, and F. Bullo. Synchronization and power sharing for droop-controlled inverters in islanded microgrids. *Automatica*, 49 (9):2603 – 2611, 2013.

[73] J. W. Simpson-Porco, Q. Shafiee, F. Dörfler, J. C. Vasquez, J. M. Guerrero, and F. Bullo. Secondary frequency and voltage control of islanded microgrids via distributed averaging. *IEEE Trans. on Industrial Electronics*, 62(11):7025–7038, Nov 2015.

[74] E. Sjödin. The price of synchrony: Evaluating transient power losses in renewable energy integrated power networks. MSc. thesis, KTH, Automatic Control Lab, Stockholm, Sweden, Aug 2013. URL `http://urn.kb.se/resolve?urn=urn:nbn:se:kth:diva-133579`.

[75] J. G. Slootweg and W. L. Kling. *Impacts of Wind Power on Power System Dynamics*, pages 629–651. John Wiley and Sons, Ltd, 2005.

[76] K. J. Åström. *Stochastic control theory*. Academic Press, Inc., New York, 1970.

[77] D. Swaroop and J. K. Hedrick. String stability of interconnected systems. *IEEE Trans. on Automatic Control*, 41(3):349–357, Mar 1996.

[78] D. Swaroop and J. K. Hedrick. Constant spacing strategies for platooning in automated highway systems. *Trans. ASME J. Dyn. Sys., Meas., Control*, 121 (3):462–270, 1999.

[79] E. Tegling, M. Andreasson, J. W. Simpson-Porco, and H. Sandberg. Improving performance of droop-controlled microgrids through distributed pi-control. *American Control Conference*, 2016. To appear.

[80] R. Teodorescu, M. Liserre, and P. Rodriguez. *Grid Converters for Photovoltaic and Wind Power Systems*. John Wiley and Sons, Hoboken, NJ, 2010.

[81] U.S. Energy Information Administration. Annual energy outlooks 2010 with projections to 2035. Technical Report DOE/EIA-0383, U.S. Dept. of Energy, 2010. URL http://www.eia.doe.gov/oiaf/aeo.

[82] P. Varaiya. Smart cars on smart roads: problems of control. *IEEE Transactions on Automatic Control*, 38(2):195–207, Feb 1993.

[83] P. Varaiya, F.F. Wu, and R.-L. Chen. Direct methods for transient stability analysis of power systems: Recent results. *Proceedings of the IEEE*, 73(12): 1703 – 1715, Dec. 1985.

[84] A. von Meier. *Electric Power Systems: A Conceptual Introduction*. John Wiley and Sons Inc., Hoboken, NJ, 2006.

[85] L. Xiao, S. Boyd, and S.-J. Kim. Distributed average consensus with least-mean-square deviation. *Journal of Parallel and Distributed Computing*, 67(1): 33 – 46, 2007.

[86] C. Zhan, G. Chen, and L. F. Yeung. On the distributions of Laplacian eigenvalues versus node degrees in complex networks. *Physica A: Statistical Mechanics and its Applications*, 389(8):1779 – 1788, 2010.

[87] F. Zhang and Q. Zhang. Eigenvalue inequalities for matrix product. *IEEE Trans. on Automatic Control*, 51(9):1506–1509, 2006.

[88] C. Zhao, E. Mallada, and F. Dörfler. Distributed frequency control for stability and economic dispatch in power networks. In *Proc. of the 2015 American Control Conference*, pages 2359–2364, Jul 2015.

[89] Q. Zhong and T. Hornik. *Control of Power Inverters in Renewable Energy and Smart Grid Integration*. Wiley-IEEE Press, Chichester, UK, 2013.

[90] K. Zhou, J. C. Doyle, and K. Glover. *Robust and optimal control.* Prentice
     Hall, New Jersey, 1996.

[91] Zpryme Research & Consulting. Power systems of the future: The case for
     energy storage, distributed generation, and microgrids. Technical report, IEEE
     Smart Grid, Nov. 2012.